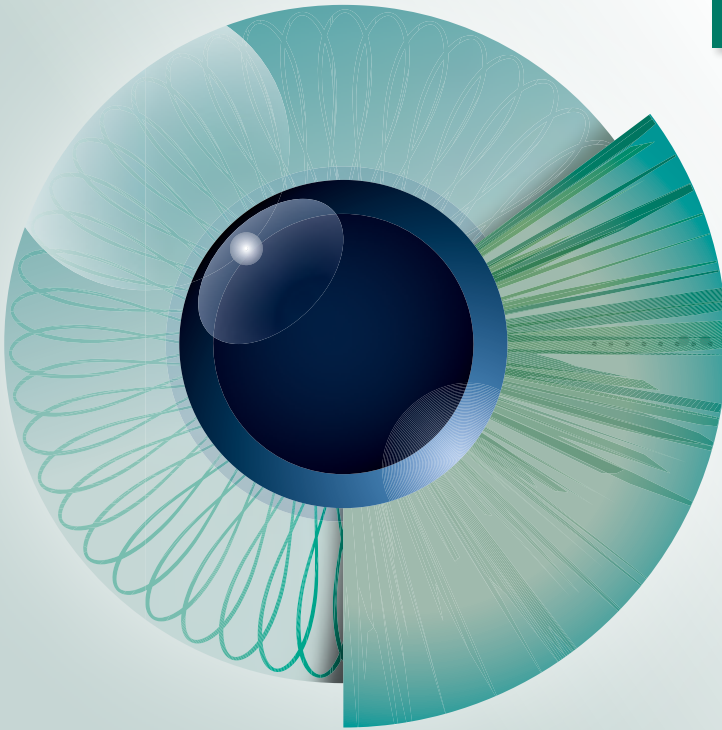# Journal for Modeling in Ophthalmology

MARK YOUR CALENDAR
JUNE 28–JULY 1, 2017

HELSINKI

Please save the date for the 7th
WORLD GLAUCOMA CONGRESS
JUNE 28–JULY 1, 2017
HELSINKI

N
E
S
WGA

THE GLOBAL GLAUCOMA NETWORK
www.worldglaucoma.org

JMO

Journal for Modeling in Ophthalmology

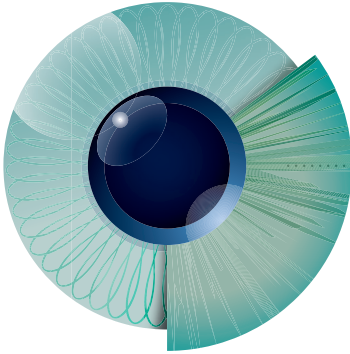**Journal for Modeling in Ophthalmology** (JMO) was created with the aim of providing a forum for interdisciplinary approaches integrating mathematical and computational modeling techniques to address open problems in ophthalmology.

The Editorial Board members include experts in ophthalmology, physiology, mathematics and engineering and strive to ensure the highest scientific level of the contributions selected for publication. JMO aims to be the voice for this rapidly growing interdisciplinary research and we hope you will join us on this exciting journey.

I: www.modeling-ophthalmology.com
E: info@modeling-ophthalmology.com

Copyright

Manuscript submissions

Author guidelines & templates are available via the website, through which all manuscripts should be submitted. For inquiries please contact us via e-mail.

Publication frequency

JMO is published four issues per year (quarterly) electronically. A selection of the best papers is published in print twice a year and distributed free of charge at congresses through Kugler Publications or partners.

Open access policy

The first volume of JMO is fully open access (after reg-istration) without requiring any publication fee from the authors. However, we are currently evaluating various models to cover the publi-cations costs while keeping knowledge as accessible as possible, which remains our first priority. Possible models include subscription fees, publication fees and advertise-ment venues, or a combination. Please share your thoughts with us on this hot topic via e-mail.

Advertising inquiries

JMO offers online and in print sponsorship and advertising opportunities. Please contact Kugler Publications to for inquiries.

Disclaimers

All articles published, including editorials and letters, represent the opinions of the authors and do not reflect the official policy of JMO, its sponsors, the publisher or the institution with which the author is affiliated, unless this is clearly specified. Although every effort has been made to ensure the technical accuracy of the contents of JMO, no responsibility for errors or omissions is accepted. JMO and the publisher do not endorse or guarantee, directly or indirectly, the quality or efficacy of any product or service described the advertisements or other material that is commercial in nature in any issue. All advertising is expected to conform to ethical and medical standards. No responsibility is assumed by JMO or the publisher for any injury and/or damage to persons or property as a matter of products liability, negligence or otherwise, or from any use or operation of any methods, products, instructions, or ideas contained in the material herein. Because of rapid advances in the medical Sciences, independent verification of diagnoses and drug dosages should be made.

Focus and scope

While the rapid advance of imaging technologies in oph-thalmology is making available a continually increasing number of data, the interpretation of such data is still very challenging and this hinders the advance in the understanding of ocular diseases and their treatment. Interdisciplinary approaches encompassing ophthal-mology, physiology, mathematics and engineering have shown great capabilities in data analysis and interpre-tation for advancing basic and applied clinical sciences. The Journal for Modeling in Ophthalmology (JMO) was created in 2014 with the aim of providing a forum for interdisciplinary approaches integrating mathematical and computational modeling techniques to address open problems in ophthalmology. JMO welcomes articles that use modeling techniques to investigate questions related to the anatomy, physiology and function of the eye in health and disease.

For further information and manuscript submissions:
www.modeling-ophthalmology.com
info@modeling-ophthalmology.com

Table of contents

Dear Reader,

It is with great pleasure we welcome you to the inaugural issue of the *Journal for Modeling in Ophthalmology*! It is our shared vision to present a dynamic multi-disciplinary approach towards solving the enigmatic causes of the life altering diseases of blindness.

Throughout our careers in medicine and mathematics, we have both realized that the current echo chambers of singular approaches to medicine and mathematics have produced self-limited contributions to science and medicine. It is likely that many answers to outstanding questions in vision loss are sitting on the shelves of clinical researcher's offices, while the tools to unlock them unknowingly exist across the street with modeling experts in the schools of science or engineering. "Big data analysis" is an innovative approach being brought into many facets of business and computer science, however the barriers of tradition, self-selection, and specialization have impaired the medical community's embrace of these concepts. In a sea of specialized journals, which concentrate solely on clinical or abstract paradigms, our approach is to bridge the gap between theoretical and applied sciences to improve understanding of ocular disease processes, identify new biomarkers, develop advanced screening tools for ocular diseases, and to uncover new therapeutic targets for improved disease management and outcomes.

Advancements in imaging and medical education have identified many biological processes involved in ocular disease pathophysiology. The exact mechanisms involving many identified risk factors and physiological parameters, however, remains insufficiently described. The tired standard statistical approaches to interpreting clinical data continues to provide incremental contributions to understanding ocular pathology, but true breakthroughs to existing hurdles in medicine require a novel collaborative approach.

Dynamic mathematical modeling has begun to reach new levels of applicability and holds the potential to reveal previously unseen synergies of risk or protection within individuals. Many tissues in the eye cannot be visualized with current technologies, and simultaneous measurements of multiple factors are not possible, leaving unanswered questions and limited advancement in clinical understanding of the causes of ocular diseases. Theoretical approaches to solving these issues have a tremendous potential. For instance, advances in dynamic mathematical modeling have recently allowed for the exploration of glaucoma risk factor interconnectivity; providing further insight into glaucoma pathophysiology and eventually may allow for individualized screening and improved patient-specific treatment options.

It is with our shared vision of a multi-disciplinary collaborative approach to preventing ocular disease and blindness that we invite you to join our team. Mathematicians, physicians, statisticians, computer scientists, engineers, physicists, research scientists, and all who seek a fresh approach to dynamic analysis of ocular diseases are joining together to solve the unanswered questions of vision loss. We are excited to invite you to join us, collaborate with us, and bring your individual expertise to the *Journal for Modeling in Ophthalmology* where the best ideas in medicine are brought together with the most advanced modeling and big data analysis available to prevent blindness.

Yours truly,

Alon Harris and Giovanna Guidoboni

Mathematical modeling and glaucoma: the need for an individualized approach to risk assessment

Alice Chandra Verticchio Vercellin[1,2], Alon Harris[1], Jareau Vance Cordell[1], Thai Do[1], James Moroney[3], Aditya Belamkar[1], Brent Siesky[1]

[1]*Department of Ophthalmology, Indiana University School of Medicine, Indianapolis, IN, USA;* [2]*University Eye Clinic, IRCCS Policlinico San Matteo, Pavia, Italy;* [3]*Michigan State University School of Medicine, Grand Rapids, MI, USA*

Abstract

Primary open-angle glaucoma is a chronic optic neuropathy characterized by retinal ganglion cell loss and subsequent visual field impairment. Elevated intraocular pressure remains the only treatable and modifiable risk factor and vascular impairment has been demonstrated in glaucomatous patients. New research has uncovered varying and often contradictory data suggesting more than just a casual correlation with ethnicity, diabetes, gender, obesity and age. Little is known about each variables' contribution to the etiology of glaucoma and how their presence or absence with other risk factors potentiate or reduce an individual's overall risk. The realization that glaucoma is more than a simple, binary disease necessitates a next-generation mathematical model with the capability to integrate individual patient characteristics and clinical risk factors to predict its formation and progression.

Key words: blood flow, disease progression, mathematical modeling, primary open-angle glaucoma, risk factors

Correspondence: Alon Harris, MS, PhD, FARVO, Director of Clinical Research, Lois Letzter Professor of Ophthalmology, Professor of Cellular and Integrative Physiology, Department of Ophthalmology, Indiana University School of Medicine, 1160 West Michigan Street, Indianapolis, IN 46202, USA. E-mail: alharris@indiana.edu

1. Introduction

Glaucoma is the second leading cause of blindness.[1-3] Primary open-angle glaucoma (POAG) is characterized by progressive retinal ganglion cell death and irreversible visual field loss. To date, intraocular pressure (IOP) is the only modifiable risk factor.[4] Despite aggressive medical and surgical treatment, a high percentage of individuals with normal IOP continue to experience disease progression and visual field loss.[1,5-9] The observed progression of POAG despite aggressive IOP management suggests that glaucoma is a multifactorial disease with inadequate surveillance and management.[10] Previous clinical studies have shown changes in blood flow in retinal, choroidal and retrobulbar circulations in POAG.[11-12] Over the last few decades, additional risk factors for POAG have been discovered which include advanced age, ethnic background, family history of glaucoma, decreased central corneal thickness (CCT), higher vertical cup-to-disk ratios (CDR) of the optic disc, and increased pattern standard deviation (PSD) values on Humphrey automated perimeter at baseline.[13] Other patient characteristics including diabetes mellitus (DM), gender, and obesity have been correlated with variation in glaucoma development and differences in glaucoma progression. The mechanisms by which these factors contribute to POAG pathophysiology are still largely unknown. It remains unclear which of these factors are causes or consequences of the disease and whether combinations of different factors yield similar risk for POAG. Without significant advancement in the current understanding of the pathogenesis of glaucoma, the impact of this irreversible blindness on the quality of life worldwide will continue unabated. Due to the heterogeneity of the pathophysiology of glaucoma, it is critical to develop a mathematical model to characterize the probability of glaucoma development and changes in progression based on patient-specific risk factors and known predictive markers of glaucoma development.

1.1. Aqueous humor physiology

Aqueous humor is produced by the non-pigmented epithelium of the ciliary body in the posterior chamber. From there, it flows into the anterior chamber and exits through the trabecular meshwork and Schlemm's canal or the uveoscleral pathway.[14] This traditional model has influenced both our clinical approach and treatment of glaucoma for decades. In highlighting the intrinsically complex interplay of intraocular pressure homeostasis, emerging research in aqueous humor dynamics demonstrates the presence of a third modifiable outflow pathway.[15,16] This additional outlet involves ocular lymphatics, a tissue previously believed to be absent in the eye, within the ciliary body itself. While serving as a potential target for future pharmacological manipulation, this discovery further emphasizes the need for a robust mathematical model that can be dynamically customized and implemented as our understanding of glaucoma evolves.

1.2. Ophthalmological examination in the clinical practice

The ophthalmological examination is a standard tool in ascertaining crucial information about the overall condition of the patient. The eye is often the first part of the body involved in systemic diseases; as a consequence, the ophthalmologist is frequently the first specialist to diagnose a systemic pathology. In particular, several ophthalmic clinical measurements have an important relevance in this field.[17] The assessment of visual acuity can be used as a tool for early diagnosis of diabetic status: a decrease in the visual acuity caused by a myopic shift of the refraction can be for example the first sign of diabetes that causes an increase of the level of the sugar in the aqueous humor. The examination of the fundus oculi, another important part of the ophthalmological examination, can also be informative. In fact, the vessels of the retina represent the only ones in the whole body that can be observed directly and non-invasively by the physician, which can be used to ascertain systemic vessel health. In this sense, the diagnosis and follow up of important systemic conditions, such as diabetes and hypertension, is realized by the periodical examination of the fundus oculi at the slit lamp. Importantly, the retina and the nerve fibers of the optic nerve derived embryological from the neural tube and the eye can be considered as a natural protrusion of the brain. Therefore, neurological disorders can have their first manifestation in the eye. For instance, optic neuritis is frequently the initial sign of multiple sclerosis. Other neurological diseases, such as brain tumors or cerebral ischemia, can be diagnosed with visual field examination, another noninvasive tool that ophthalmologist use in their clinical practice.

In conclusion, important parts of the ophthalmic exam, such as the evaluation of visual acuity, fundus examination through slit lamp and visual field assessment, are noninvasive tools to aid the physician in performing a comprehensive medical evaluation to determine the overall health of an individual.

1.3. Mathematical modeling and glaucoma

Mathematical modeling consists of translating 'real-world problems' into mathematical equations whose solutions simulate the behavior of a physical system.[18] Statistical analysis of experimental and clinical data is one of the most common uses of mathematics in medicine. In the context of glaucoma, mathematical modeling has been used to characterize mechanical response of the optic nerve head (ONH) with variation in IOP, scleral tension and cerebrospinal fluid pressure (CSFP), as well as hemodynamic changes in ocular blood flow and regulation in retinal, choroidal, and ONH vascular beds.[18] Several analytical models attempted to characterize glaucoma progression based on biomechanical changes of the eye, such as scleral thickness, retinal nerve fiber layer (RNFL) thickness and visual functional data.[19-24]

In this review, we will summarize the role of various heterogeneous, confounding factors (ethnicity, diabetic status, gender, obesity, and age) in the pathophysiology of glaucoma, including recent results obtained by our research team in a pilot analysis of POAG patients over a five-year period. Therefore, we will demonstrate

the necessity of comprehensive mathematical modeling capable of predicting the natural course of disease progression, which holds the promise for individualized patient care by incorporating specific characteristics lacking in current models to date.

2. Materials and methods

Electronic databases utilized in the search strategy for journal articles included Pubmed, Google Scholar and Web of Science. Journal article inclusion criteria were based on open-angle glaucoma risk factors for the following populations: European descent, African descent, diabetes, gender, obesity and age. The exclusionary criteria implemented included non-African and non-European ancestry and ophthalmic diseases of intraocular pressure etiology other than open-angle glaucoma. Key words used in search strategy consisted of primary open-angle glaucoma, ethnicity, diabetes, gender, obesity, body-mass index, age, intraocular pressure, risk factors, glaucomatous progression, treatment, mathematical model, optic-head morphology, visual acuity, ocular perfusion pressure and capillary blood flow. Articles were also assessed for open-angle glaucoma diagnostic and treatment paradigms in order to the survey the current literature for up to date methodologies and approaches. Search parameters for article publication date were configured to extrapolate the most recent findings.

2.1. Risk and prognostic factors

2.1.1. Ethnicity
Ethnicity is a known modifier of POAG.[1] Studies have indicated increased incidence and prevalence of POAG in people of African descent (AD) compared to those of European descent (ED).[10,25-27] These patients have increased risk of developing POAG at an earlier age and their disease progression is often more rapid.[28-31] Furthermore, structural differences in persons of AD include thinner corneas, higher percentage of reported DM, high blood pressure and a worse pattern of mean deviation and PSD for standard automated perimetry fields.[30,32-35] Despite studies demonstrating the differences in the development and disease progression of POAG between persons of AD and ED, the mechanisms underlying this disparity have yet been elucidated.

In previous publications, our research group has demonstrated that AD participants with POAG had statistically significant lower retrobulbar blood flow velocities than participants of ED, including lower ophthalmic artery end diastolic velocity, central retinal artery peak systolic velocity, temporal posterior short ciliary arteries peak systolic velocity, and nasal posterior short ciliary arteries peak systolic velocity.[36] Individuals of AD with POAG have been reported to also have higher systolic and diastolic blood pressures than their ED counterparts, including within

the aforementioned data set.[36-37] Although the studies did not focus on causation of these blood pressure differences, the higher systemic blood pressure in the AD cohort with lower localized blood velocity in ocular tissues suggests constriction may be occurring rather than lower delivery force. Whether the systemic and hemodynamic variation in retrobulbar blood flow observed in subjects of AD is due to racial ethnicity alone or in combination with other parameters, such as increased association with DM and systemic hypertension, remains unknown.[30,32-35]

To further clarify the relationship between ethnicity and POAG disease progression, our team analyzed data from a five-year observational study comparing patients of AD and ED. We identified statistically significant differences in the changes from baseline to five years follow-up in the nasal posterior short ciliary arteries end diastolic velocity ($p = 0.0430$) between participants of AD and ED. Furthermore, measurement of retinal capillary blood flow by Heidelberg retinal flowmetry showed an increased area of avascular retinal tissue in subjects of AD ($p = 0.0436$) compared to ED. Baseline inferior RNFL thickness assessed by optical coherence tomography was found to be predictive of structural progression in patients of ED ($p = 0.0048$) but not of AD ($p = 0.6955$), with a statistically significant difference between groups ($p = 0.0379$). The results of previous studies and from our research team suggest that POAG patients of AD have lower retrobulbar blood flow and more retinal capillary dropout associated with their disease progression compared to POAG patients of ED. Whether the observable differences in ocular blood flow between the patient populations is solely dependent on race only or in combination with other parameters remains unclear. The complexity in the heterogeneity of the disease presentation emphasizes the significance of an integrative mathematical model that is capable of incorporating race, in conjunction with other known patient's characteristics, to assist clinicians in predicting patient's specific disease progression.

2.1.2. Diabetes

The association between DM and POAG has been widely investigated; however, the underlying pathophysiology remains poorly understood.[38] Several large-scale population-based cohort studies have reported that DM is a significant risk factor for the development and progression of POAG.[39-41] While others, including the Rotterdam Study, have shown baseline DM status is not predictive of POAG development at 6.5-year follow-up.[42] One postulate is that increased CCT in diabetic patients leads to increased IOP, which, in and of itself, is a major risk factor for POAG progression.[43] There is also evidence that diabetes and elevated IOP together cause increased retinal ganglion cell death.[43] Diabetes may also lead to increased risk of POAG through dysfunctional optic nerve vessels and oxidative damage.[39] To further complicate matters, there is a difference in glaucoma development and progression depending on whether the individual has type-1 diabetes (T1DM) or type-2 diabetes (T2DM). Patients with T1DM have 5.94 times greater risk of developing secondary glaucoma

while patients with T2DM demonstrate a 4.43 times greater risk.[45] Additionally, POAG is more common in patients with non-proliferative diabetic retinopathy than in patients with pre-proliferative or proliferative diabetic retinopathy.[45]

Emerging evidence suggests that impaired ocular perfusion pressure (OPP) and regulation of retinal blood flow observed in diabetic patients contributes to glaucomatous progression.[46] Central retinal artery peak systolic velocity is lower in DM, which correlates to reduce OPP.[46] A negative correlation also exists between retrobulbar blood flow and retinal circulation in DM patients but is absent in non-diabetic patients.[46]

As seen in the studies aforementioned, the role of DM in the onset and progression of glaucoma has not been clearly elucidated. Further to the above-mentioned analysis, our research group investigated the role of retrobulbar and capillary blood flow in diabetic glaucoma patients over a 5-year period. In the analysis of retrobulbar blood flow assessed with color Doppler imaging, a statistically significant difference from baseline to five-year follow-up was demonstrated in the resistivity index of the ophthalmic artery ($p = 0.0017$) and central retinal artery ($p = 0.0482$) between patients with DM compared to those without DM. In addition, the evaluation of the capillary blood flow realized by the Heidelberg retinal flowmetry showed that the area of retinal avascularity at baseline was a predictive factor of structural progression of the disease after five years in glaucoma patients with DM ($p = 0.0297$) but not in those without ($p = 0.5924$), with a statistically significant difference between the two groups ($p = 0.0352$).

Knowing the complexity of the correlation between DM and POAG and the contradictory results of the studies mentioned above, a mathematical model able to incorporate the diabetic status of the patient could aid clinicians in the decision making process to diagnose and manage the disease with an individualized approach.

2.1.3. Gender
Various bodies of glaucoma research have shown incongruent results with respect to analyzing gender disparities. The Blue Mountain Eye Study showed a higher POAG prevalence among women while the group Rudnicka-Ashby *et al.* (2006), found male participants were more likely to develop open angle glaucoma.[47-48] The Framingham and Beaver Dam Eye Studies found that gender was not a risk factor in the development of glaucoma.[49-50]

To date, clear differences in retrobulbar blood flow and its role in glaucoma between men and women have been presented, while others have failed to establish any clear correlation altogether. One study found that men had higher peak systolic velocities, end diastolic velocities, resistive index and pulsatile index (PI) in the ophthalmic artery compared to women. In the same group, women had higher peak systolic velocity, end diastolic velocity, resistive index and PI in the short posterior ciliary arteries compared to men. Interestingly, these results were

more significant in the younger groups than in the older groups.[51] Yet another group who measured the hemodynamic parameters of retrobulbar vessels found no statistically significant difference.[52] In an attempt to unveil the intricacies associated with gender differences, Harris-Yitzhak *et al.* (2000), showed how young women and postmenopausal women receiving estrogen exhibited reduced resistive indices when compared to postmenopausal women not receiving estrogen.[53] Younger women showed greater peak systolic velocity and end diastolic velocity in the short posterior ciliary arteries versus both postmenopausal groups. Conversely, another study found no difference in retinal or retrobulbar blow flow measurements in comparing the effects of Raloxifene on postmenopausal women.[54] Retrobulbar blood vessel caliber analysis in several large studies failed to reveal any differences between males and females.[55-56] These findings suggest the importance of sex hormones as viable candidates to explain retrobulbar blood flow differences among men and women.

In response to the previous contradictory studies, we recently identified, utilizing color Doppler imaging to measure blood flow velocities in POAG patients, a statistically significant difference between gender in the change from baseline to five-year follow-up in the ophthalmic artery end diastolic velocity ($p = 0.0241$) and central retinal artery resistive index ($p = 0.0496$). In addition, the central retinal artery (CRA) peak systolic velocity (PSV) and end diastolic velocity (EDV) were found to be baseline predictive factors of structural progression in open-angle glaucoma patients after five years in males (CRA PSV: $p = 0.0076$; CRA EDV: $p = 0.0131$), but not females, (CRA PSV: $p = 0.5459$; CRA EDV: $p = 0.0604$) with a statistically significant difference between the two groups (CRA PSV: $p = 0.0113$; CRA EDV: $p = 0.0020$). These results further validate gender as an important characteristic in our ever-evolving glaucoma model and illustrate its capricious nature between men and women. While monitoring the blood flow velocities in the ophthalmic artery of males to quantify and track disease burden was highly significant, no equivalent marker was found in women. The likely mechanism for such varying and confusing study results will likely be revealed when mathematical modeling is capable of simulating the multifactorial nature of open angle glaucoma at a personalized level.

2.1.4. Obesity

The rising prevalence of obesity in the United States continues to reach epidemic levels.[57-58] Correlational analysis from several epidemiological studies presents conflicting data.[59-61] To date, the precise relationship between obesity and glaucoma progression remains unclear. In one study, systemic changes associated with obesity and metabolic syndrome, such as insulin resistance and systemic hypertension, were shown to be positively correlated with IOP elevation, which is a risk factor for glaucoma development.[61] It was hypothesized that high systemic blood pressure increases ultrafiltration of the aqueous humor, whereby increasing IOP. In a different retrospective study, primarily of ED individuals, increased BMI

(body mass index) was shown to have neuroprotective effects against glaucoma progression. The study postulated that an increase in translaminar pressure, indicative of IOP and CSFP differences, damages the optic nerve and contributes to glaucomatous optic neuropathy. High CSFP may reduce translaminar pressure, which in turn reduces the risk of glaucoma.[65-66] Results published by our research team agreed are congruent with findings in Berdahl *et al.* (2008).[65-66] We showed that there was a negative correlation between IOP and OPP in overweight (BMI 25-30) and obese (BMI >30) patients; this relationship was not seen in patients with normal BMI (<25).[67] The variation in the results of previous publications further obscures the relationship between weight and POAG development.

Building upon previous studies on obesity and glaucoma progression, we analyzed our 5-years prospective study according to patient's weight. We observed statistically significant changes between patients of normal weight and obese patients from baseline to 5 years follow-up in the following parameters: temporal posterior short ciliary arteries peak systolic velocity (p=0.0118), cup area (p=0.0370), vertical CDR (p=0.0365), macular thickness inner temporal (p=0.0110) and cup volume (p=0.0083). When the overall data was analyzed, without consideration of weight, the change in temporal posterior short ciliary arteries peak systolic velocity was not statistically significant. This suggests the necessity of analyzing epidemiological data with patient-specific factors to reveal their correlational relationship. Moreover, our result on the vertical CDR is varied from a prior publication by Pedro-Egbe *et al.* (2013), which showed no statistically significant correlation between vertical CDR and BMI.[68] Moreover, the baseline BMI category (obese versus normal weight) was a predictive factor of glaucoma structural progression after five years (p = 0.0435). We speculate that factors, such as patient's racial ethnicity, diabetes, gender, weight, and age, may have contributed to the differences reported in previous studies.

Given the diverse results from these various studies, including results from our team, the relationship between obesity and glaucoma progression remains unsettled. To clarify the effect of obesity on POAG development and progression, further advancement in current mathematical models is necessary to integrate multiple demographic parameters to predict disease progression.

2.1.5. Age

Several longitudinal population-based studies have shown that age is a risk factor for the development of POAG in healthy subjects.[42,69-71] The risk of developing glaucoma in subjects who were one year older at baseline was higher by 4% in the Barbados Incidence Study of Eye Diseases and by 6% in the Rotterdam Eye Study.[42,69] In the Melbourne Visual Impairment Project subjects aged 40-49 years old at baseline had a 12-fold lower five-year risk of developing POAG compared to subjects with an age of 70-79 years old at baseline.[71] Older age is also a predictive baseline factor associated with the development of POAG in patients with ocular

hypertension, as demonstrated in the Ocular Hypertension Treatment Study and in the European Glaucoma Prevention Study.[72-73] Finally, results from the Early Manifest Glaucoma Trial have shown that older age at baseline is also a prognostic factor for the progression of POAG.[74]

Knowing the importance of the patient's age not only as a risk factor for the onset of glaucoma but also as a prognostic factor for the disease progression, the role of retrobulbar blood flow in patients with POAG of different ages over a five-year period was investigated in our pilot analysis. The peak systolic velocity (p = 0.0140) and the end diastolic velocity (p = 0.0373) of the ophthalmic artery and the end diastolic velocity of the temporal posterior ciliary arteries (p = 0.0086) were found to be statistically different between subjects aged ≥ 65 compared to subjects aged < 65 as predictive factors of functional progression. Furthermore, we found that baseline age was a predictive factor of functional glaucoma progression after five years (p = 0.0098).

As shown by the aforementioned large population studies and by the recent findings of our research group, age is an important factor in the natural history of glaucoma, playing a well-established role in the disease development and advancement. The formulation of a dynamic mathematical model including subjects' age is clearly needed to allow clinicians to have a tailor approach in the diagnosis and treatment of their glaucomatous patients.

3. Conclusion

Our review of previous research shows that POAG patients of varying race, diabetic status, gender, obesity, and age differ in terms of their initial presentation and subsequent progression. The manner in which these systemic and ocular physiological parameters change, both in terms of structure and function, are highly variable in disease progression. Additional studies will allow the creation of a dynamic model needed to understand the highly complex interactions between each of the aforementioned variables, as well as their role in the pathogenesis and natural history of glaucoma.

Mathematical modeling in medicine is often utilized for its intrinsic ability to use the predictive values of known risk factors to forecast the development of certain diseases. Such algorithms have been employed to characterize glaucoma progression based on biomechanical changes of the eye and its ocular hemodynamics. However, efforts to quantify the complex nature of these systemic factors to provide comprehensive modeling of glaucoma development and progression are incomplete and ongoing. Based on our summarized results in this review, we advocate for the need to establish mathematical modeling so that the predictive values of known risk factors can be used to correctly identify patients with the highest risk of developing glaucoma. This comprehensive dynamic model will

include vital demographic characteristics, such as race, diabetic status, gender, obesity, and age that will allow physicians the ability to confidently provide clear, individualized, evidence based approach for each of their patients.

Acknowledgement

References

1. Leske MC. Open-angle glaucoma: an epidemiological overview. Ophthalmic Epidemiol 2007;14(4):166-172. Available from: http://www.diseaseinfosearch.org/result/3065 PubMed PMID: 17896292. doi: 10.1080/09286580701501931.

2. Kingman S. Glaucoma is second leading cause of blindness globally. Bull World Health Organ 2004;82(11):887-8.

3. Cook C, Foster P. Epidemiology of glaucoma: what's new?. Can J Ophthalmol 2012;47(3):223-226. Available from: http://www.diseaseinfosearch.org/result/3065 PubMed PMID: 22687296. doi: 10.1016/j.jcjo.2012.02.003.

4. Grewe R. [The history of glaucoma].. Klin Monbl Augenheilkd 1986;188(2):167-169. Available from: http://www.diseaseinfosearch.org/result/3065 PubMed PMID: 3520122. doi: 10.1055/s-2008-1050606.

5. Leske MC, Heijl A, Hyman L, Bengtsson B, Dong L, Yang Z. Predictors of long-term progression in the early manifest glaucoma trial.. Ophthalmology 2007;114(11):1965-1972. Available from: http://www.scholaruniverse.com/ncbi-linkout?id=17628686 PubMed PMID: 17628686. doi: 10.1016/j.ophtha.2007.03.016.

6. Caprioli J, Coleman AL. Intraocular pressure fluctuation a risk factor for visual field progression at low intraocular pressures in the advanced glaucoma intervention study.. Ophthalmology 2008 Feb;115(7):1123-1129. Available from: http://www.scholaruniverse.com/ncbi-linkout?id=18082889 PubMed PMID: 18082889. doi: 10.1016/j.ophtha.2007.10.031.

7. Caprioli J, Coleman AL. Blood flow in glaucoma discussion; blood pressure, perfusion pressure, and glaucoma. Am J Ophthalmol 2010;149(5):704-712. Available from: http://www.diseaseinfosearch.org/result/3065 PubMed PMID: 20399924. doi: 10.1016/j.ajo.2010.01.018.

8. Danias J, Podos SM. Comparison of glaucomatous progression between untreated patients with normal-tension glaucoma and patients with therapeutically reduced intraocular pressures. The effectiveness of intraocular pressure reduction in the treatment of normal-tension glaucoma. Am J Ophthalmol 1999;127(5):623-5.

9. Ehrnrooth P, Puska P, Lehto I, et al. Progression of visual field defects and visual loss in trabeculectomized eyes. Graefes Arch Clin Exp Ophthalmol 2005;243(8):741-747. Available from: https://www.researchgate.net/publication/e/pm/15700183?ln_t=p&ln_o=linkout PubMed PMID: 15700183. doi: 10.1007/s00417-004-1088-3.

10. Tielsch JM, Sommer A, Katz J, et al. Racial variations in the prevalence of primary open angle glaucoma, the baltimore eye survey. JAMA 1991 Jul;266(3):369-74. Available from: http://www.scholaruniverse.com/ncbi-linkout?id=2056646 PubMed PMID: 2056646. doi: 10.1001/jama.1991.03470030069026.

11. Chung HS, Harris A, Kagemann L, Martin B. Peripapillary retinal blood flow in normal tension glaucoma.. Br J Ophthalmol 1999;83(4):466-469. Available from: http://bjo.bmj.com/cgi/pmidlookup?view=long&pmid=10434872 PubMed PMID: 10434872. doi: 10.1136/bjo.83.4.466.

12. Harris A, Sergott RC, Spaeth . GL et al. Color Doppler analysis of ocular vessel blood velocity in normal-tension glaucoma. Am J Ophthalmol 1994;118(5):642-9. Available from: http://linkinghub.elsevier.com/retrieve/pii/S0002939414765791 doi: 10.1016/S0002-9394(14)76579-1.

13. Coleman AL, Caprioli J. The logic behind target intraocular pressure. Am J Ophthalmol 2009;147(3):379-80. Available from: http://linkinghub.elsevier.com/retrieve/pii/S0002939408008854 doi: 10.1016/j.ajo.2008.10.027.

14. Harris A, Guidoboni G, Arciero JC, et al. Ocular hemodynamics and glaucoma: The role of mathematical modeling. Eur J Ophthalmol 2013 Mar;23(2):139-46. doi: 10.5301/ejo.5000255.

15. Karpinich NO, Caron KM. Schlemm's canal: more than meets the eye, lymphatics in disguise. The Journal of Clinical Investigation. 2014 2014 Jul;124(9):3701-3703. Available from: http://europepmc.org/abstract/MED/25061871 PubMed PMID: 25061871. doi: 10.1172/JCI77507.

16. Truong TN, Li H, Hong Y, Chen L. Novel characterization and live imaging of Schlemm's canal expressing Prox-1.. PLoS One 2014 May;9(5):579-84. Available from: http://dx.plos.org/10.1371/journal.pone.0098245 PubMed PMID: 24827370. doi: 10.1371/journal.pone.0098245.

17. Kansky JJ. Clinical ophthalmology: A systemic approach. Seventh edition. Elsevier; 2011.

18. Harris A, Guidoboni G, Arciero JC, et al. Ocular hemodynamics and glaucoma: The role of mathematical modeling. Eur J Ophthalmol 2013;23(2):139-146. Available from: http://www.eur-j-ophthalmol.com/article/ocular-hemodynamics-and-glaucoma--the-role-of-mathematical-modeling   PubMed PMID: 23413108. doi: 10.5301/ejo.5000255.

19. Norman RE, Flanagan JG, Sigal IA, Rausch SMK, Tertinegg I, Ethier, C. Ross . Finite element modeling of the human sclera: Influence on optic nerve head biomechanics and connections with glaucoma. Experimental Eye Research 2011;93(1):4-12. Available from: http://linkinghub.elsevier.com/retrieve/pii/S001448351000309X PubMed PMID: 20883693. doi: 10.1016/j.exer.2010.09.014.

20. Dongqi H, Zeqin R. A biomathematical model for pressure-dependent lamina cribrosa behavior. J Biomech 1999;32(6):579-584. Available from: http://linkinghub.elsevier.com/retrieve/pii/S0021929099000251 PubMed PMID: 10332621. doi: 10.1016/S0021-9290(99)00025-1.

21. Bellezza AJ, Hart RT, Burgoyne CF. The optic nerve head as a biomechanical structure: initial finite element modeling.. Invest Ophthalmol Vis Sci 2000;41(10):2991-3000. Available from: http://www.scholaruniverse.com/ncbi-linkout?id=10967056 PubMed PMID: 10967056.

22. Sigal IA, Flanagan JG, Tertinegg I, Ethier CR. Finite element modeling of optic nerve head biomechanics. Invest Ophthalmol Vis Sci 2004;45(12):4378-4387. Available from: http://iovs.arvojournals.org/article.aspx?doi=10.1167/iovs.04-0133 PubMed PMID: 15557446. doi: 10.1167/iovs.04-0133.

23. Yousefi S, Goldbaumn M, Balasubramanian M, et al. Glaucoma progression detection using structural retinal nerve fiber layer measurements and functional visual field points. IEEE Trans Biomed Eng 2014;61(4):1143-1154. Available from: http://europepmc.org/abstract/MED/24658239 PubMed PMID: 24658239. doi: 10.1109/TBME.2013.2295605.

24. Newson T, El-Sheikh A. "Mathematical modeling of the biomechanic of the laimina cribrosa under elevated intraocular pressures. " J Biomech Eng 2006;128(4):496-504. Available from: http://Biomechanical.asmedigitalcollection.asme.org/article.aspx?articleid=1415626 doi: 10.1115/1.2205372.

25. Leske MC, Connell AM, Schachat AP, et al. The Barbados eye study, prevalence of open angle glaucoma. Arch Ophthalmol 1994;112(6):821-9. Available from: http://archopht.jamanetwork.com/article.aspx?doi=10.1001/archopht.1994.01090180121046 PubMed PMID: 8002842. doi: 10.1001/archopht.1994.01090180121046.

26. Mason RP, Kosoko O, Wilson MR, et al. National survey of the prevalence and risk factors of glaucoma in St. Lucia, West Indies. Part I. Prevalence findings. Ophthalmology 1989;96(9):1363-1368. Available from: http://linkinghub.elsevier.com/retrieve/pii/S0161642089327084 doi: 10.1016/S0161-6420(89)32708-4.

27. Rotchford AP, Kirwan JF, Muller MA, et al. Temba glaucoma study: A population-based crosssectional survey in urban South Africa. Ophthalmology 2003;110(2):376-82. Available from: http://linkinghub.elsevier.com/retrieve/pii/S0161642002015683 doi: 10.1016/S0161-6420(02)01568-3.

28. Gordon MO, Beiser JA, Brandt JD, Heuer DK, Higginbotham EJ, Johnson CA, et al. The Ocular Hypertension Treatment Study: baseline factors that predict the onset of primary open-angle glaucoma.. Arch Ophthalmol 2002;120(6):714-720. Available from: http://www.scholaruniverse.com/ncbi-linkout?id=12049575 PubMed PMID: 12049575. doi: 10.1167/iovs.14-15719.

29. Martin MJ, Sommer A, Gold EB, Diamond EL. Race and primary open-angle glaucoma.. Am J Ophthalmol 1985 Apr;99(4):383-387. Available from: http://www.diseaseinfosearch.org/result/3065 PubMed PMID: 3985075. doi: 10.1001/archophthalmol.2010.49.

30. Racette L, Liebmann JM, Girkin CA, Zangwill LM, Jain S, Becerra LM, et al. African Descent and Glaucoma Evaluation Study (ADAGES): III. Ancestry differences in visual function in healthy eyes.. Arch Ophthalmol 2010;128(5):551-559. Available from: http://europepmc.org/abstract/MED/20457975 PubMed PMID: 20457975. doi: 10.1001/archophthalmol.2010.58.

31. Racette L, Wilson MR, Zangwill LM, et al. Primary open-angle glaucoma in blacks: A review. Surv Ophthalmol 2003;48(3):295-313. Available from: http://www.scholaruniverse.com/ncbi-linkout?id=12745004 PubMed PMID: 12745004. doi: 10.1001/archophthalmol.2009.187.

32. Girkin CA, Nievergelt CM, Kuo JZ, Maihofer AX, Huisingh C, Liebmann JM, et al. Biogeographic Ancestry in the African Descent and Glaucoma Evaluation Study (ADAGES): Association With Corneal and Optic Nerve Structure.. Invest Ophthalmol Vis Sci 2015 Mar;56(3):2043-2049. Available from: http://europepmc.org/abstract/MED/25744975 PubMed PMID: 25744975. doi: 10.1167/iovs.14-15719.

33. Girkin CA, Sample PA, Liebmann JM, Jain S, Bowd C, Becerra LM, et al. African Descent and Glaucoma Evaluation Study (ADAGES): II. Ancestry differences in optic disc, retinal nerve fiber layer, and macular structure in healthy subjects.. Arch Ophthalmol 2010;128(5):541-550. Available from: http://europepmc.org/abstract/MED/20457974 PubMed PMID: 20457974. doi: 10.1001/archophthalmol.2010.49.

34. Moore GH, Bowd C, Medeiros FA. African Descent and Glaucoma Evaluation Study (ADAGES): Asymmetry of structural measures in normal participants. J Glaucoma 2015 Feb;2013(1):22-2. doi: 10.4239/wjd.v6.i1.92.

35. Sample PA, Girkin CA, Zangwill LM, Jain S, Racette L, Becerra LM, et al. The African Descent and Glaucoma Evaluation Study (ADAGES): design and baseline data.. Arch Ophthalmol 2009;127(9):1136-1145. Available from: http://europepmc.org/abstract/MED/19752422 PubMed PMID: 19752422. doi: 10.1001/archophthalmol.2009.187.

36. Siesky B, Harris A, Racette L, Abassi R, Chandrasekhar K, Tobe LA, et al. Differences in ocular blood flow in glaucoma between patients of African and European descent.. J Glaucoma 2015;24(2):117-121. Available from: http://content.wkhealth.com/linkback/openurl?sid=WKPTLP:landingpage&an=00061198-201502000-00005 PubMed PMID: 23807346. doi: 10.1097/IJG.0b013e31829d9bb0.

37. Kanakamedala P, Harris A, Siesky B, Tyring A, Muchnik M, Eckert G, et al. Optic nerve head morphology in glaucoma patients of African descent is strongly correlated to retinal blood flow. Br J Ophthalmol 2014 Jun;98(11):1551-1554. Available from: http://europepmc.org/abstract/MED/24964797 PubMed PMID: 24964797. doi: 10.1136/bjophthalmol-2013-304393.

38. Sayin N, Kara N, and Pekel G . Ocular complications of Diabetes Mellitus. World J Diabetes 2015 Feb;6(1):92-108. Available from: http://www.wjgnet.com/1948-9358/full/v6/i1/92.htm doi: 10.4239/wjd.v6.i1.92.

39. Newman-Casey PA, Talwar N, Nan B, et al. The relationship between components of metabolic syndrome and open-angle glaucoma. Ophthalmology 2011;118(7):1318-1016. Available from: http://europepmc.org/abstract/MED/21481477 PubMed PMID: 21481477. doi: 10.1016/j.ophtha.2010.11.022.

40. Chopra V, Varma R, Francis BA, et al. Type 2 Diabetes Mellitus and the risk of open-angle glaucoma the Los Angeles Latino Eye Study. Ophthalmology 2008;115(2):227-232. Available from: http://www.scholaruniverse.com/ncbi-linkout?id=17716734 PubMed PMID: 17716734. doi: 10.1016/j.ophtha.2007.04.049.

41. Zhou M, Wang W, Huang W. Diabetes Mellitus as a risk factor for open-angle glaucoma: A Systematic Review and Meta-Analysis. PloS One. 2014 Aug 2006;19(9):10-1371.

42. Voogd, S. de, , Ikram MK, Wolfs RC, et al. Is Diabetes Mellitus a risk factor for open-angle glaucoma? The Rotterdam Study. Ophthalmology 2006;113(10):1827-31. Available from: http://linkinghub. elsevier.com/retrieve/pii/S0161642006006920 doi: 10.1016/j.ophtha.2006.03.063.

43. Ozdamar Y, Cankaya B, Ozalp S. Is There a correlation between Diabetes Mellitus and central corneal thickness. J Glaucoma 1992;2010:19-9.

44. Kanamori A, Nakamura M, Mukuno H, Maeda H, Negi A. Diabetes has an additive effect on neural apoptosis in rat retina with chronically elevated intraocular pressure. Curr Eye Res 2004;28(1):47-54. Available from: https://www.researchgate.net/publication/e/pm/14704913?ln_t=p&ln_o=linkout PubMed PMID: 14704913. doi: 10.1076/ceyr.28.1.47.23487.

45. Halilovic EA, Ljaljevic S, Alimanovic I, et al. Analysis of the Influence of Type of Diabetes Mellitus on the Development and Type of Glaucoma. Medical Archives 2015;69(1):34-7. Available from: http:// www.scopemed.org/?mno=180720 PubMed PMID: 25870475. doi: 10.5455/medarh.2015.69.34-37.

46. Shoshani Y, Harris A, Shoja MM, et al. Impaired ocular blood flow regulation in patients with openan-gle glaucoma and diabetes. Clin Experiment Ophthalmol 2012;40(7):697-705. Available from: http:// doi.wiley.com/10.1111/j.1442-9071.2012.02778.x doi: 10.1111/j.1442-9071.2012.02778.x.

47. Mitchell P, Smith W, Attebo K, Healey PR. Prevalence of open-angle glaucoma in Australia. The Blue Mountains Eye Study.. Ophthalmology 1996;103(10):1661-1669. Available from: http://linkin-ghub.elsevier.com/retrieve/pii/S0161642096304491 PubMed PMID: 8874440. doi: 10.1016/S0161-6420(96)30449-1.

48. Rudnicka AR, Mt-Isa S, Owen CG, Cook DG, Ashby D. Variations in primary open-angle glaucoma prevalence by age, gender, and race: a Bayesian meta-analysis.. Invest Ophthalmol Vis Sci 2006;47(10):4254-4261. Available from: http://www.scholaruniverse.com/ncbi-linkout?id=17003413 PubMed PMID: 17003413. doi: 10.1167/iovs.06-0299.

49. Khan HA, Leibowitz HM, Ganley JP, et al. The Framingham Eye Study. II. Association of ophthalmic pathology with single variables previously measured in the Framingham Heart Study. Am J Epidemi-ol 1977;106(1):33-41. Available from: https://www.nlm.nih.gov/medlineplus/cataract.html PubMed PMID: 141882.

50. Klein BE, Klein R, Sponsel WE, Franke T, Cantor LB, Martone J, et al. Prevalence of glaucoma. The Beaver Dam Eye Study.. Ophthalmology 1992;99(10):1499-1504. Available from: http://www. scholaruniverse.com/ncbi-linkout?id=1454314 PubMed PMID: 1454314. doi: 10.1016/S0161-6420(92)31774-9.

51. Ustymowicz A, Mariak Z, Weigele J, Lyson T, Kochanowicz J, Krejza J. Normal reference intervals and ranges of side-to-side and day-to-day variability of ocular blood flow Doppler parameters. Ultrasound Med Biol 2005;31(7):895-903. Available from: https://www.researchgate.net/publica-tion/e/pm/15972195?ln_t=p&ln_o=linkout PubMed PMID: 15972195. doi: 10.1016/j.ultrasmed-bio.2005.03.013.

52. Marjanovic I, Marjanovic M, Gvozdenovic R, et al. Retrobulbar heodynamic parameters in men and women with open angle glaucoma. Voinosanit Pregl 2014;71(12):1128-31. Available from: http:// www.doiserbia.nb.rs/Article.aspx?ID=0042-84501412128M doi: 10.2298/VSP1412128M.

53. Harris-Yitzhak M, Harris A, Ben-Refael Z, et al. Estrogen-replacement therapy: effects on retrobulbar hemodynamics. Am J Ophthalmol 2000;129(5):623-628. Available from: http://www.scholaruniverse. com/ncbi-linkout?id=10844054 PubMed PMID: 10844054. doi: 10.1016/S0002-9394(99)00468-7.

54. Siesky B, Harris A, Kheradiya N, Ehrlich R, Klaas C, Kaplan B, et al. The effects of raloxifene hydrochlo-ride on ocular hemodynamics and visual function. Int Ophthalmol 2008 Apr;29(4):225-230. Available from: http://www.scholaruniverse.com/ncbi-linkout?id=18427730 PubMed PMID: 18427730. doi: 10.1007/s10792-008-9224-4.

55. Wang S, Xu L, Wang Y, Wang Y, Jonas JB. Retinal vessel diameter in normal and glaucomatous eyes: the Beijing eye study.. Clin Experiment Ophthalmol 2007;35(9):800-807. Available from: https://

www.nlm.nih.gov/medlineplus/glaucoma.html PubMed PMID: 18173406. doi: 10.1111/j.1442-9071.2007.01627.x.

56. Wong TY, Klein R, Klein BEK, Meuer SM, Hubbard LD. Retinal vessel diameters and their associations with age and blood pressure.. Invest Ophthalmol Vis Sci 2003;44(11):4644-4650. Available from: http://iovs.arvojournals.org/article.aspx?doi=10.1167/iovs.03-0079 PubMed PMID: 14578380. doi: 10.1167/iovs.03-0079.

57. Ogden C, Carroll M, Kit B, et al. Prevalence of childhood and adult obesity in the United States, 2011-2012. JAMA 2014 Feb;311(8):806-14. Available from: http://jama.jamanetwork.com/article.aspx?doi=10.1001/jama.2014.732 doi: 10.1001/jama.2014.732.

58. Finkelstein EA, Khavjou OA, Thompson H, Trogdon JG, Pan L, Sherry B, et al. Obesity and severe obesity forecasts through 2030.. Am J Prev Med 2012;42(6):563-570. Available from: http://linkinghub.elsevier.com/retrieve/pii/S0749379712001468 PubMed PMID: 22608371. doi: 10.1016/j.amepre.2011.10.026.

59. Yoshida M, Ishikawa M, Karita K, et al. Association of blood pressure and body mass index with intraocular pressure in middle-aged and older Japanese residents: a cross-sectional and longitudinal study. Acta Med Okayama 2015;68(1):27-34. Available from: http://www.lib.okayama-u.ac.jp/www/acta/pdf/68_1_27.pdf PubMed PMID: 24553486. doi: 10.1167/iovs.08-2228.

60. Geloneck MM, Crowell EL, Wilson EB, Synder BE, Chuang AZ, Baker LA, et al. Correlation between intraocular pressure and body mass index in the seated and supine positions.. J Glaucoma 2015;24(2):130-134. Available from: https://www.nlm.nih.gov/medlineplus/obesity.html PubMed PMID: 24247996. doi: 10.1097/01.ijg.0000435775.05032.87.

61. Sw OH, Lee S, Park C, et al. Elevated intraocular pressure is associated with insulin resistance and metabolic syndrome. Diabetes Metab Res Rev 2005;21(5):434-40.

62. Gasser P, Stümpfig D, Schötzau A, Ackermann-Liebrich U, Flammer J. Body mass index in glaucoma.. J Glaucoma 1999;8(1):8-11. Available from: http://www.diseaseinfosearch.org/result/3065 PubMed PMID: 10084268.

63. Asrani S, Samuels B, Thakur M, Santiago C, Kuchibhatla M. Clinical profiles of primary open angle glaucoma versus normal tension glaucoma patients: a pilot study.. Curr Eye Res 2011;36(5):429-435. Available from: http://www.diseaseinfosearch.org/result/3065 PubMed PMID: 21501076. doi: 10.3109/02713683.2011.559563.

64. Kang JH, Loomis SJ, Rosner BA, et al. Comparison of risk factor profiles for primary open-angle glaucoma subtypes defined by pattern of visual field loss: a prospective study. Invest Ophthalmolmol Vis Sci 2015;56(4):2439-48. Available from: http://europepmc.org/abstract/MED/25758813 PubMed PMID: 25758813. doi: 10.1167/iovs.14-16088.

65. Berdahl JP, Allingham RR, Johnson DH. Cerebrospinal fluid pressure is decreased in primary open-angle glaucoma. Ophthalmology 2008;115(6):763-8. Available from: http://linkinghub.elsevier.com/retrieve/pii/S016164200800064X doi: 10.1016/j.ophtha.2008.01.013.

66. Berdahl JP, Fautsch MP, Stinnet SS, et al. Intracranial pressure in primary open angle glaucoma, normal tension glaucoma, and ocular hypertension: a case-control study. Invest Ophthalmol Vis Sci 2008;49(12):5412-8. Available from: http://europepmc.org/abstract/MED/18719086 PubMed PMID: 18719086. doi: 10.1167/iovs.08-2228.

67. Ngo S, Harris A, Sieksy BA, et al. Blood pressure, ocular perfusion pressure, and body mass index in glaucoma patients. Eur J Ophthal 2013;23(5):664-9. Available from: http://www.eur-j-ophthalmol.com/article/blood-pressure--ocular-perfusion-pressure--and-body-mass-index-in-glaucoma-patients doi: 10.5301/ejo.5000257.

68. Pedro-Egbe C and Awoyesuku E . The relationship between vertical cup-disc ratio and body mass index in Port Harcourt, Nigeria. Niger J Clin Pract 2013;16(4):517-20. Available from: http://www.njcponline.com/text.asp?2013/16/4/517/116904 PubMed PMID: 23974750. doi: 10.4103/1119-

3077.116904.

69. Leske MC, Wu SY, Hennis A et al. Risk factors for incident open-angle glaucoma: The Barbados Eye Studies. Ophthalmology 2008;115(1):85-93. Available from: http://linkinghub.elsevier.com/retrieve/pii/S0161642007002424 doi: 10.1016/j.ophtha.2007.03.017.

70. Müskens RPHM, de Voogd S, Wolfs RCW, Witteman JCM, Hofman A, de Jong PTVM, et al. Systemic antihypertensive medication and incident open-angle glaucoma.. Ophthalmology 2007;114(12):2221-2226. Available from: http://www.scholaruniverse.com/ncbi-linkout?id=17568677 PubMed PMID: 17568677. doi: 10.1016/j.ophtha.2007.03.047.

71. Le A, Mukesh BN, McCarty CA, Taylor HR. Risk factors associated with the incidence of open-angle glaucoma: the visual impairment project.. Invest Ophthalmol Vis Sci 2003;44(9):3783-3789. Available from: http://iovs.arvojournals.org/article.aspx?doi=10.1167/iovs.03-0077 PubMed PMID: 12939292. doi: 10.1167/iovs.03-0077.

72. Kass MA, Heuer DK, Higginbotham EJ, Johnson CA, Keltner JL, Miller JP, et al. The Ocular Hypertension Treatment Study: a randomized trial determines that topical ocular hypotensive medication delays or prevents the onset of primary open-angle glaucoma.. Arch Ophthalmol 2002;120(6):701-713. Available from: http://www.scholaruniverse.com/ncbi-linkout?id=12049574 PubMed PMID: 12049574.

73. Miglior S, Zeyen T, Pfeiffer N, Cunha-Vaz J, Torri V, Adamsons I. Results of the European Glaucoma Prevention Study.. Ophthalmology 2005;112(3):366-375. Available from: http://www.diseaseinfosearch.org/result/3065 PubMed PMID: 15745761. doi: 10.1016/j.ophtha.2004.11.030.

74. Heijl A, Leske MC, Bengtsson B, Hyman L, Bengtsson B, Hussein M. Reduction of intraocular pressure and glaucoma progression: results from the Early Manifest Glaucoma Trial.. Arch Ophthalmol 2002;120(10):1268-1279. Available from: http://archopht.jamanetwork.com/article.aspx?doi=10.1001/archopht.120.10.1268 PubMed PMID: 12365904. doi: 10.1001/archopht.120.10.1268.

Can diagnostic accuracy for early glaucoma be improved in Japanese? A trial with a potential new parameter of the RTVue OCT

Yoshiyuki Kita[1], Gábor Holló[2], Ritsuko Kita[1]

[1]*Department of Ophthalmology, Toho University Ohashi Medical Center, Tokyo, Japan;*
[2]*Department of Ophthalmology, Semmelweis University, Budapest, Hungary*

Abstract

Aim: To evaluate the diagnostic accuracy of the ratio of circumpapillary retinal nerve fiber layer thickness (cpRNFLT) to macular outer retinal thickness (R/O ratio) and the ratio of ganglion cell complex (GCC) thickness to outer retinal thickness (G/O ratio) measured with the RTVue-100 Fourier-domain optical coherence tomograph for detecting early glaucoma in Japanese eyes.

Methods: Forty-seven healthy control, 31 preperimetric and 70 early perimetric glaucoma eyes. We used cpRNFLT and macular retinal thickness measurements to calculate new ratio parameters, and to compare their diagnostic accuracy to those of the manufacturer-provided parameters of the RTVue-100. The ability of each parameter to diagnose glaucoma was examined by comparing the area under the receiver-operating characteristics curve (AUROC).

Results: AUROC values for the healthy vs. preperimetric glaucoma comparison were 0.842, 0.859, and 0.925 for average cpRNFLT, average R/O ratio, and average G/O ratio, respectively. For the healthy vs. early perimetric glaucoma comparison the AUROC values were 0.927, 0.933, and 0.979 for cpRNFLT, R/O ratio, and G/O ratio, respectively. Diagnostic accuracy of the R/O ratio and cpRNFLT did not differ significantly (P > 0.05). Diagnostic accuracy for the G/O ratio was significantly greater than the cpRNFLT in early glaucoma (P < 0.05).

Conclusions: Use of the G/O ratio is recommended for the detection of early glaucoma in Japanese eyes.

Correspondence: Yoshiyuki Kita, Department of Ophthalmology, Kyorin University School of Medicine, 6-20-2 Shinkawa, Mitaka, Tokyo, 181-8611, Japan.
E-mail: kitakita220@gmail.com

Key words: ganglion cell complex, outer retinal thickness, ratio, preperimetric glaucoma, retinal nerve fiber layer thickness

1. Introduction

In the last decade, Fourier-domain optical coherence tomography (FD-OCT) has gained importance for detecting glaucoma.[1-3] A decrease in the circumpapillary retinal nerve fiber layer thickness (cpRNFLT) is frequently detected in the early stages of glaucoma,[4-6] although the normal cpRNFLT range is wide: it varies between 79.5[5] and 131.4 μm, and its overlap with cpRNFLT in preperimetric glaucoma (reported range: 60.2 to 114.4 μm) is considerable.[7] The variability of cpRNFLT in normal eyes is likely influenced by the axial length, refractive error, age, disc size, image quality, and race.[8-13] In addition, it has been shown that various manufacturer-provided and investigator-generated FD-OCT parameters perform differently in Japanese and Caucasian eyes.[10,14,1] Japanese eyes, like many Asian eyes, are have higher axial length and therefore they are typically more myopic than Caucasian eyes.[16] This can be considered as a reason of the different relationship between macular ganglion cell complex (GCC) thickness and macular outer retina thickness (OR) thickness in Japanese and Caucasian eyes: GCC and OR thickness correlate significantly in Japanese eyes, but they do not correlate Caucasian eyes.[14] Therefore, to further increase the diagnostic value of FD-OCT for detecting early glaucoma in Japanese patients, we investigated novel FD-OCT parameters and parameter ratios with smaller normal ranges[17] and compared them with the standard FD-OCT parameters for clinical usefulness. We recently reported that the GCC to total retinal thickness ratio (the G/T ratio) is useful for diagnosing perimetric glaucoma in Japanese eyes with myopia.[17] Furthermore, since GCC thickness correlated significantly with OR thickness in normal eyes and glaucoma, the GCC to OR thickness ratio (the G/O ratio) is a suitable parameter to account for variation in the OR thickness, and the G/O ratio has a smaller normal range.[17,18] These parameters are not affected by the axial length.[18] Since cpRNFLT and GCC thickness decrease in glaucoma and OR thickness is not affected by the glaucomatous ganglion cell and axon loss,[17,18,20,21] in the present study, we investigated whether the thickness ratio of cpRNFLT and OR (R/O ratio) and the G/O ratio offer an advantage over the existing manufacturer-provided FD-OCT parameters for detecting preperimetric and early perimetric glaucoma.

2. Materials and methods

In total, 148 consecutive Japanese subjects (47 normal patients and 101 patients with primary open-angle glaucoma) examined between October 2009 and March

2013 at the Toho University Ohashi Medical Center Department of Ophthalmology (Tokyo, Japan) were retrospectively selected from a research database. One eye in each subject was randomly selected as the study eye. The Toho University Ohashi Medical Center Institutional Review Board for Human Research approved the study protocol (No.12-87), and the study conduct adhered to the tenets of the Declaration of Helsinki.

All study participants underwent a complete ophthalmologic examination that included visual acuity testing (with determination of refractive error), slit-lamp biomicroscopy, gonioscopy, Goldmann applanation tonometry, and dilated stereoscopic fundus examination. Noncycloplegic refraction was measured using an auto-refracto/keratometer (ARK-530A; Nidek, Aichi, Japan). Refraction data were converted to the spherical equivalent, defined as the spherical power (in diopters) plus half the cylindrical power. Visual fields were considered reliable when fixation losses were < 20% and false-positive and false-negative rates were < 15%. An abnormal visual field result was defined as an abnormal range on the glaucoma hemifield test, a pattern standard deviation of < 5%, or three abnormal points (< 5% probability of being normal), with one point having a pattern deviation of < 1%.

To be included in the normal eye group, healthy control subjects had to have normal intraocular pressure (IOP; < 21 mmHg) and normal optic nerve head (ONH) appearance, open anterior chamber angles, a normal and reliable visual field test result on the Swedish interactive threshold algorithm (SITA) 24-2 standard test of the Humphrey Field Analyzer (HVF, Humphrey-Zeiss Systems, Dublin, CA), a best-corrected visual acuity of 20/20 or better, a refractive spherical error between +3.00 and -6.00 diopters, and a refractive cylindrical error of < 3.0 diopters. An eye was considered to have a normal optic nerve head if the stereoscopic fundus examination revealed a vertical cup-to-disc ratio of < 0.7 (although in Japanese eyes the disc area is similar to that in European eyes, the cup-to-disc ratio of healthy Japanese eyes is usually higher than that of healthy Caucasian eyes10), a uniform neuroretinal rim, no retinal nerve fiber layer (RNFL) defects, and no optic nerve abnormalities (e.g., diffuse or localized rim thinning, disc hemorrhage, or an interocular difference in vertical cup-to-disc ratio > 0.2). The subjects were not included if they had a possible history of elevated IOP (*e.g.*, iridocyclitis, trauma), intraocular eye disease, or any other condition that may have affected the visual field (*e.g.*, pituitary lesions, demyelinating diseases, diabetic retinopathy). Subjects were also excluded if they had a history of intraocular surgery or retinal laser procedures.

For inclusion in the early perimetric glaucoma group, patients had to have a best-corrected visual acuity of 20/20 or better, a refractive spherical error between +3.00 and -6.00 diopters, a refractive cylindrical error of < 3.0 diopters, open anterior chamber angles (determined with gonioscopy), glaucomatous optic neuropathy (GON) and corresponding HVF abnormalities (mean deviation (MD) value up to -6 dB) on reliable and reproducible SITA 30-2 test, and the diagnosis of primary open-angle glaucoma or normal-tension glaucoma. GON was defined as neuroret-

inal rim narrowing at the optic disc margin with notching, excavation, or a visible RNFL defect.

For inclusion in the preperimetric glaucoma group, patients had to have a best-corrected visual acuity of 20/20 or better, a refractive spherical error between +3.00 and -6.00 diopters, a refractive cylindrical error of < 3.0 diopters, open anterior chamber angles (determined with gonioscopy), and GON and normal HVF results on reliable and reproducible SITA 30-2 test. Both preperimetric and perimetric glaucoma patients were excluded if they had any retinal pathology, neurological disease, diabetes, or a history of retinal laser or intraocular procedures. We included patients with glaucoma who had already commenced treatment with ocular hypotensive drugs.

2.1. Macula and retinal nerve fiber layer imaging

The FD-OCT measurements were performed using the RTVue-100 OCT (software version 4.0.5.39; Optovue Inc., Fremont, CA, USA), which employs a scan beam with a wavelength of 840 ± 10 nm. After pupil dilation, a well-trained operator obtained high-quality OCT images. Only scans with a signal strength index of > 45 were included in analyses. Measurements of cpRNFLT and macular parameters in each participant were obtained on the same day.

The ONH protocol was designed for measuring cpRNFLT. The total time required to acquire a single scan was 0.55 seconds. Using the OCT-generated fundus image (video baseline protocol), the ONH contours were manually traced. The cpRNFLT was then automatically measured by the instrument's software at a diameter of 3.45 mm around the center of the optic disc. A total of 775 A-scans were obtained along this circle. Subjects were excluded if peripapillary atrophy extended outside the OCT measurement circle. The cpRNFLT parameter represents the mean thickness of RNFLT measurements made around the 360° circle, and the superior hemisphere and inferior hemispheres, respectively.

The GCC scanning protocol was used to determine the GCC thickness (measured from the inner limiting membrane (ILM) to the outer inner plexiform layer (IPL) border), total retinal thickness (measured from ILM to the outer retinal pigment epithelium (RPE) border), OR thickness (measured from the outer IPL border to the outer RPE border), global loss volume (GLV), and focal loss volume (FLV) in the macula. The GCC protocol consisted of 15 vertical line scans over a 7×7-mm square region. To achieve optimum imaging coverage within the temporal region, the GCC protocol scan was centered one mm temporal to the center of the fovea. The area within a 0.75-mm radius from the center of the fovea was also excluded. During the scanning period, the GCC protocol captured 15,000 data points within 0.6 s. The GCC scan created a six-mm map corresponding to approximately 20° of HVF, and the average GCC thickness, total retinal thickness, and OR thickness were calculated over the three measurement regions (global, superior, and inferior hemisphere). GLV and FLV are two software-provided RTVue-100 OCT parameters calculated from

the GCC scan. Detailed descriptions of these analytic methods have been reported previously.[7,22] In brief, GLV measures the average amount of GCC loss over the entire GCC map and is based on the fractional deviation (FD) map. FLV measures the average focal loss over the entire GCC map and is based on both FD and pattern deviation maps. All HVF and OCT tests were conducted within a three-month period.

2.2. Ratio parameters

The G/O and G/T ratios were calculated using the following published formulas:[18]

$$\text{G/O ratio (\%)} = \left(\frac{\text{GCC thickness}}{\text{macular OR thickness}}\right) \times 100$$

$$\text{G/T ratio (\%)} = \left(\frac{\text{GCC thickness}}{\text{macular total retinal thickness}}\right) \times 100$$

The novel R/O ratio parameter was calculated using the following formula:

$$\text{R/O ratio (\%)} = \left(\frac{\text{cpRNFLT}}{\text{macular OR thickness}}\right) \times 100$$

2.3. Statistics

The demographic characteristics were compared between the groups with the $\chi 2$ test and with the Tukey-Kramer test. The RTVue-100 OCT measurements were compared between the groups using a combination of the analysis of variance and the Tukey-Kramer test. Pearson's correlation coefficients were used to characterize the relationships between the RTVue-100 OCT parameters and OR thickness and between the RTVue-100 OCT parameters and the refractive spherical equivalent. Receiver-operating characteristic (ROC) curves were used to determine whether each variable could differentiate between glaucomatous and normal eyes. The ROC curve describes the trade-off between sensitivity and specificity. An area under the ROC curve (AUROC) of 1.0 represents perfect discrimination, whereas an AUROC of 0.5 represents only chance discrimination. MedCalc (version 12.3.0, MedCalc Software, Mariakerke, Belgium) was used to draw and compare the ROC curves; all other statistical analyses were performed using SPSS statistical software (version 20.0, SPSS Inc., Chicago, IL, USA). Data are reported as the mean ± standard deviation (SD); the statistical significance was defined as $P < 0.05$.

3. Results

The normal group comprised 47 eyes of 47 healthy subjects. Thirty-one eyes of 31 patients and 70 eyes of 70 patients were included in the preperimetric and early perimetric glaucoma groups, respectively. The demographics of the participants are summarized in Table 1. There were no significant differences in sex distribution,

Table 1. Demographics and clinical characteristics of study subjects.

	Normal eyes (n = 47)	Preperimetric glaucoma (n = 31)	Early perimetric glaucoma (n = 70)	P value
Gender				0.07[a]
Male (subjects)	26	10	26	
Female (subjects)	21	21	44	
Age (years)	52.4 ± 11.1	57.4 ± 9.8	55.5 ±12.1	0.114[b]
Spherical equivalent (D)	-1.30 ± 1.91	-1.68 ± 2.23	-2.09 ± 2.45	0.177[b]
IOP (mmHg)	14.8 ± 2.7	13.4 ± 2.4	16.1 ± 3.5	< 0.001[†b]
MD in HFA (dB)	0.35 ± 1.06	0.10 ± 1.08	-2.83 ± 1.80	< 0.001[*b]
PSD in HFA (dB)	1.42 ± 0.25	1.88 ± 0.27	6.95 ± 3.10	< 0.001[*b]

Data are presented as mean ± standard deviation. [a] indicates χ^2 test; [b] indicates variance with the Tukey-Kramer test; [†] indicates preperimetric glaucoma vs. early glaucoma, $P <$ 0.001; [*] indicates normal vs. early glaucoma, $P < 0.001$, preperimetric glaucoma vs. early glaucoma, $P < 0.001$; D = diopter; IOP = intraocular pressure; MD = mean deviation; HFA= Humphrey Field Analyzer; PSD = pattern standard deviation.

age, or refraction among the groups. The early perimetric glaucoma group had a significantly higher IOP than the preperimetric glaucoma group, and significant differences in the visual field MD and pattern standard deviation were observed among the groups.

The standard RTVue-100 OCT parameter values and ratio parameter results are summarized in Tables 2 and 3, respectively. No significant difference was observed between the groups for the average OR thickness (P = 0.895). In contrast, the GCC thickness, total retinal thickness, and average cpRNFLT decreased with increasing disease severity. FLV, GLV, the G/O ratio, the G/T ratio, and the R/O ratio all significantly differed among the study groups (P < 0.001). The OR thickness correlated significantly with cpRNFLT in normal eyes (r = 0.401, P = 0.005) but not in preperimetric and early perimetric glaucoma eyes (Table 4). Significant correlations were observed between the spherical refractive equivalent and cpRNFLT (r = 0.343, P = 0.018) and between the spherical refractive equivalent and R/O ratio (r = 0.364, P = 0.012). In contrast, no correlation was observed between the spherical refractive equivalent and OR thickness (r = 0.006, P = 0.968).

Table 2. Optical coherence tomography parameters in each study group.

	Normal eyes	Preperimetric glaucoma	Early perimetric glaucoma	P value (ANOVA)
GCC thickness (μm)				
Average	94.9 ± 7.6	83.7 ± 5.4	78.8 ± 6.6	< 0.001[†]
Superior hemisphere	94.8 ± 7.9	86.6 ± 7.4	83.2 ± 9.3	< 0.001[#]
Inferior hemisphere	95.0 ± 7.7	80.7 ± 6.5	74.5 ± 10.2	< 0.001[†]
Total retinal thickness (μm)				
Average	264.7 ± 14.2	253.9 ± 8.4	248.7 ± 11.4	< 0.001[#]
Outer retinal thickness (μm)				
Average	169.8 ± 8.7	170.4 ± 5.4	169.9 ± 6.8	0.895
Superior hemisphere	171.6 ± 8.7	171.9 ± 5.4	171.1 ± 7.4	0.826
Inferior hemisphere	168.0 ± 8.9	168.9 ± 5.6	168.6 ± 6.9	0.854
FLV (%)	0.85 ± 0.94	4.41 ± 2.36	8.72 ± 3.83	< 0.001[†]
GLV (%)	6.65 ± 4.73	15.68 ± 5.09	20.29 ± 6.15	< 0.001[†]
cpRNFLT (μm)				
Average	102.0 ± 8.9	89.7 ± 8.2	84.4 ± 8.1	< 0.001[†]
Superior hemisphere	102.4 ± 10.6	91.3 ± 11.6	87.7 ± 13.3	< 0.001[#]
Inferior hemisphere	101.6 ± 9.0	88.1 ± 8.7	81.1 ± 8.4	< 0.001[†]

Data presented as mean ± standard deviation. [†] normal vs. preperimetric glaucoma group and preperimetric glaucoma vs. early glaucoma group statistically different (Tukey-Kramer test); [#] normal vs. preperimetric glaucoma group statistically different and preperimetric glaucoma group vs. early glaucoma group not statistically different (Tukey-Kramer test); ANOVA = analysis of variance; cpRNFLT = circumpapillary retinal nerve fiber layer thickness; FLV = focal loss volume; GCC = macular ganglion cell complex; GLV = global loss volume.

Table 3. Ratio parameter values in the three study groups.

	Normal eyes	Preperimetric glaucoma	Early perimetric glaucoma	P value (ANOVA)
G/O ratio (%)				
Average	55.91 ± 3.69	49.13 ± 3.15	46.41 ± 3.54	< 0.001[†]
G/T ratio (%)				
Average	35.82 ± 1.50	32.94 ± 1.46	31.66 ± 1.67	< 0.001[†]
R/O ratio (%)				
Average	60.09 ± 4.94	52.72 ± 5.58	49.78 ± 4.99	< 0.001[†]
Superior hemisphere	59.68 ± 5.79	53.22 ± 7.42	51.36 ± 7.87	< 0.001[#]
Inferior hemisphere	60.53 ± 5.27	52.33 ± 5.76	48.20 ± 5.25	< 0.001[†]

Data presented as mean ± standard deviation. [†] normal vs. preperimetric glaucoma and preperimetric glaucoma vs. early glaucoma statistically different (Tukey-Kramer test); [#] normal vs. preperimetric glaucoma statistically different and preperimetric glaucoma vs. early glaucoma not statistically different (Tukey-Kramer test); ANOVA = analysis of variance; G/O ratio = ganglion cell complex (GCC) thickness/outer retinal (OR) thickness ratio; G/T ratio = GCC thickness/total retinal thickness ratio; average R/O ratio = average circumpapillary retinal nerve fiber layer thickness (cpRNFLT)/average OR thickness ratio; superior hemisphere R/O ratio = superior hemisphere cpRNFLT /superior OR thickness; inferior hemisphere R/O ratio = inferior hemisphere cpRNFLT/inferior OR thickness.

Table 4. Correlation between macular outer retinal thickness and circumpapillary retinal nerve fiber layer thickness measurements.

	Normal eyes		Preperimetric glaucoma		Early perimetric glaucoma	
	r	*P*	r	*P*	r	*P*
Average outer retinal thickness						
Average cpRNFLT	0.401	**0.005**	-0.225	0.224	0.058	0.634
Superior outer retinal thickness						
Superior hemisphere cpRNFLT	0.363	**0.012**	-0.229	0.214	0.066	0.585
Inferior outer retinal thickness						
Inferior hemisphere cpRNFLT	0.337	**0.021**	-0.153	0.411	0.019	0.875

Values printed in bold are statistically significant ($P < 0.05$). GCC = macular ganglion cell complex; cpRNFLT = circumpapillary retinal nerve fiber layer thickness; r =Pearson correlation coefficient.

Table 5 summarizes the AUROC results for the established global RTVue-100 OCT parameters and the R/O ratio. The highest AUROC values were observed for FLV (0.941, 0.996, and 0.979 for preperimetric, early perimetric glaucoma, and all glaucoma, respectively). The G/O ratio also favorably discriminated the groups (the AUROC values for preperimetric, early perimetric glaucoma, and all glaucoma were 0.925, 0.979, and 0.962, respectively). The AUROC for FLV was significantly greater than that for cpRNFLT in both glaucoma groups. In the early perimetric glaucoma group and for all glaucoma eyes the AUROCs for the G/O ratio and G/T ratio were significantly greater than those for cpRNFLT and the R/O ratio ($P < 0.05$). At a specificity of ≥ 90%, GLV had the highest sensitivity in the preperimetric group, and FLV had the highest sensitivity in the early perimetric glaucoma group. The G/O and G/T ratios had the second highest sensitivity at a specificity of ≥ 90% in the preperimetric group. AUROCs for the hemisphere cpRNFLT and the corresponding R/O ratios are shown in Table 6.

Table 5. Area under receiver operating characteristic curves and sensitivity at a fixed specificity.

	Normal vs. preperimetric glaucoma		Normal vs. early perimetric glaucoma		Normal vs. all glaucoma	
	AUROC	Sn/Sp (Sp ≥ 90%)	AUROC	Sn/Sp (Sp ≥ 90%)	AUROC	Sn/Sp (Sp ≥ 90%)
Average GCC thickness	0.896 ± 0.04	74.19/ 91.49	0.961 ± 0.02	91.43/ 91.49	0.941 ± 0.02	86.14/ 91.49
FLV	0.941 ± 0.02[†]	74.19/ 91.49	0.996 ± 0.003[#]	98.57/ 95.74	0.979 ± 0.009[#]	91.09/ 91.49
GLV	0.907 ± 0.04	80.65/ 91.49	0.967 ± 0.02	97.14/ 91.49	0.949 ± 0.02 [†]	92.08/ 91.49
Average G/O ratio	0.925 ± 0.03	77.42/ 91.49	0.979 ± 0.01[§]	95.71/ 91.49	0.962 ± 0.01[§]	90.10/ 91.49
Average G/T ratio	0.921 ± 0.03	77.42/ 91.49	0.979 ± 0.01[§]	95.71/ 91.49	0.961 ± 0.01[§]	90.10/ 91.49
Average cpRNFLT	0.842 ± 0.05	41.94/ 91.49	0.927 ± 0.02	75.71/ 91.49	0.901 ± 0.03	65.35/ 91.49
Average R/O ratio	0.859 ± 0.05	67.74/ 91.49	0.933 ± 0.02	80.00/ 91.49	0.910 ± 0.02	76.24/ 91.49

Data presented as mean ± standard error. [†] $P < 0.05$ for average cpRNFLT comparison; [#] $P < 0.01$ for average cpRNFLT and R/O ratio comparisons; [§]$P < 0.05$ for average cpRNFLT and R/O ratio comparisons; AUROC = area under receiver operating characteristic curve; Sn = sensitivity; Sp = specificity; GCC = macular ganglion cell complex; FLV = focal loss volume; GLV = global loss volume; cpRNFLT = circumpapillary retinal nerve fiber layer thickness; G/O ratio = GCC thickness to outer retinal thickness ratio; G/T ratio = GCC thickness to total retinal thickness ratio; R/O ratio = cpRNFLT to outer retinal thickness ratio.

Table 6. Comparison of area under receiver operating characteristic curves between the corresponding sector cpRNFLT and R/O ratio parameters.

	Normal vs. preperimetric glaucoma			Normal vs. early perimetric glaucoma		
	cpRNFLT	R/O ratio	*P*	cpRNFLT	R/O ratio	*P*
Average	0.842 ± 0.05	0.859 ± 0.05	0.466	0.927 ± 0.02	0.933 ± 0.02	0.659
Superior hemisphere	0.770 ± 0.06	0.774 ± 0.06	0.838	0.806 ± 0.04	0.798 ± 0.04	0.646
Inferior hemisphere	0.865 ± 0.04	0.861 ± 0.04	0.854	0.949 ± 0.02	0.956 ± 0.02	0.417

Area under the receiver operating characteristic curve data presented as mean ± standard error. cpRNFLT = circumpapillary retinal nerve fiber layer thickness; R/O ratio = cpRNFLT to outer retinal thickness ratio.

4. Discussion

In the present study, we evaluated a potential novel RTVue-100 OCT parameters, the R/O ratio and the G/O ratio, for its diagnostic accuracy in preperimetric and early perimetric glaucoma in Japanese eyes. This investigation was conducted because the detection of early perimetric and particularly preperimetric glaucoma, with the FD-OCT instruments, has been consistently reported as suboptimal, for various populations.[22-25] In very early stages of glaucoma, the decrease of cpRNFLT, the most frequently used OCT parameter in glaucoma diagnostics, is relatively small, and therefore cpRNFLT may remain within the corresponding normal range. In order to increase the discrimination between normal eyes and eyes with early structural damage more sensitive parameters are needed. It has been shown that OCT parameter ratios have narrower normal ranges than non-ratio type parameters.[17] This is why in the current investigation R/O and G/O ratios were evaluated for their diagnostic accuracy in early and preperimetric glaucoma.

It has been shown that cpRNFLT decreases during glaucomatous ganglion cell and axon loss, while OR thickness remains uninfluenced by glaucoma.[17,18,20,21] Therefore, we hypothesized that in case a positive correlation between cpRNFLT and OR thickness is observed in normal eyes, a decrease of the normal range of R/O ratio can be expected for preperimetric and early perimetric glaucoma, and this may potentially be applicable for the detection of early glaucoma.

In fact, we observed a statistically significant moderate positive correlation between cpRNFLT and OR thickness in the healthy control group and no correlation either in the preperimetric or the early perimetric glaucoma group. Although the OR thickness did not differ between the groups, despite its wide normal range,[7-9] cpRNFLT was significantly lower in preperimetric glaucoma eyes than in normal eyes, and in the early perimetric glaucoma group than in the other groups. As expected, we observed a significantly smaller R/O ratio for the preperimetric and perimetric glaucomatous groups than the healthy control eyes. Therefore, to further evaluate the R/O ratio, we compared its diagnostic accuracy to that of the manufacturer-provided standard RTVue-100 OCT parameters and the ratio parameters that showed a favorable diagnostic accuracy in Japanese eyes in our earlier studies.[17,18]

We observed that the R/O ratio did not perform better than the best discriminating manufacturer-provided parameters (GLV and FLV) or the ratio parameters (average G/O ratio, average G/T ratio) shown by us in our previous studies.[17,18] This can be explained with our present result that refractive error has a significant effect on the R/O ratio. Previously, it has been shown that cpRNFLT, GCC thickness, FLV, and GLV are all influenced by the axial length.[26] This influence was confirmed in the present study by a significant relationship between cpRNFLT and refractive error. Our results suggest that myopia, which is highly prevalent in East Asia,[16] negatively influences the diagnostic accuracy of the previously established parameters and the R/O ratio. To compare the diagnostic accuracy of the various cpRNFLT parameters and the spatially corresponding R/O ratios, we compared the corresponding hemisphere AUROC values. Although the average R/O ratio had a higher AUROC value than the average cpRNFLT for both the preperimetric and the early perimetric glaucoma groups, this advantage was not observed when the AUROC curves of the hemisphere cpRNFLT parameters and the corresponding R/O ratio parameters were compared. Overall, though the R/O ratio performed relatively well in discriminating between healthy and preperimetric or early perimetric glaucoma, its diagnostic accuracy did not exceed that of the established RTVue-100 OCT parameters.

Previously, we reported that G/T ratio is useful for diagnosing glaucoma.[17] Furthermore, although refractive error significantly affects FLV and GLV, the G/O ratio and G/T ratio does not influence the refractive error.[26] Therefore, G/O ratio and G/T ratio provide better specificity for diagnosing glaucoma with myopia. In the current study, the AUROC for G/O ratio and G/T ratio were significantly greater than that of the cpRNFLT. This is of particular importance in preperimetric glaucoma, when functional (visual field) testing is by definition unable to support the diagnostic process. This suggests that these parameters may have a place among the software-provided parameters of the RTVue OCT, for detecting early glaucoma. FLV had a higher AUROC value than the G/O ratio and G/T ratio, though the differences were not statistically significant. Since FLV is a parameter that is specific for the RTVue-OCT, but parameters similar to RTVue-OCT GCC thickness, OR thickness and total retinal thickness can be measured with various other OCT

systems, it is possible that G/O-like and G/T-like ratios can be applied also on other FD-OCT systems. Therefore further investigations on the potential applicability and clinical usefulness of these ratio parameters on other FD-OCT instruments for diagnosing early glaucoma in Japanese eyes is proposed.

Ethnic differences are known to exist in GCC thickness; the GCC thickness is significantly thinner in African-derived populations that in other ethnic groups.[10] Previously we found no significant difference in the G/T ratio between Japanese and European eyes.[14] These data suggest that further investigations are necessary to compare the G/T ratio between all main ethnic groups, and to evaluate whether the G/T ratio has a potential to improve glaucoma diagnostics in other East-Asian populations such as Koreans and Chinese.

In conclusion, although our study was limited by the relatively small number of patients and the absence of pathological myopia cases, our results suggest that the G/O and G/T ratios can be proposed as a potential novel OCT parameters for the detection of early perimetric glaucoma in Japanese eyes.

References

1. Leung CK, Chan WM, Yung WH, Ng AC, Woo J, Tsang MK, et al. Comparison of macular and peripapillary measurements for the detection of glaucoma: an optical coherence tomography study. Ophthalmology 2005;112(3):391-400. Available from: http://www.diseaseinfosearch.org/result/3065 PubMed PMID: 15745764. doi: 10.1016/j.ophtha.2004.10.020

2. Medeiros FA, Zangwill LM, Bowd C, Vessani RM, Susanna Jr R, Weinreb RN. Evaluation of retinal nerve fiber layer, optic nerve head, and macular thickness measurements for glaucoma detection using optical coherence tomography. Am J Ophthalmol 2005;139(1):44-55. Available from: http://www.scholaruniverse.com/ncbi-linkout?id=15652827 PubMed PMID: 15652827. doi: 10.1016/j.ajo.2004.08.069.

3. Leite MT, Rao HL, Zangwill LM, Weinreb RN, Medeiros FA. Comparison of the diagnostic accuracies of the Spectralis, Cirrus, and RTVue optical coherence tomography devices in glaucoma. Ophthalmology 2011 Mar;118(7):1334-1339. Available from: http://europepmc.org/abstract/MED/21377735 PubMed PMID: 21377735. doi: 10.1016/j.ophtha.2010.11.029.

4. Wollstein G, Ishikawa H, Wang J, Beaton SA, Schuman JS. Comparison of three optical coherence tomography scanning areas for detection of glaucomatous damage. Am J Ophthalmol 2005;139(1):39-43. Available from: http://www.scholaruniverse.com/ncbi-linkout?id=15652826 PubMed PMID: 15652826. doi: 10.1016/j.ajo.2004.08.036.

5. Kim NR, Lee ES, Seong GJ, Choi EH, Hong S, Kim CY. Spectral-domain optical coherence tomography for detection of localized retinal nerve fiber layer defects in patients with open-angle glaucoma. Arch Ophthalmol 2010;128(9):1121-1128. Available from: http://www.scholaruniverse.com/ncbi-linkout?id=20837794 PubMed PMID: 20837794. doi: 10.1001/archophthalmol.2010.204.

6. Takagi ST, Kita Y, Yagi F, Tomita G. Macular retinal ganglion cell complex damage in the apparently normal visual field of glaucomatous eyes with hemifield defects. J Glaucoma 2012;21(5):318-325. Available from: https://www.researchgate.net/publication/e/pm/21423034?ln_t=p&ln_o=linkout PubMed PMID: 21423034. doi: 10.1097/IJG.0b013e31820d7e9d.

7. Tan O, Chopra V, Lu AT, Schuman JS, Ishikawa H, Wollstein G, et al. Detection of macular ganglion cell loss in glaucoma by Fourier-domain optical coherence tomography. Ophthalmology 2009;116(12):2305-2314. Available from: http://europepmc.org/abstract/MED/19744726 PubMed PMID: 19744726. doi: 10.1016/j.ophtha.2009.05.025.

8. Öner V, Aykut V, Taş M, Alakus MF, Iscan Y. Effect of refractive status on peripapillary retinal nerve fibre layer thickness: a study by RTVue spectral domain optical coherence tomography. Br J Ophthalmol 2013;97(1):75-79. Available from: http://bjo.bmj.com/cgi/doi/10.1136/bjophthalmol-2012-301865 PubMed PMID: 23143906. doi: 10.1136/bjophthalmol-2012-301865.

9. Zhao Z, Jiang C. Effect of myopia on ganglion cell complex and peripapillary retinal nerve fiber layer measurements. a Fourier domain optical coherence tomography study of young Chinese persons. Clin Experiment Ophthalmol 2013;41(6):561-566. Available from: http://doi.wiley.com/10.1111/ceo.12045 PubMed PMID: 23231592. doi: 10.1111/ceo.12045.

10. Girkin CA, McGwin Jr G, Sinai MJ, Sekhar GC, Fingeret M, Wollstein G, et al. Variation in optic nerve and macular structure with age and race with spectral-domain optical coherence tomography. Ophthalmology 2011;118(12):2403-2408. Available from: https://www.nlm.nih.gov/medlineplus/seniorshealth.html PubMed PMID: doi: 10.1016/j.ophtha.2011.06.013.

11. Savini G, Barboni P, Parisi V, Carbonelli M. The influence of axial length on retinal nerve fiber layer thickness and optic-disc size measurements by spectral-domain OCT. Br J Ophthalmol 2012;96(1):57-61. Available from: https://www.researchgate.net/publication/e/pm/21349942?ln_t=p&ln_o=linkout PubMed PMID: 21349942. doi: 10.1136/bjo.2010.196782.

12. Cheung CY, Leung CK, Lin D, Pang CP, Lam DS. Relationship between retinal nerve fiber layer measurement and signal strength in optical coherence tomography. Ophthalmology 2008;115(8):1347-1351. Available from: https://www.researchgate.net/publication/e/

pm/18294689?ln_t=p&ln_o=linkout PubMed PMID: 18294689. doi: 10.1016/j.ophtha.2007.11.027.

13. Alasil T, Wang K, Keane PA, Lee H, Baniasadi N, de Boer JF, et al. Analysis of normal retinal nerve fiber layer thickness by age, sex, and race using spectral domain optical coherence tomography. J Glaucoma 2013;22(7):532-541. Available from: https://www.nlm.nih.gov/medlineplus/senior-shealth.html PubMed PMID: 22549477. doi: 10.1097/IJG.0b013e318255bb4a.

14. Kita Y, Naghizadeh F, Kita R, Tomita G, Holló G. Comparison of macular ganglion cell complex thickness to total retinal thickness ratio between Hungarian and Japanese eyes. Jpn J Ophthalmol 2013 Aug;57(6):540-545. Available from: https://www.researchgate.net/publication/e/pm/23982214?ln_t=p&ln_o=linkout PubMed PMID: 23982214. doi: 10.1007/s10384-013-0273-5.

15. Holló G, Naghizadeh F, Vargha P. Accuracy of macular ganglion-cell complex thickness to total retina thickness ratio to detect glaucoma in white Europeans. J Glaucoma;23(8):23-7. Available from: http://www.diseaseinfosearch.org/result/3065 PubMed PMID: 24247997. doi: 10.1097/IJG.0000000000000030.

16. Shimizu N, Nomura H, Ando F, Niino N, Miyake Y, Shimokata H. Refractive errors and factors associated with myopia in an adult Japanese population. Jpn J Ophthalmol 2003;47(1):6-12. Available from: http://linkinghub.elsevier.com/retrieve/pii/S0021515502006202 doi: 10.1016/S0021-5155(02)00620-2.

17. Kita Y, Kita R, Takeyama A, Takagi S, Nishimura C, Tomita G. Ability of optical coherence tomography-determined ganglion cell complex thickness to total retinal thickness ratio to diagnose glaucoma. J Glaucoma 2013;22(9):757-762. Available from: http://www.diseaseinfosearch.org/result/3065 PubMed PMID: 22668980. doi: 10.1097/IJG.0b013e31825af58a.

18. Kita Y, Kita R, Takeyama A, Anraku A, Tomita G, Goldberg I. Relationship between macular ganglion cell complex thickness and macular outer retinal thickness: a spectral-domain optical coherence tomography study. Clin Experiment Ophthalmol 2013 Apr;41(7):674-682. Available from: https://www.researchgate.net/publication/e/pm/23433351?ln_t=p&ln_o=linkout PubMed PMID: 23433351. doi: 10.1111/ceo.12089.

19. Takeyama A, Kita Y, Kita R, Tomita G. Influence of axial length on ganglion cell complex (GCC) thickness and on GCC thickness to retinal thickness ratios in young adults. Jpn J Ophthalmol 2014;58(1):86-93. Available from: https://www.researchgate.net/publication/e/pm/24242185?ln_t=p&ln_o=linkout PubMed PMID: 24242185. doi: 10.1007/s10384-013-0292-2.

20. Tan O, Li G, Lu AT, Varma R, Huang D, Group, I.f.G.S. (Advanced) . Mapping of macular substructures with optical coherence tomography for glaucoma diagnosis. Ophthalmology 2008;115(6):949-956. Available from: http://europepmc.org/abstract/MED/17981334 PubMed PMID: 17981334. doi: 10.1016/j.ophtha.2007.08.011.

21. Vajaranant TS, Anderson RJ, Zelkha R, Zhang C, Wilensky JT, Edward DP, et al. The relationship between macular cell layer thickness and visual function in different stages of glaucoma. Eye 2011 Feb;25(5):612-618. Available from: http://europepmc.org/abstract/MED/21350568 PubMed PMID: 21350568. doi: 10.1038/eye.2011.17.

22. Seong M, Sung KR, Choi EH, Kang SY, Cho JW, Um TW, et al. Macular and peripapillary retinal nerve fiber layer measurements by spectral domain optical coherence tomography in normal-tension glaucoma. Invest Ophthalmol Vis Sci 2009 Oct;51(3):1446-1452. Available from: http://ClinicalTrials.gov/search/term=19834029%20%5BPUBMED-IDS%5D PubMed PMID: 19834029. doi: 10.1167/iovs.09-4258.

23. Hirashima T, Hangai M, Nukada M, Nakano N, Morooka S, Akagi T, et al. Frequency-doubling technology and retinal measurements with spectral-domain optical coherence tomography in preperimetric glaucoma. Graefes Arch Clin Exp Ophthalmol 2012 Jun;251(1):129-137. Available from: http://www.diseaseinfosearch.org/result/3065 PubMed PMID: 22684903. doi: 10.1007/s00417-012-2076-7.

24. Mori S, Hangai M, Sakamoto A, Yoshimura N. Spectral-domain optical coherence tomography measurement of macular volume for diagnosing glaucoma. J Glaucoma 2010;19(8):528-534. Available from: http://ClinicalTrials.gov/search/term=20164794%20%5BPUBMED-IDS%5D PubMed PMID: 20164794. doi: 10.1097/IJG.0b013e3181ca7acf.

25. Na JH, Lee K, Lee JR, Baek S, Yoo SJ, Kook MS. Detection of macular ganglion cell loss in preperimet-
     ric glaucoma patients with localized retinal nerve fibre defects by spectral-domain optical coherence
     tomography. Clin Experiment Ophthalmol 2013 Jul;41(9):870-880. Available from: http://www.disea-
     seinfosearch.org/result/3065 PubMed PMID: 23777476. doi: 10.1111/ceo.12142.
26. Kita Y, Kita R, Takeyama A, Tomita G, Goldberg I. The effect of high myopia on glaucoma diag-
     nostic parameters as measured by optical coherence tomography. Clin Experiment Ophthalmol
     2014;42(8):722-728. Available from: http://www.diseaseinfosearch.org/result/3065 PubMed PMID:
     24617978. doi: 10.1111/ceo.12318.

Intracranial, intraocular and ocular perfusion pressures: differences between morning and afternoon measurements

Lina Siaudvytyte[1], Akvile Daveckaite[1], Ingrida Januleviciene[1], Arminas Ragauskas[2], Brent Siesky[3], Alon Harris[3]

[1]Eye Clinic, Lithuanian University of Health Sciences, Kaunas, Lithuania; [2]Health Telematics Science Centre of Kaunas University of Technology, Kaunas, Lithuania; [3]Glaucoma Research and Diagnostic Center, Eugene and Marilyn Glick Eye Institute, Indiana University School of Medicine, Indianapolis, IN, USA

Abstract

Purpose: To assess how intracranial pressure (ICP), intraocular pressure (IOP) and ocular perfusion pressure (OPP) differ between the morning and the afternoon in healthy subjects.
Design: Prospective pilot study.
Methods: Ten healthy subjects age 26.5 (1.2) years were included in the prospective pilot study. For each participant, blood pressure, heart rate, IOP, ICP and calculated OPP, translaminar pressure difference (TPD) were assessed two times per day, in the morning (9 ± 1 a.m.) and afternoon (2 ± 1 p.m.) by the same experienced operator. Best-corrected visual acuity and body mass index were also evaluated. TPD was calculated as IOP minus ICP. ICP was measured using a non-invasive two-depth transcranial Doppler device. $P < 0.05$ was considered significant.
Results: Mean ICP was higher during afternoon (10.09 (1.8) mmHg) compared to morning ICP (9.80 (2.2) mmHg), but the difference was not statistically significant (p = 0.14). By analyzing ICP according to different refractive errors categories, we found that emmetropic patients had higher ICP (morning 11.94 (3.0), afternoon 11.5 (2.6) mmHg), compared to myopic (accordingly, 9.14 (1.2) and 9.72 (1.3) mmHg) or hypermetropic (accordingly, 8.85 (0.7) and 9.17 (0.8) mmHg) patients, but the difference

Correspondence: Lina Siaudvytyte, Eye Clinic, Lithuanian University of Health Sciences, Eiveniu str. 2, Kaunas 50009, Lithuania.
E-mail: lynciuke@gmail.com

was not statistically significant (p > 0.05). We also found that higher OPP in the morning was correlated to lower TPD (r = -0.65; p = 0.04).

Conclusion: We found no significant variations in ICP, IOP or OPP during morning and afternoon in young healthy subjects. Higher OPP was related to lower TPD in the morning. Further prospective studies are warranted to investigate diurnal ICP variations in glaucoma patients to understand if fluctuations in ICP and TPD may contribute to the disease process.

Key words: Intracranial pressure, intraocular pressure, diurnal variations, healthy subjects, ocular perfusion pressure, translaminar pressure difference

1. Introduction

Intracranial pressure (ICP) is the pressure inside the skull, corresponding brain tissue, and cerebrospinal fluid (CSF). The human body has various mechanisms by which it keeps ICP within certain limits through shifts in production and absorption of CSF.[1] ICP and intraocular pressure (IOP) are interrelated and relatively independent pressure systems, which facilitate a relatively stable state through aqueous and CSF circulations. These two circulating fluids are both produced by carbonic anhydrase-catalyzed reactions, generally represent an ultrafiltrate of blood, and have nearly identical chemical composition, except that CSF has more proteins and less ascorbates.[2-3] Normal ICP varies with age but is generally considered to be 5-15 mmHg in healthy supine adults, 3-7 mmHg in children, and 1.5-6 mmHg in infants.[4-6] The mean IOP in healthy adults is 15-16 mmHg, with a standard deviation of nearly 3 mmHg. The upper limit of normal IOP is statistically defined as two standard deviations above normality.[7-8] Low ICP has recently been implicated in the pathogenesis of glaucoma,[9-14] as optic nerve is exposed not only to IOP in the eye, but also to ICP as it is surrounded by CSF in the subarachnoid space (SAS). Furthermore, CSF pressure represents the true counter-pressure against the IOP across the lamina cribrosa and is one of the two determinants of the translaminar pressure difference (TPD). Studies have shown that higher TPD may lead to abnormal function and damage of the optic nerve due to changes in axonal transportation, deformation of the lamina cribrosa, altered blood flow, or a combination thereof leading to glaucomatous damage.[15-16] However, measuring TPD in glaucoma and healthy subjects has not been historically feasible due to the invasiveness of traditional ICP measurements and the potential risk of intracranial hemorrhages, infection, persistent leak of CSF and/or cerebral herniation.[17] Many different technologies have been explored to overcome the invasive limitation of ICP measurements,[18-20] but all these approaches are based solely on correlation of various anatomical or physiological parameters of the human head and brain with ICP. Therefore, previous attempts to non-invasively measure ICP have not provided absolute ICP values in mmHg greatly

limiting specificity of their measures.

In an attempt to overcome these previous methodological limitations, an innovative method for non-invasive measurement of ICP absolute values was recently developed using transcranial Doppler ultrasound. This methodology measures and compares blood flow pulsatilities in the intracranial and extracranial segments of the ophthalmic artery (OA). The sensitivity, specifity and diagnostic value of this device has been proven in previous prospective studies with healthy subjects and patients with neurological diseases.[21-22] In order to provide insight on these emerging dynamic glaucomatous risk factors, we conducted a pilot study with the aim to assess diurnal variations of ICP, IOP, and ocular perfusion pressure (OPP) in healthy subjects to establish a baseline understanding of their diurnal activity in disease free stasis.

2. Materials and methods

Ten healthy subjects (age 26.5 (1.2)) participated in a prospective pilot clinical study. All study procedures were carried out according to the Declaration of Helsinki, and the study protocol was approved by the Lithuanian University of Health Sciences Review Board. Study objectives and methods were explained to all subjects prior to examination. All participants provided written informed consent. All examinations were performed on one randomly chosen study eye.

Quantities of blood pressure (BP), heart rate, IOP and ICP were measured two times per day, in the morning (9 ± 1 a.m.) and afternoon (2 ± 1 p.m.) by the same experienced operator (L.S.), which allowed us to estimate quantities of OPP and TPD. TPD was calculated as IOP minus ICP. OPP was calculated using the equation OPP = 2/3MAP – IOP, where MAP is mean arterial pressure. Systolic ocular perfusion pressure (SOPP) was determined by subtracting IOP from systolic BP. Diastolic ocular perfusion pressure (DOPP) was determined by subtracting IOP from diastolic BP. An average of two separate measurements with a 15 minutes undisturbed rest period constituted the mean value of parameters. Best-corrected visual acuity and body mass index (BMI) were also evaluated.

Non-invasive absolute ICP values were measured using a two-depth Transcranial Doppler (TCD) device (Vittamed UAB, Kaunas, Lithuania) that does not require individual patient specific calibration. A head frame with fixed ultrasound transducer was placed over the closed eyelid. A small inflatable ring cuff placed over the tissues surrounding the eyeball produced external pressure on the orbit. The TCD transducer and the external pressure device were connected to a computer with specific software allowing it to assess simultaneous an insonation angle independent blood flow pulsation monitoring in the intracranial and extracranial segments of the OA (Fig. 1). External pressure was automatically increased gradually from 0 to 20 mmHg by pressure steps of 4 mmHg. In order to decrease ICP value
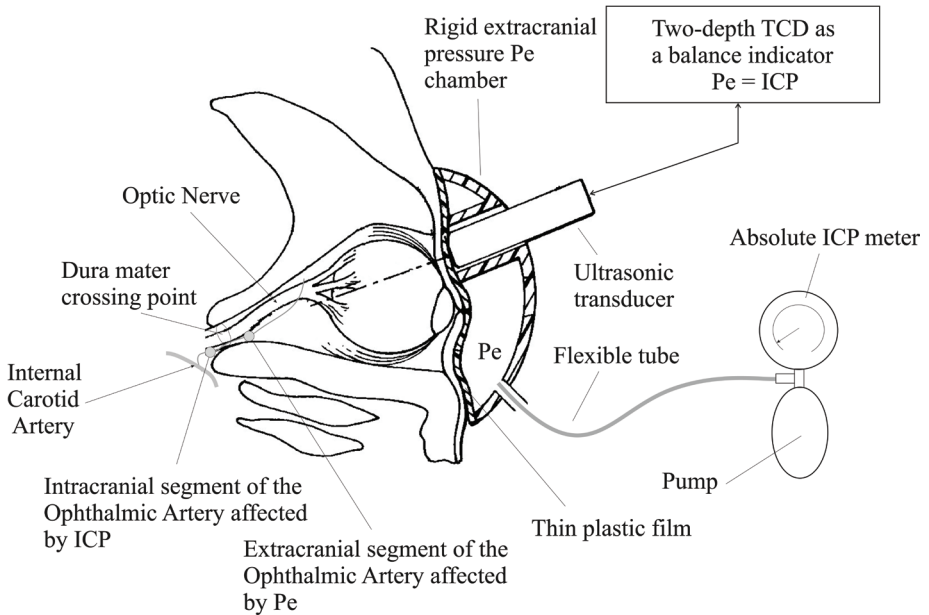
Fig. 1. Non-invasive two-depth TCD device components showing the relevant eye/brain anatomy. The ultrasound transducer of the Doppler subsystem is surrounded by an externally applied pressure chamber with a controlled external pressure (Pe) source and measurement. (Reprinted with permission from Ragauskas *et al.* 2012.)

sampling error, if the first measured absolute ICP value was lower than 10 mmHg, then the measurement was repeated using 2 mmHg pressure steps until external pressure reached 12 mmHg. The value of external pressure, when blood flow signals in both OA segments are equal, was fixed and expressed automatically in absolute units of mmHg. The duration of one ICP measurement was up to 10 minutes.

Non-invasive ICP was measured in the supine position, and therefore IOP was measured in the same position using a Schiotz impression tonometer.

Inclusion criteria consisted of healthy subjects over 18 years of age with no history of glaucoma or other diseases that could disturb the results and willingness to sign informed consent form prior to initiation of the study. Pregnant or nursing women, patients with uncontrolled systemic diseases, patients with a history of allergy to local anesthetics, orbital/ocular trauma, neurological or other diseases that could bias study results were excluded from the study.

The statistical data analysis was performed using computer program SPSS 17.0 for Windows. All variables were defined by methods of descriptive statistics. The analysis of the quantitative variables included calculation of the mean and standard deviation (x (SD)). The Wilcoxon signed-rank test was used when comparing two related samples on a single sample to assess whether their population mean ranks

differ. The hypothesis of equality of means among three groups was analyzed using the Kruskall-Wallis test. Association between categorical variables or abnormally distributed continuous variables was assessed by Spearman's correlation. The level of significance $p < 0.05$ was considered significant.

3. Results

Ten healthy subjects (80% women, 20% men) were included in the prospective pilot study. Patients characteristics are provided in Table 1.

Morning and afternoon parameters are shown in Table 2. There were no statistically significant differences between morning and afternoon IOP, TPD, BP and OPP ($p > 0.05$). ICP was higher during afternoon (10.09 (1.8) mmHg), compared to morning ICP (9.80 (2.2) mmHg), but the difference was not statistically significant ($p = 0.14$) (Fig. 2). By analyzing ICP according to different refractive errors between subjects (Table 3), we found that emmetropic patients had higher ICP compared to myopic or hypermetropic patients, but the difference was not statistically significant ($p > 0.05$). We also found that in the morning higher OPP was correlated to lower TPD ($r = -0.65$; $p = 0.04$).
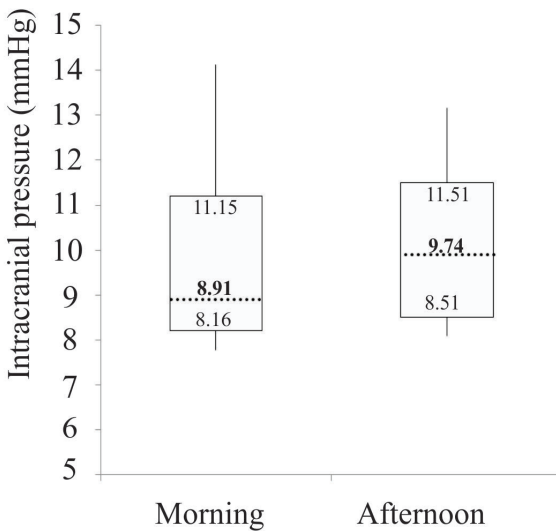

Fig. 2. Morning and afternoon intracranial pressure variations. Box-plot showing distribution of intracranial pressure during morning and afternoon in healthy subjects. Box-plots show the median, interquartile range, minimum and maximum values.

Table 1. Patient characteristics.

	Healthy subjects (N = 10) Mean (SD)
Sex (N (%)): Male Female	2 (20%) 8 (80%)
Age (years): Range	26.5 (1.2) 25-29
Best corrected visual acuity Height (m) Weight (kg)	1.0 (0.0) 1,71 (0.1) 63.6 (16.6)
Body mass index (kg/m²)	21.4 (3.1)
Systemic medications	0

SD = standard deviation; N = number.

Table 2. Changes in parameters during morning and afternoon.

	Morning (9 ± 1 a.m.)		Afternoon (2 ± 1 p.m.)		p value
	Mean (SD)	Median	Mean (SD)	Median	
ICP (mmHg)	9.80 (2.2)	8.91	10.09 (1.8)	9.74	0.14
Range:	7.77-14.13		8.08-13.16		
IOP (mmHg)	13.4 (2.0)	13.1	13.6 (1.8)	13.1	0.58
TPD (mmHg)	3.64 (2.0)	3.71	3.49 (1.8)	3.28	0.95
Systolic BP (mmHg)	115.1 (7.3)	114.0	115.9 (7.1)	114.0	0.28
Diatolic BP (mmHg)	77.3 (7.9)	76.5	75.7 (6.5)	75.0	0.44
OPP (mmHg)	50.1 (4.7)	50.8	50.3 (3.7)	49.5	0.61
SOPP (mmHg)	101.7 (7.3)	101.6	102.3 (6.8)	100.9	0.47
DOPP (mmHg)	63.9 (7.4)	63.6	62.1 (5.6)	60.4	0.44
Heart rate (bpm)	64.4 (4.8)	62.5	64.5 (4.5)	62.5	0.86

*Wilcoxon signed-rank test. Significance level $p < 0.05$. SD = standard deviation; ICP = intracranial pressure; IOP = intraocular pressure; TPD = translaminar pressure difference; BP = blood pressure; OPP = ocular perfusion pressure; SOPP = systolic ocular perfusion pressure; DOPP = diastolic ocular perfusion pressure.

Table 3. Differences in intracranial pressure between different refractive errors.

	Emmetropia (n = 3) Mean (SD)	Myopia (n = 4) Mean (SD)	Hypermetropia (n = 3) Mean (SD)	p value
Morning ICP (9 ± 1 a.m.) (mmHg)	11.94 (3.0)	9.14 (1.2)	8.53 (0.7)	0.23
Afternoon ICP (2 ± 1 p.m.) (mmHg)	11.50 (2.6)	9.72 (1.3)	9.17 (0.8)	0.40
p value	0.59	0.14	0.11	

* Wilcoxon signed-rank test. ** Kruskal Wallis test. Significance level $p < 0.05$. N = number; SD = standard deviation; ICP = intracranial pressure.

4. Discussion

There is a growing body of evidence that indicates ICP and TPD may be involved in the disease process of glaucomatous optic neuropathy. These physiological variables, along with BP and IOP, likely fluctuate during the diurnal cycle, allowing for possible periods of susceptibility and tissue damage. While it is accepted that diurnal IOP fluctuations are greater in eyes with glaucoma,[23] it is currently not established whether that is also true of ICP variations. Several studies concluded that IOP fluctuations were more strongly related to progression of visual field damage than the level of mean IOP.[24-25] Mechanistically this may occur due to previous findings of repeated mechanical stress on neurons being more harmful than steady stress.[26-28]

In this study we reported morning and afternoon ICP measurements in healthy subjects. We found that during first part of the day ICP changed marginally, though ICP was higher at afternoon. Several experimental studies analyzed circadian variations in conscious and partially restrained Sprague-Dawley rats and found nocturnal elevation in ICP[29-30] by 3.9 mmHg.[31] Another study with conscious, freely moving Sprague-Dawley rats showed a relatively constant ICP in the light and dark periods.[32] Although circadian ICP variations were insignificant, endogenous variations in the ICP regulatory factors might be significant. It has been revealed that human CSF production exhibits a circadian pattern – CSF production is two to three-and-a-half times higher in the middle of the night compared to late afternoon.[33-34] However, since healthy subjects have ICP homeostasis, the significant change in CSF production might not lead to a parallel day/night ICP pattern.[35] Furthermore, Kropyvnytskyy *et al.* in their study with severely neurologically affected patients found no detectable 24-hour ICP rhythm in head injury patients.[36]

Given that humans sleep in the supine or prone position but are upright during the day, it is important to note that IOP and ICP are dynamic parameters and vary

according to changes in body position or individual activities.[37] Therefore we assessed these parameters in the standard ICP measuring state – a supine position.[38] Understanding posture and its affects on these dynamic variables is important as prospective studies have found that in healthy subjects CSF pressure was related to the systemic arterial BP and IOP.[41] According to several population-based studies, IOP was also related to the systemic arterial BP so that pressures in all three fluid-filled compartments were related to each other,[42-43] however, the mechanism of such a triangular relationship remains unclear. Samuels *et al.* in an experimental study with rats found that chemical stimulation of the dorsomedial and perifornical hypothalamic neurons evoked substantial increases in IOP, CSF pressure, TPD, heart rate and MAP.[44] In our study we did not find any correlations between ICP, IOP or BP, however, we found a negative correlation between OPP and TPD in the morning. It is important to consider that in this correlation some signs of triangulation can be found, as these parameters are calculated by the following formulas: TPD = IOP – ICP; OPP = 2/3MAP – IOP. There are many variations in all body fluid spaces, cardiac output, peripheral resistance and blood flow to various vascular beds,[45-46] however, all these variations are insignificant to young healthy adults as they have intact homeostasis and ability of a vascular bed to maintain its blood flow despite changes in perfusion pressure. In our study we did not find significant variations from morning to afternoon in IOP, BP, OPP or TPD in healthy individuals. Unlike our participant population, glaucoma patients have been demonstrated to have pathological variations in IOP, BP, OPP[23,47-48] that could result in higher TPD. Higher IOP or lower ICP also result in higher TPD, leading to barotraumatic damage to the optic nerve. In other words, there is a likelihood of misbalance between IOP, ICP and BP in glaucoma patients contributing to their disease process.

In our study we analyzed young healthy adults and found that mean ICP was about 10 mmHg. Several studies that have examined CSF pressure and age failed to find a relationship of significance,[49-50] while Fleischman *et al.* in their retrospective analysis of 33,922 patients who had lumbar puncture revealed that CSF pressure decreases with older age. This study found that CSF pressure was stable for the first 50 years of life (11.5 (2.8) mmHg) after which there was a steady decline by 2.5% at age 50-54 and by 26.9% at age 90-95. However, CSF pressure of the included patients varied from 4.41 to 18.38 mmHg.[51] Other authors analyzing primary open-angle glaucoma (POAG) and healthy subjects found inconsistent ICP values: Ren *et al.* in a prospective study analyzed 71 healthy subjects with a mean age of 45.7 and found mean a ICP of 12.9 mmHg.[41] Similar ICP results were found by Berdahl *et al.* in a retrospective study, however, the mean age of included healthy subjects was 68.2.[52] These studies measured ICP invasively via lumbar puncture (41,52). Siaudvytyte *et al.* evaluated ICP non-invasively and found it to be 10.5 mmHg in 51.9-years-old healthy subjects.[14]

Positive BMI and CSF pressure associations were found by various prospective and retrospective studies.[52-54] Fleischman *et al.* analyzed CSF pressure in five

different age groups and found that BMI was positively correlated with CSF pressure in every age group. Adult patients younger than 42 years of age with BMI between 10.1 to 22.3 kg/m^2 had a mean CSF pressure of 9.92 mmHg.[51] This data corresponds to ours as our results showed a mean ICP of about 10 mmHg with BMI of 21.4(3.1) kg/m^2.

We also found no statistically significant differences in ICP between subjects with different refractive errors. Our included subjects had mild myopia/hypermetropia, therefore higher refractive errors influence on ICP still remains unclear.

There are several limitations in our study. Firstly, it was a small sample pilot study aiming to evaluate physiological fluctuations of IOP, ICP and OPP in healthy young adults with presumably intact autoregulation that likely does not reflect glaucoma populations. Therefore this study establishes a baseline of fluctuations in healthy subjects for comparative purposes and our data should not be considered representative of any disease state. However, it represents an exciting future direction for our pilot analysis to build upon. A larger sample may also allow future analysis to confirm other relationships of IOP, ICP and OPP variations. Secondly, we obtained only morning and midday measurements of these parameters, and therefore it does not present diurnal or circadians variations. Thirdly, due to the requirement of measuring ICP in the supine position and the fact that IOP varies according to posture we measured IOP with Schiotz tonometer, which may not be the same as the current gold standard Goldmann tonometer, besides it has errors related to sclera rigidity and corneal curvature.[55] Fourthly, we used a non-invasive ICP measurement method by using two-depth TCD device, instead of golden standard invasive ICP measurement methods, which may represent sample errors yet to be discovered. Nevertheless, a prospective study with 108 neurological patients showed that diagnostic sensitivity, specificity and the area under the ROC curve of this non-invasive absolute ICP method were 68.0 %, 84.3 % and 0.87, respectively.[56] However, it remains unclear whether ICP is directly related to the CSF pressure in the orbit around the optic nerve. Experimental studies on dogs showed that CSF pressure in optic nerve SAS is equal to CSF pressure in the lateral ventricle of the brain at the level of eye.[15] Of note, the method depends on the optic nerve path at SAS between the orbital and intracranial parts. It is not known what happens when the optic nerve canal is blocked, in such cases as suprasellar meningioma, tuberculous meningitis, intracanalicular OA aneurysm, etc. It is thought that CSF is distributed evenly with a continuous flow through all CSF spaces, including ventricles, cisterns and SAS. The SAS of the optic nerve is bridged by a variety of trabeculae and septa, which number and morphology depend on their location within SAS: the retrobulbar portion of the optic nerve is composed of delicate trabeculae, the midorbital SAS – of broad septae, the canalicular portion – combination of septae and trabeculae.[57] In addition, unlike in other areas, the dura of optic nerve sheath contains atypical meningeal tissue with lymphoid characteristics.[58] Interestingly, Killer and colleagues[59] found that CSF flow between the basal cisterns and the SAS surrounding the optic nerve was

different between patients with NTG and healthy subjects, showing that NTG had decreased CSF flow in this area.

5. Conclusion

We found no significant ICP, IOP and OPP variations during morning and afternoon in young healthy subjects. Higher OPP was related to lower TPD in the morning. Further prospective studies are warranted to investigate diurnal ICP variations in glaucoma patients to understand how fluctuations in ICP and TPD may contribute to the glaucoma process.

Acknowledgements

References

1. Rodriguez-Boto G, Rivero-Garvia M, Gutierrez-Gonzalez R, Marquez-Rivas J. Basic concepts about brain pathophysiology and intracranial pressure monitoring. Neurologia 2015;30(1):16-22. Available from: http://www.elsevier.es/en/linksolver/ft/pii/S0213-4853(12)00269-1 PubMed PMID: 23246212. doi: 10.1016/j.nrl.2012.09.002.
2. Goel M, Picciani RG, Lee RK, Bhattacharya SK. Humor Dynamics: A Review. The Open Ophthalmology Journal 2010;4:52-9. Available from: http://europepmc.org/abstract/MED/21293732 PubMed PMID: 21293732. doi: 10.2174/1874364101004010052.
3. Samuels MA. Disturbances of cerebrospinal fluid and its circulation, including hydrocephalus, pseudo-tumor cerebri, and low-pressure syndromes. and Victor's principles of neurology. Chapter 30, 9th ed. NY: McGraw-Hill; 2009.
4. Albeck MJ, Børgesen SE, Gjerris F, Schmidt JF, Sørensen PS. Intracranial pressure and cerebrospinal fluid outflow conductance in healthy subjects. J Neurosurg 1991;74(4):597-600. Available from: https://www.researchgate.net/publication/e/pm/2002373?ln_t=p&ln_o=linkout PubMed PMID: 2002373. doi: 10.3171/jns.1991.74.4.0597.
5. Smith M. Monitoring intracranial pressure in traumatic brain injury. Anesth Analg 2008;106(1):240-248. Available from: https://www.nlm.nih.gov/medlineplus/traumaticbraininjury.html PubMed PMID: 18165584. doi: 10.1213/01.ane.0000297296.52006.8e.
6. Welch K. The intracranial pressure in infants. J Neurosurg 1980;52(5):693-699. Available from: http://thejns.org/doi/abs/10.3171/jns.1980.52.5.0693 PubMed PMID: 7373397. doi: 10.3171/jns.1980.52.5.0693.
7. Leydecker WA, Neumann HG. The intraocular pressure of healthy eyes. Klin Mbl Augenheilk 1958;133:662-70.
8. Society EG. Intraocular pressure (IOP) and tonometry. In: Publicomm srl (eds). Terminology and guide-lines for glaucoma. Chapter 2014;1.

9. Yablonski M, Ritch R, Pokorny KS. Effect of decreased intracranial pressure on optic disc. Invest Ophthalmol Vis Sci 1979;18:165.

10. Berdahl JP, Allingham RR, Johnson DH. Cerebrospinal fluid pressure is decreased in primary open-angle glaucoma. Ophthalmology 2008;115(5):763-768. Available from: http://www.diseaseinfosearch.org/result/3065 PubMed PMID: 18452762. doi: 10.1016/j.ophtha.2008.01.013.

11. Ren R, Wang N, Zhang X, Cui T, Jonas JB. Trans-lamina cribrosa pressure difference correlated with neuroretinal rim area in glaucoma. Graefes Arch Clin Exp Ophthalmol 2011 Apr;249(7):1057-1063. Available from: http://www.diseaseinfosearch.org/result/3065 PubMed PMID: 21455776. doi: 10.1007/s00417-011-1657-1.

12. Jonas JB. Role of cerebrospinal fluid pressure in the pathogenesis of glaucoma. Acta Ophthalmol 2011;89(6):505-514. Available from: http://dx.doi.org/10.1111/j.1755-3768.2010.01915.x PubMed PMID: 20456257. doi: 10.1111/j.1755-3768.2010.01915.x.

13. Volkov VV. [Essential element of the glaucomatous process neglected in clinical practice]. Oftalmol Zh 1976;31(7):500-504. Available from: https://www.nlm.nih.gov/medlineplus/glaucoma.html PubMed PMID: 1012622.

14. Siaudvytyte L, Januleviciene I, Ragauskas A, Bartusis L, Meiliuniene I, Siesky B, et al. The difference in translaminar pressure gradient and neuroretinal rim area in glaucoma and healthy subjects. J Ophthalmol 2014 Apr;2014:937360. Available from: http://dx.doi.org/10.1155/2014/937360 PubMed PMID: 24876948. doi: 10.1155/2014/937360.

15. Morgan WH, Yu DY, Cooper RL, Alder VA, Cringle SJ, Constable IJ. The influence of cerebrospinal fluid pressure on the lamina cribrosa tissue pressure gradient. Invest Ophthalmol Vis Sci 1995;36(6):1163-1172. Available from: https://assays.cancer.gov/CPTAC-232 PubMed PMID: 7730025.

16. Morgan WH, Chauhan BC, Yu D, Cringle SJ, Alder VA, House PH. Optic disc movement with variations in intraocular and cerebrospinal fluid pressure. Invest Ophthalmol Vis Sci 2002;43(10):3236-3242. Available from: https://www.researchgate.net/publication/e/pm/12356830?ln_t=p&ln_o=linkout PubMed PMID: 12356830.

17. Zeng T, Gao L. Management of patients with severe traumatic brain injury guided by intraventricular intracranial pressure monitoring: a report of 136 cases. Chin J Traumatol 2010 Jun;13(3):146-151. Available from: https://www.nlm.nih.gov/medlineplus/traumaticbraininjury.html PubMed PMID: 20515591.

18. Rosenberg JB, Shiloh AL, Savel RH, Eisen LA. Non-invasive Methods of Estimating Intracranial Pressure. Neurocrit Care 2011;15(3):599-608. Available from: http://ClinicalTrials.gov/search/term=21519957%20%5BPUBMED-IDS%5D PubMed PMID: 21519957. doi: 10.1007/s12028-011-9545-4.

19. Geeraerts T, Launey Y, Martin L, Pottecher J, Vigué B, Duranteau J, et al. Ultrasonography of the optic nerve sheath may be useful for detecting raised intracranial pressure after severe brain injury. Intensive Care Med 2007 Aug;33(10):1704-1711. Available from: http://ClinicalTrials.gov/search/term=17668184%20%5BPUBMED-IDS%5D PubMed PMID: 17668184. doi: 10.1007/s00134-007-0797-6.

20. Siaudvytyte L, Januleviciene J, Ragauskas A, Bartusis L, Siesky B, Harris A. Update in intracranial pressure evaluation methods and translaminar pressure gradient role in glaucoma. Acta Ophthalmol 2015;93(1):9-15. Available from: http://dx.doi.org/10.1111/aos.12502 PubMed PMID: 25043873. doi: 10.1111/aos.12502.

21. Ragauskas A, Daubaris G, Dziugys A, Azelis V, Gedrimas V. Innovative non-invasive method for absolute intracranial pressure measurement without calibration. Acta Neurochir Suppl 2005;95:357-361. Available from: https://www.nlm.nih.gov/medlineplus/traumaticbraininjury.html PubMed PMID: 16463881.

22. Ragauskas A, Matijosaitis V, Zakelis R, Petrikonis K, Rastenyte D, Piper I, et al. Clinical assessment of noninvasive intracranial pressure absolute value measurement method. Neurology 2012 May;78(21):1684-1691. Available from: http://ClinicalTrials.gov/search/term=22573638%20

%5BPUBMED-IDS%5D PubMed PMID: 22573638. doi: 10.1212/WNL.0b013e3182574f50.

23. Wilensky JT. Diurnal variations in intraocular pressure. Trans Am Ophthalmol Soc 1991;89:757-790. Available from: http://europepmc.org/abstract/MED/1687295 PubMed PMID: 1687295.

24. Flammer J, Orgül S, Costa VP, Orzalesi N, Krieglstein GK, Serra LM, et al. The impact of ocular blood flow in glaucoma. Prog Retin Eye Res 2002;21(4):359-393. Available from: http://www.diseaseinfosearch.org/result/3065 PubMed PMID: 12150988. doi: 10.1016/S1350-9462(02)00008-3.

25. Asrani S, Zeimer R, Wilensky J, Gieser D, Vitale S, Lindenmuth K. Large diurnal fluctuations in intraocular pressure are an independent risk factor in patients with glaucoma. J Glaucoma 2000;9(2):134-142. Available from: http://www.scholaruniverse.com/ncbi-linkout?id=10782622 PubMed PMID: 10782622. doi: 10.1097/00061198-200004000-00002.

26. Wostyn P, Audenaert K, De Deyn PP. Alzheimer's disease-related changes in diseases characterized by elevation of intracranial or intraocular pressure. Clin Neurol Neurosurg 2008;110(2):101-109. Available from: http://linkinghub.elsevier.com/retrieve/pii/S0303846707003162 PubMed PMID: 18061341. doi: 10.1016/j.clineuro.2007.10.011.

27. Triyoso DH, Good TA. Pulsatile shear stress leads to DNA fragmentation in human SH-SY5Y neuroblastoma cell line. J Physiol 1999 Mar;515(2):355-365. Available from: http://onlinelibrary.wiley.com/resolve/openurl?genre=article&sid=nlm:pubmed&issn=0022-3751&date=1999&volume=515&issue=&spage=355 PubMed PMID: 10050003. doi: 10.1111/j.1469-7793.1999.355ac.x.

28. Edwards ME, Wang SS, Good TA. Role of viscoelastic properties of differentiated SH-SY5Y human neuroblastoma cells in cyclic shear stress injury. Biotechnol Prog 2001;17(4):760-767. Available from: http://www.scholaruniverse.com/ncbi-linkout?id=11485440 PubMed PMID: 11485440. doi: 10.1021/bp010040m.

29. Starcevic VP, Morrow BA, Farner LA, Keil LC, Severs WB. Long-term recording of cerebrospinal fluid pressure in freely behaving rats. Brain Research 1988;462(1):112-117. Available from: http://linkinghub.elsevier.com/retrieve/pii/0006899388905926 doi: 10.1016/0006-8993(88)90592-6.

30. Maurel D, Ixart G, Barbanel G, Mekaouche M, Assenmacher I. Effects of acute tilt from orthostatic to head-down antiorthostatic restraint and of sustained restraint on the intra-cerebroventricular pressure in rats. Brain Res 1996;736(1-2):165-173. Available from: https://www.researchgate.net/publication/e/pm/8930321?ln_t=p&ln_o=linkout PubMed PMID: 8930321. doi: 10.1016/0006-8993(96)00676-2.

31. Morrow BA, Starcevic VP, Keil LC, Seve WB. Intracranial hypertension after cerebroventricular infusions in conscious rats. Am J Physiol 1990;258(5 Pt 2). Available from: https://www.researchgate.net/publication/e/pm/2337198?ln_t=p&ln_o=linkout PubMed PMID: 2337198.

32. Lin JS, Liu JKH. Circadian Variations in Intracranial Pressure and Translaminar Pressure Difference in Sprague-Dawley Rats. Invest Ophthalmol Vis Sci 2010;51(11):5739-43. Available from: http://iovs.arvojournals.org/article.aspx?doi=10.1167/iovs.10-5542 PubMed PMID: 20574015. doi: 10.1167/iovs.10-5542.

33. Nilsson C, Ståhlberg F, Thomsen C, Henriksen O, Herning M, Owman C. Circadian variation in human cerebrospinal fluid production measured by magnetic resonance imaging. Am J Physiol 1992;262:1992-262.

34. Nilsson C, Ståhlberg F, Gideon P, Thomsen C, Henriksen O. The nocturnal increase in human cerebrospinal fluid production is inhibited by a beta 1-receptor antagonist. Am J Physiol 1994;267(6 Pt 2):1994-267. Available from: http://toxnet.nlm.nih.gov/cgi-bin/sis/search2/r?dbs+hsdb:@term+@rn+29122-68-7 PubMed PMID: 7810751.

35. Johanson CE, Duncan 3rd JA, Klinge PM, Brinker T, Stopa EG, Silverberg GD. Multiplicity of cerebrospinal fluid functions: New challenges in health and disease. Cerebrospinal Fluid Res 2008;5(1):10. Available from: http://www.cerebrospinalfluidresearch.com/content/5//10 PubMed PMID: 18479516. doi: 10.1186/1743-8454-5-10.

36. Kropyvnytskyy IV, Saunders FW, Klemfuss H. Circadian rhythm of cerebral perfusion pressure and

intracranial pressure in head injury. Brain Inj 1999;13(1):45-52. Available from: https://www.nlm.nih.gov/medlineplus/headinjuries.html PubMed PMID: 9972442. doi: 10.1080/026990599121872.

37. Berdahl JP, Allingham RR. Intracranial pressure and glaucoma. Curr Opin Ophthalmol 2010;21(2):106-111. Available from: http://www.diseaseinfosearch.org/result/3065 PubMed PMID: 20040876. doi: 10.1097/ICU.0b013e32833651d8.

38. Roux, P. Le, , Menon DK, Citerio G, Vespa P, Bader MK, Brophy GM, et al. Consensus summary statement of the International Multidisciplinary Consensus Conference on Multimodality Monitoring in Neurocritical Care: a statement for healthcare professionals from the Neurocritical Care Society and the European Society of Intensive Care Medicine. Intensive Care Med 2014;40(9):1189-209. Available from: http://link.springer.com/10.1007/s00134-014-3369-6 doi: 10.1007/s00134-014-3369-6.

39. Magnaes B. Body position and cerebrospinal fluid pressure. Part 2: clinical studies on orthostatic pressure and the hydrostatic indifferent point. J Neurosurg 1976;44(6):698-705. Available from: http://www.lens.org/lens/search?q=citation_id:1271090 PubMed PMID: 1271090. doi: 10.3171/jns.1976.44.6.0698.

40. Lenfeldt N, Koskinen LD, Bergenheim AT, Malm J, Eklund A. CSF pressure assessed by lumbar puncture agrees with intracranial pressure. Neurology 2007 Jan;68(2):155-158. Available from: https://www.researchgate.net/publication/e/pm/17210899?ln_t=p&ln_o=linkout PubMed PMID: 17210899. doi: 10.1212/01.wnl.0000250270.54587.71.

41. Ren R, Jonas JB, Tian G, Zhen Y, Ma K, Li S, et al. Cerebrospinal fluid pressure in glaucoma: a prospective study. Ophthalmol 2010;117:259-66.

42. Mitchell P, Lee AJ, Wang JJ, Rochtchina E. Intraocular pressure over the clinical range of blood pressure: Blue Mountains Eye Study findings. Am J Ophthalmol 2005;140:131-2.

43. Xu L, Wang H, Wang Y, Jonas JB. Intraocular pressure correlated with the arterial blood pressure: The Beijing Eye Study. Am J Ophthalmol 2007;144:461-2.

44. Samuels BC, Hammes NM, Johnson PL, Shekhar A, McKinnon SJ, Allingham RR. Dorsomedial/Perifornical hypothalamic stimulation increases intraocular pressure, intracranial pressure, and the translaminar pressure gradient. Invest Ophthalmol Vis Sci 2012;53(11):7328-35.

45. Durward QJ, Amacher AL, Maestro, R.F. Del , Sibbald WJ. Cerebral and cardiovascular responses to changes in head elevation in patients with intracranial hypertension. J Neurosurg 1983;59(6):938-44.

46. Magnaes B. Body position and cerebral fluid pressure. Part 1: Clinical studies on the effect of rapid postural changes. J Neurosurg 1976;44(6):687-97.

47. Choi J, Jeong J, Cho HS, Kook MS. Effect of nocturnal blood pressure reduction on circadian fluctuation of mean ocular perfusion pressure: a risk factor for normal tension glaucoma. Invest Ophthalmol Vis Sci 2006;47:831-6.

48. Costa VP, Harris A, Anderson D, Stodtmeister R, Cremasco F, Kergoat H, et al. Ocular perfusion pressure in glaucoma. Acta Ophthalmol 2013 Nov;92(4):252-66. Available from: http://dx.doi.org/10.1111/aos.12298 PubMed PMID: 24238296. doi: 10.1111/aos.12298.

49. Malm J, Jacobsson J, Birgander R, Eklund A. Reference values for CSF outflow resistance and intracranial pressure in healthy elderly. Neurology 2011 Mar;76(10):903-909. Available from: http://www.scholaruniverse.com/ncbi-linkout?id=21383326 PubMed PMID: 21383326. doi: 10.1212/WNL.0b013e31820f2dd0.

50. Czosnyka M, Czosnyka ZH, Whitfield PC, Donovan T, Pickard JD. Age dependence of cerebrospinal pressure-volume compensation in patients with hydrocephalus. J Neurosurg 2001;94(3):482-486. Available from: http://www.diseaseinfosearch.org/result/3510 PubMed PMID: 11235954. doi: 10.3171/jns.2001.94.3.0482.

51. Fleischman D, Berdahl JP, Zaydlarova J, Stinnett S, Fautsch MP, Allingham RR. Cerebrospinal fluid pressure decreases with older age. PLoS One 2012 Dec;7(12):52664. Available from: http://dx.plos.org/10.1371/journal.pone.0052664 PubMed PMID: 23300737. doi: 10.1371/journal.pone.0052664.

52. Fleischman D, Allingham RR, Berdahl J, Fautsch M. Body mass, spinal fluid, and glaucoma. Ophthalmology 2011;118(6):1225-6. Available from: http://linkinghub.elsevier.com/retrieve/pii/S0161642011000583 doi: 10.1016/j.ophtha.2011.01.025.

53. Ren R, Wang N, Zhang X, Tian G, Jonas JB. Cerebrospinal fluid pressure correlated with body mass index. Graefes Arch Clin Exp Ophthalmol 2011 Aug;250(3):445-446. Available from: https://www.researchgate.net/publication/e/pm/21814821?ln_t=p&ln_o=linkout PubMed PMID: 21814821. doi: 10.1007/s00417-011-1746-1.

54. Berdahl JP, Fleischman D, Zaydlarova J, Stinnett SS, Allingham RR, Fautsch MP. Body Mass Index has a linear relationship with Cerebrospinal Fluid Pressure. Invest Ophthalmol Vis Sci 2012;53(3):1422-7. Available from: http://iovs.arvojournals.org/article.aspx?doi=10.1167/iovs.11-8220 doi: 10.1167/iovs.11-8220.

55. Loewn NA, Tanna AP. Glaucoma risc factors: Intraocular pressure. Clinical glaucoma care. The essentials. Chapter 1, 1st ed. Springer; .

56. Ragauskas A, Bartusis L, Piper I, Zakelis R, Matijosaitis V, Petrikonis K, et al. Improved diagnostic value of a TCD-based non-invasive ICP measurement method compared with the sonographic ONSD method for detecting elevated intracranial pressure. Neurol Res 2014;36(7):607-614. Available from: http://ClinicalTrials.gov/search/term=24620972%20%5BPUBMED-IDS%5D PubMed PMID: 24620972. doi: 10.1179/1743132813Y.0000000308.

57. Killer HE, Laeng HR, Flammer J, Groscurth P. Architecture of arachnoid trabeculae, pillars, and septa in the subarachnoid space of the human optic nerve: anatomy and clinical considerations. Br J Ophthalmol 2003;87(6):777-781. Available from: http://bjo.bmj.com/cgi/pmidlookup?view=long&pmid=12770980 PubMed PMID: 12770980. doi: 10.1136/bjo.87.6.777.

58. Killer HE, Jaggi GP, Miller NR, Flammer J, Meyer P. Does immunohistochemistry allow easy detection of lymphatics in the optic nerve sheath?. J Histochem Cytochem 2008 Sep;56(12):1087-1092. Available from: http://europepmc.org/abstract/MED/18765840 PubMed PMID: 18765840. doi: 10.1369/jhc.2008.950840.

59. Killer HE, Miller NR, Flammer J, Meyer P, Weinreb RN, Remonda L, et al. Cerebrospinal fluid exchange in the optic nerve in normal-tension glaucoma. Br J Ophthalmol 2011 Nov;96(4):544-548. Available from: http://www.diseaseinfosearch.org/result/3065 PubMed PMID: 22116958. doi: 10.1136/bjophthalmol-2011-300663.

Assessment and comparison of the morphology and function of the corneal sub-basal nerve plexus in type-1 diabetes mellitus patients and in healthy subjects

Irmante Derkac[1], Ingrida Januleviciene[1], Kirwan Asselineau[1], Dzilda Velickiene[2]

[1]Department of Ophthalmology, Hospital of Lithuanian University of Health Sciences Kaunas Clinics, Kaunas, Lithuania; [2]Endocrinology institute, Lithuanian University of Health Sciences, Kaunas, Lithuania

Abstract

Aim/purpose: It is believed that small nerve bundles are damaged in the earliest stages of neuropathy caused by diabetes mellitus (DM). Our goal was to evaluate and compare anatomical characteristics of corneal nerve fibers and corneal sensitivity in type-1 DM patients and in healthy control subjects.
Design: A prospective, masked, controlled cross-sectional clinical study.
Method: Thirty patients with type-1 DM and ten non-diabetic healthy subjects underwent a corneal confocal microscopy to evaluate the corneal sub-basal nerve fibers (density, number of nerves and branches, total nerve length) and contact corneal esthesiometry.
Results: Diabetic patients had significantly lower corneal nerve fiber density density (14.32 ± 5.87 vs. 19.71 ± 5.59 mm/mm2; p = 0.023) nerve branches number (4.57 ± 3,91 vs. 9.90 ± 5.8 n°/image; p = 0.006) , nerve fiber length (2.28 ± 0.94 vs. 3.13 ± 0.89 mm; p = 0.032) and corneal sensitivity (1.13 ± 0.29 vs. 0.98 ± 0.058 gr/mm2 p = 0.02), as compared with controls. A negative correlation was found between corneal nerve fiber length, corneal nerve number, corneal nerve fiber density and disease duration (p < 0.05).
Conclusion: Corneal confocal microscopy and corneal sensitivity evaluation are

---

Correspondence: Irmante Derkac MD, Department of Ophthalmology, Hospital of Lithuanian University of Health Sciences Kaunas Clinics, Eiveniu 2, LT-50009, Kaunas, Lithuania. E-mail: irmantederkac@gmail.com.

noninvasive techniques helping to detect early changes in the sub-basal nerve plexus characteristic for diabetic neuropathy (DN) in patients with type-1 DM. Further studies are required to investigate the role of corneal neuropathy assessment using these novel techniques as a toll to detect early DN.

Key words: contact corneal esthesiometry, corneal confocal microscopy, corneal sensitivity, diabetes mellitus, diabetic neuropathy.

1. Introduction

Diabetic neuropathy (DN) is a significant and prevalent complication of diabetes mellitus (DM), which has no effective treatment once established and can ultimately result in foot ulceration and lower extremity amputation.[1] Up to 50% of patients with DM will develop distal symmetric polyneuropathy at some point during their illness.[2] The natural history of nerve damage in patients with type-1 DM is not entirely clear but we do know that the development of diabetic neuropathy has been related not only to glycemic control but also to conventional cardiovascular risk factors such as hypertension and dyslipidemia.[3] Unfortunately, demonstrating an improvement in neuropathy over time has been much more difficult to achieve than preventing progression.[4] Recent studies demonstrated significant abnormalities in the small fibers in subjects with impaired glucose tolerance and DM, despite normal electrophysiology, suggesting that the earliest nerve fiber damage is to the small fibers. Clinical assessments and scales have the advantage of taking into account the patients' symptoms and a neurologic examination, but a recent work has indicated that this approach may have a poor reproducibility.[5]

Traditional neuropathy diagnostic tools do not objectively and accurately assess small nerve fibers, which are often the first to be injured and perhaps the first to be repaired[6], and which has a very important value in clinical trials when investigating interventions for the prevention and treatment of DN. Although electrophysiology correlates with large fiber's damage, it does not assess small fibers (Aδ and C fibers) and the test for preclinical small nerve damage, the skin punch biopsy, which can detect intra-epidermal nerve fiber density and is generally regarded as the gold standard of small nerve fiber degeneration is an invasive procedure.[7,8] Several groups have reported the use of corneal confocal microscopy (CCM) evaluation of corneal nerve structures and corneal sensitivity measurement as a reliable assessments of DN[9,10] and has been shown to be effective as a rapid, noninvasive, repeatable tool that allows detection of neuropathy in patients with DM.[11] In this study we assessed the corneal sensitivity and corneal nerve morphology using contact corneal esthesiometry and CCM in DM patients and healthy control subjects aiming to detect and compare small corneal nerves alterations that might possibly predict development of neuropathy and stratify diabetic patients with increasing neuropathic severity.

2. Materials and methods

2.1. Subjects

This prospective, masked, controlled cross-sectional clinical study, conducted in accordance with the Declaration of Helsinki with the approval of the Human Research Committee with applicable regulations pertaining to Good Clinical Practice was conducted in the Eye Clinic and Endocrinology Clinic of the Lithuanian University of Health Sciences' Hospital.

All subjects were 18 and older and all signed an informed consent form. The patients underwent a single medical examination during which several factors were assessed (age, gender, diabetes mellitus duration, glycated hemoglobin A1c (HbA1c), detailed medical history, family history, lifestyle factors, comorbidities, etc.) and the ophthalmological examination performed (best corrected visual acuity, refraction, intraocular pressure, biomicroscopy, ophthalmoscopy, corneal confocal microscopy, contact corneal esthesiometry).

The study group included type-1 DM patients whereas the control group included healthy subjects.

Exclusion criteria: neuropathy attributable to causes other than diabetes, diseases known to affect the corneal sub-basal innervation (*i.e.*, Herpes zoster), contact-lens wear, concomitant active or past corneal or ocular surface diseases (*i.e.*, active or a history of ocular herpes simplex infection), systemic disease known to affect the corneal sub-basal innervation, (*i.e.*, dry eye in Sjögren syndrome), corneal dystrophy, previous corneal surgery, corneal opacification or visible corneal edema, severe movement disorders (strabismus, nystagmus, poor compliance, or fixation issues),[12-15] refractive laser procedure (LASIK) in the past five years,[16] known allergy to proparacaine .

DM type 1 was defined based on the following criteria for the diagnosis of diabetes: symptoms of diabetes (polydipsia, polyuria, weight loss, fatigue, dizziness, nausea etc.) plus casual plasma glucose concentration ≥ 11.1 mmol/l or Fasting Plasma Glucose (FPG) ≥ 7.0 mmol/l twice on two separate days. Diabetic neuropathy was defined using a modified Neuropathy Disability Score (NDS), which is based on the assessment of ankle reflexes and sensory modalities on the big toes of both feet, and scored: (i) ankle reflexes (0, normal; 1, present with reinforcement; 2, absent); (ii) vibration with a 128-Hz tuning fork; (iii) pinprick; and (iv) temperature (warm and cool) (0, normal; 1, abnormal). Final scores of 3-5, 6-8 and 9-10 were considered to be evidence of mild, moderate and severe clinical neuropathy, respectively.[17]

2.2. Corneal confocal microscopy

All participants underwent in-vivo corneal confocal microscopy (IVCCM) examination of the sub-basal nerve fiber plexus (SNP), comprised between the basal epithelium and the Bowman's layer of the cornea scanned with a laser IVCCM (Heidelberg Engineering GmbH, Heidelberg, Germany) to produce a 0.4 mm x 0.4 mm (384 pixel

x 384 pixel) applying an established methodology.[18] The device is a laser-scanning confocal microscope that uses a visible 670 nm red wavelength diode laser source. The subject's eyes were topically anesthetized using a drop of 0.5% proparacaine hydrochloride, and an ocular 2% carbomer containing gel was applied on the surface of the eye for lubrication. A drop of gel was placed on the tip of the objective lens, which was covered by a sterile disposable TomoCap® to allow the optical coupling of the objective lens to the cornea after another drop of gel had been applied on the surface of the TomoCap® Subjects fixed their gaze on a target positioned behind the corneal confocal microscope device and the examiner used a side-view digital video camera to ensure the apex of the central cornea was scanned. Five to ten high-quality images with the best resolution of the SNP were acquired from the center of the cornea.

The investigator who examined the cornea and undertook morphometric measurements of the images was masked with respect to the identity of the patients as well as medical and neurological results of the subjects. From the images showing well-focused nerves from the central cornea, one image was randomly selected. The priority was given to the picture with the highest quality. The SNP density was calculated, defined by the length of nerves per square millimeters of image area.[9] The following variables were quantified: (1) corneal nerve fiber density (CNFD) – the total number of all nerve fibers per mm^2 (in mm/mm^2); (2) corneal nerve fiber length (CNFL) – the total length of nerve fiber in mm; (3) corneal nerve branches number (CNBN) – the number of branches per image; (4) corneal nerve number per image (CNN) – the total number of major nerves per image. Measures 1 and 2 were calculated using the NeuronJ plug-in of the computer software ImageJ (ImageJ 1.49d, the Java-based image processing environment developed at the National Institutes of Health, Bethesda, MD, USA), which allows a manual semi-automatic nerve tracing and further calculation of the nerve plexus. The pictures on a single plane were mandatory, no oblique pictures were selected, and only the visible parts of the nerve were marked with the ImageJ software.[18]

2.3. Corneal sensitivity

Corneal sensitivity examination is performed to assess the sensory function of the cornea. The examination was carried out using a handheld Cochet-Bonnet esthesiometer (Luneau Ophtalmologie, France), which allows to measure the sensation level and record its numerical value. The device relies on the principle of contact esthesiometry. It contains a thin (0.12 mm in diameter), retractable, nylon monofilament, which has a length that can be regulated in order to increase or reduce the amount of pressure applied. The fully extended length of nylon filament was 60 mm, at which length the cornea was firstly tested. If a positive answer was not detected the filament length was shortened by steps of five mm and the procedure was repeated until a positive response was obtained and each of the pressure value obtained was written down.[9,19]

Five positions were tested in each eye using the esthesiometer, the first one being the central cornea. The cornea was then virtually divided horizontally and vertically into four quadrants, which were tested one after the other. After all five zones had been tested, the average pressure needed to elicit a positive answer was calculated.

2.4. Statistics

SPSS 17.0 for Windows was used to compute the results. The analysis included descriptive and frequency statistics. All data are expressed as means (x(SD)). P value less than 0.05 was considered as significant. The Mann-Whitney test was used to compare patients with type-1 diabetes and controls.

3. Results

Thirty type-1 diabetic patients aged 34 ± 10.4 years and ten control subjects aged 29 ± 11.2 years were included in the study (p = 0.13). There were statistically more female patients in the diabetic group than in control (p = 0.03) (participants characteristics are shown in Table 1).

Table 1. Clinical demographics and corneal sensitivity in control subjects and diabetic patients**.**

	Healthy volunteers (N = 10)	**Diabetic patients (N = 30)**	*p value*
Female sex, N (%)	6 (60%)	27 (90%)	**0.03**
Age (years)	29 ± 1.2	34 ± 10.4	0.13
Diabetes duration (years)	-	13 ± 9.8	-
HbA1c (%)	-	8,5 ± 1,4	-
CCM parameters:			
CNFL (mm)	3.14 ± 0.9 [3.13 (1.74; 4.59)]	2.29 ± 0.9 [2.27 (0.36; 3.87)]	**0.032**
CNFD (mm/mm^2)	19.72 ± 5.6 [20.06 (10.88; 28.71)]	14.32 ± 5.9 [14.19 (2.25;24.18)]	**0.023**
CNBN (number/image)	9.9 ± 5.8 [9 (2;22)]	4.6 ± 3.9 [3 (0;16)]	**0.006**
CNN (number/image)	5.7 ± 1.9 [6.0 (3;8)]	5.3 ± 1.9 [6 (1;8)]	0.67
Corneal sensitivity (gr/mm^2)	0.99 ± 0.06 [0.96 (0.96;1.14)]	1.13 ± 0.29 [1.01 (0.96; 2.24)]	**0.02**

Mean ± SD [median (min.; max.)]. p values were calculated with non-parametric Mann-Withey Test, significance level p < 0.05. HbA1c = Glycated hemoglobin A1c; CNFL = corneal nerve fiber length; CNFD = corneal nerve fiber density; CNBN = corneal nerve branches number; CNN = corneal nerves number.
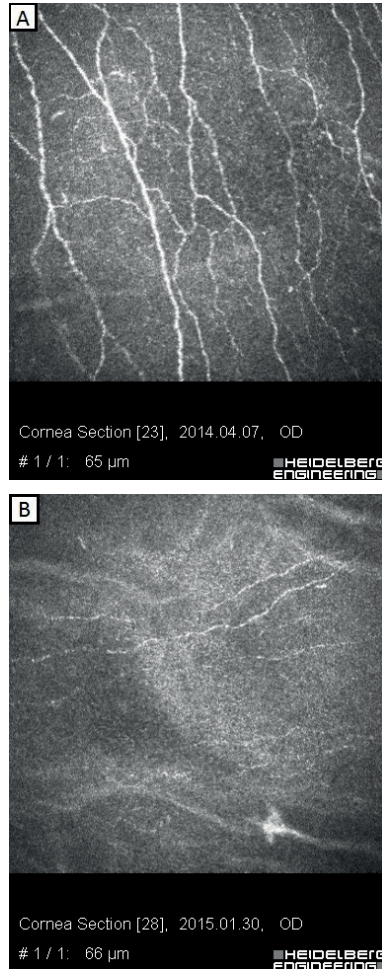
Fig. 1. CCM images from Bowman's layer of cornea: **A.** A 23-years-old healthy patient, CNFD 21.81 mm/mm^2, corneal sensitivity 1.14 gr/mm^2. **B.** A 35-years-old patient, diabetes duration 23 years, CNFD 14.15 mm/mm^2, corneal sensitivity 1.43 gr/mm^2.

Safety: none of the participants experienced any visual or corneal sequelae as a result of the examinations.

Figure 1 displays a sample of the pictures obtained using the CCM. The inter-connected sub-basal nerve fiber plexus is represented as elongated hyperreflec-tive structures in both a DM and a healthy person at the sub-basal level, located between the basal layer of the epithelium and the Bowman's membrane (Fig. 1).

Diabetic patients compared to controls had a significantly lower CNFL (2.28 ± 0.94 vs. 3.13 ± 0.89 mm; p = 0.032), CNFD (14.32 ± 5.87 vs. 19.71 ± 5.59 mm/mm^2; p

= 0.023), CNBN (4.57 ± 3.91 vs. 9.90 ± 5.8 no/image; p = 0.006), while the CNN values were not statistically significantly different between the two groups (5.3 ± 1.9 vs. 5.7 ± 1.9 n°/image; p = 0.67). Estimated corneal sensitivity was also lower in diabetic patients group compared to the healthy controls (0.99 ± 0.06 vs. 1.13 ± 0.29 gr/mm^2; p = 0.02). A negative correlation was found between CNFL, CNN, CNFD and diabetes duration (r = -0.366, r = - 0.464, r = -0.363; p < 0.05, respectively) and no statistical significance was found between diabetes duration and corneal sensitivity (p > 0.05) (Figs. 2, 3, 4). There were no statistically significant correlations between HbA1c, corneal sensitivity and sub-basal nerve parameters in the diabetic subjects group. We found no correlations between age and SNP morphological changes or corneal sensitivity in both diabetic and healthy control groups (p > 0,05).

4. Discussion

DN development is the main initiating factor for foot ulceration and lower extremity amputation. The lack of early biomarkers for nerve injury hinders the process of drug development in clinical research, which highlights the urgent need for a valid screening test in clinical practice that overcomes the limitations in their specificity as predictive markers for the future onset of neuropathy.[20] Over the past decade there has been increasing research interest in modeling the relationship between corneal nerve fiber loss and diabetes. There is evidence suggesting that CCM can detect early small fiber changes in patients with type-1 diabetes without neuropathy and accurately quantify the severity of DN.[21]
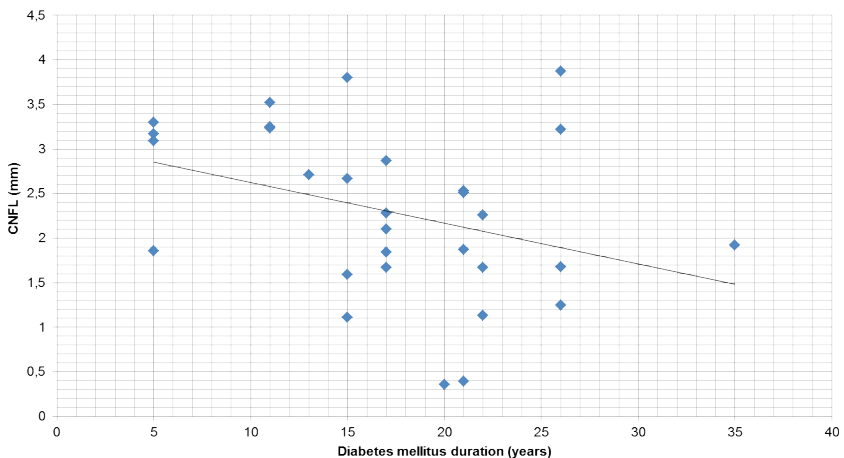

Fig. 2. Correlation between changes in nerve fiber density and duration of diabetes mellitus (r = -0.363, p = 0.049).
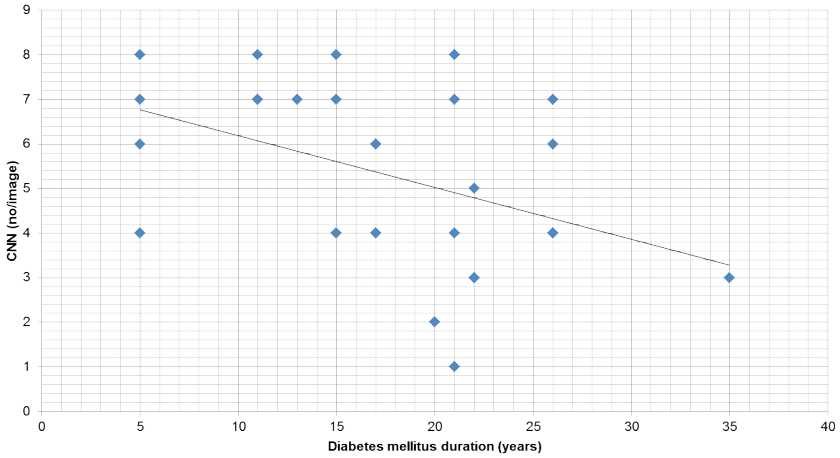
Fig. 3. Correlations between changes in nerve fiber length and duration of diabetes mellitus (r = -0.366, p = 0.046)
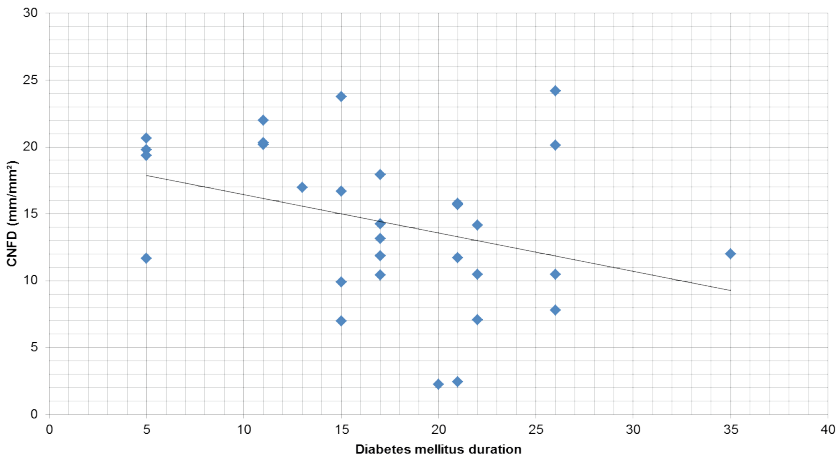

Fig. 4. Correlations between changes in nerve fiber number and duration of diabetes mellitus (r = - 0.464, p = 0.010)

The purpose of this cross-sectional study was to evaluate the differences of corneal sub-basal nerve plexus and corneal sensitivity in subjects with type-1 DM and healthy controls. We hypothesized that values between diabetic and healthy control groups indicate incipient nerve injury that represents those individuals with future neuropathy risk. The study was conducted using two novel noninvasive measures of neuropathy, namely contact corneal esthesiometry and corneal

confocal microscopy.

Our study estimated that corneal sub-basal nerve plexus parameters and corneal sensitivity are significantly reduced in diabetic patients compared with healthy controls and these results are in agreement with several other studies.[9-11,22,23] Rosenberg et al. demonstrated that patients with type-1 DM have a reduction in corneal sensitivity and in the number of corneal nerve fiber bundles, and these correlate statistically significantly with the severity of neuropathy.[9] We did not stratify the severity of somatic nerve neuropathy in diabetic patients because of a small number of participants, who have been diagnosed with DN. In Tavakoli et al. study, 101 diabetic patients underwent neurological evaluation, the neuropathy deficit score (NDS) was established and the severity of neuropathy was determined. They demonstrated a progressive reduction in corneal sensitivity and increasing corneal nerve degeneration with increasing severity of diabetic neuropathy.[10] In another study conducted by Ishibashi et al., 38 controls and 38 diabetic patients were recruited. DN was not stratified into severity levels, but diabetic patients were divided into two groups based on the presence or absence of DN and was named as 'probable DN'. The authors also established that CCM parameters' alterations were found in patients without neuropathy compared with healthy subjects.[22]

We found no statistically significant correlations between HbA1c, corneal sensitivity and sub-basal nerve parameters in the diabetic patient's group. This could be due to a relatively small sample size. Ishibashi et al. found an inversed correlation between CNFD and CNFL and the mean annual HbA1c levels for a period of seven to ten years prior to the examination, suggesting that the mean HbA1c level during this period was an independent predictor of reduced CNFD and CNFL in type-1 DM, but, in their study, this significant correlation disappeared abruptly beyond ten years, probably because of a decrease in the number of subjects.[22]

Although another study conducted by Tavakoli et al., including 25 patients with DM, showed that improvement in nerve fiber density correlated significantly with the improvement in HbA1c ($r = -0.51$; $p = 0.008$) and confirmed the negative association between HbA1c and nerve fiber density ($P = 0.02$), they did not find significant correlations between HbA1c and other corneal sub-basal nerve parameters (i.e. corneal nerve branches number, nerve branch density, nerve fiber length, corneal nerves number).[24]

We did not find any statistically significant correlation between gender, corneal sensitivity and sub-basal nerve parameters. In our study, there were more female than male patients (40 participants, 33 of which were females), however, in a 2013 study conducted by Parissi et al. including 106 patients, 59 of which were females and 47 males, no differences in the mean sub-basal nerve density between genders were identified.[18]

Interestingly, our study showed that diabetes duration is negatively correlated to CNFL, CNN, CNFD ($p < 0.05$) and that the disease duration has no significant correlation with corneal sensitivity ($p = 0.295$), while Ishibashi et al. found no statis-

tically significant correlation, despite a very similar duration of diabetes in studies (13 ± 9.8 vs.15.4 ± 1.5 years). These discrepancies might become significant because of the different number of diabetic participants. Also Ishibashi *et al.* found no difference in nerve branches between controls and diabetic patients,[22] whereas our study showed that the number of nerve branches was statistically significantly lower in the diabetic group compared to healthy patients (p < 0.05). The branches, when analyzed by CCM, possess a smaller diameter than the main nerve trunks. They were significantly less numerous in diabetic patients than in our control group, which may confirm that smaller diameter nerve fibers, corresponding to sensory nerve fibers, are affected primarily in the course of DN, and they are probably responsible for the increased threshold required to elicit a corneal sensation.[7] In contrast with another study conducted by Rosenberg *et al.*,[9] we did not find statistically significant changes in CNN between both groups (p = 0.67), while they found that patients with diabetes had less nerve fiber bundles than healthy control subjects (p = 0.035).[9] This might be due to differences in estimation methods, in the evaluation of the branches and nerves per image. Also different from our study, where we did not find any significant correlation, Rosenberg *et al.* estimated that corneal sensitivity was inversely correlated with the duration of diabetes (r = -0.630; p = 0.001) and this might be caused by discrepancies in diabetes duration mean between both studies (13 ± 9.8 vs. 25.9 ± 8.1 years).[9]

Despite the results, showing similarities between different studies, there are differences not only in the number of participants, but also in the methodologies and in the technique of images capture, selection, and analysis. First of all, some investigations that quantified CCM parameters in diabetic and healthy subjects used slit-scanning confocal microscopy,[9] and not laser scanning microscopy. Different software was used to measure CCM parameters, which makes it more difficult to compare the parameters between healthy controls and diabetic patients. Secondly, although diminished, corneal sensitivity in diabetes with symmetrical involvement was first described by Schwartz using a Cochet and Bonnet esthesiometer (and later by others),[25] there were differences in corneal sensitivity assessment methods in some recent studies. Tavakoli *et al.* also found significant differences of corneal sensitivity between diabetic and healthy persons (p < 0.001), but the study was conducted using a noncontact corneal esthesiometer (NCCA) and assessing just the center of the cornea,[10] which differed from our study.

We acknowledge limitations to the interpretation of our results. Firstly, the data were cross-sectional and correlated with clinical factors retrospectively. Although we define diagnostic thresholds for CNFL, we acknowledge that the small number of participants, differences in gender sample and measurement error could limit the precision of these specific threshold values. Secondly, although we evaluated the corneal sensitivity, it was performed by contact corneal esthesiometry, and not using newer non-contact gas-esthesiomer, which is due to the very limited availability of such devices.[1] Thirdly, we acknowledge that protocols using fully automated

image analysis will likely be needed for this diagnostic test to be generalized into clinical practice.[26-27]

Because of such limitations, a longitudinal study, including more participants, a similar number of different genders and more data concerning the relationship between the morphological anomalies on CCM and the contributing clinical factors is needed.

Many studies use a cross-sectional methodology and it is still unclear how the early nerve regeneration seen in the cornea could be related to the functional improvements of peripheral neuropathy. The possibility remains that corneal nerves and sensory/motor nerves in the feet are unrelated. At present, underdiagnoses impede the benefits of early identification, thus delaying early management and prevention of neuropathy. Although CCM and corneal esthesiometry have the potential to be a game changer in the neuropathy outcome assessment, additional researches[28] as well as a longitudinal study are needed to provide more robust data regarding the ability of CCM to identify patients at risk of developing neuropathy.

References

1. Pritchard N, Edwards K, Vagenas D, Shahidi AM, Sampson GP, Russell AW, et al. Corneal sensitivity as an ophthalmic marker of diabetic neuropathy.. Optom Vis Sci 2010;87(12):1003-1008. Available from: http://www.scholaruniverse.com/ncbi-linkout?id=21037498 PubMed PMID: 21037498. doi: 10.1097/OPX.0b013e3181fd6188.
2. Pirart J. [Diabetes mellitus and its degenerative complications: a prospective study of 4,400 patients observed between 1947 and 1973 (3rd and last part) (author's transl)].. Diabete Metab 1977;3(4):245-256. Available from: http://www.diseaseinfosearch.org/result/2236 PubMed PMID: 598565.
3. Tesfaye S, Chaturvedi N, Eaton SE, Ward JD, Manes C, Ionescu-Tirgoviste C, Witte DR, Fuller JH, Group EPCS. Vascular risk factors and diabetic neuropathy. N Engl J Med 2005 Jan;352(4):341-350. Available from: http://www.nejm.org/doi/abs/10.1056/NEJMoa032782?url_ver=Z39.88-2003&r-fr_id=ori:rid:crossref.org&rfr_dat=cr_pub%3dwww.ncbi.nlm.nih.gov PubMed PMID: 15673800. doi: 10.1056/NEJMoa032782.
4. Group, D.C.a.C.T.R. (The). The effect of intensive treatment of diabetes on the development and progression of long-term complications in insulin-dependent diabetes mellitus. N Engl J Med 1993;329(14):977-986. Available from: http://www.nejm.org/doi/abs/10.1056/NEJM199309303291401 doi: 10.1056/NEJM199309303291401.
5. Dyck PJ, Overland CJ, Low PA, Litchy WJ, Davies JL, Dyck PJ, O'Brien PC,,, , vs C. NPhys Trial Investigators, Albers JW, Andersen H, Bolton CF, England JD, Klein CJ, Llewelyn JG, Mauermann ML, Russell JW, Singer W, Smith AG, Tesfaye S, Vella A. Signs and symptoms versus nerve conduction studies to diagnose diabetic sensorimotor polyneuropathy: Cl vs. NPhys trial. Muscle Nerve 2010;42(2):157-164. Available from: http://europepmc.org/abstract/MED/20658599 PubMed PMID: 20658599. doi: 10.1002/mus.21661.
6. Smith AG, Russell J, Feldman EL, Goldstein J, Peltier A, Smith S, et al. Lifestyle intervention for pre-diabetic neuropathy.. Diabetes Care 2006;29(6):1294-1299. Available from: http://www.scholaruniverse.com/ncbi-linkout?id=16732011 PubMed PMID: 16732011. doi: 10.2337/dc06-0224.
7. Tavakoli M, Mitu-Pretorian M, Petropoulos IN, Fadavi H, Asghar O, Alam U, et al. Corneal confocal microscopy detects early nerve regeneration in diabetic neuropathy after simultaneous pancreas and kidney transplantation. Diabetes. 2013 Jan;62(1):254-60. Diabetes 2012 Sep;62(1):254-260. Available

from: http://diabetes.diabetesjournals.org/cgi/pmidlookup?view=long&pmid=23002037 PubMed PMID: 23002037. doi: 10.2337/db12-0574.

8. England JD, Gronseth GS, Franklin G, Carter GT, Kinsella LJ, Cohen JA, Asbury AK, Szigeti K, Lupski JR, Latov N, Lewis RA, Low PA, Fisher MA, Herrmann DN, Howard JF Jr, Lauria G, Miller RG, Polydefkis M, Sumner AJ,, , Neurology, A.o. (American) . Practice Parameter: evaluation of distal symmetric polyneuropathy: role of autonomic testing, nerve biopsy, and skin biopsy (an evidence-based review). Report of the American Academy of Neurology, American Association of Neuromuscular and Electrodiagnostic Medicine, and American Academy of Physical Medicine and Rehabilitation. Neurology 2009 Jan;72(2):177-184. Available from: http://www.scholaruniverse.com/ncbi-linkout?id=19056667 PubMed PMID: 19056667. doi: 10.1212/01.wnl.0000336345.70511.0f.

9. Rosenberg ME, Tervo TM, Immonen IJ, Müller LJ, Grönhagen-Riska C, Vesaluoma MH. Corneal structure and sensitivity in type 1 diabetes mellitus.. Invest Ophthalmol Vis Sci 2000;41(10):2915-2921. Available from: http://www.diseaseinfosearch.org/result/2236 PubMed PMID: 10967045.

10. Tavakoli M, Quattrini C, Abbott C, Kallinikos P, Marshall A, Finnigan J, et al. Corneal confocal microscopy: a novel noninvasive test to diagnose and stratify the severity of human diabetic neuropathy. Diabetes Care. 2010 Aug;33(8):1792-7. Diabetes Care 2010 Apr;33(8):1792-1797. Available from: http://europepmc.org/abstract/MED/20435796 PubMed PMID: 20435796. doi: 10.2337/dc10-0253.

11. Ahmed A, Bril V, Orszag A, Paulson J, Yeung E, Ngo M, et al. Detection of diabetic sensorimotor polyneuropathy by corneal confocal microscopy in type 1 diabetes: a concurrent validity study. Diabetes Care. 2012 Apr;35(4):821-8. Epub 2012 Feb;PubMed Central PMCID. PubMed PMID: 22323412. doi: 10.2337/dc11-1396.

12. Patel DV, McGhee CNJ. Mapping the corneal sub-basal nerve plexus in keratoconus by in vivo laser scanning confocal microscopy.. Invest Ophthalmol Vis Sci 2006;47(4):1348-1351. Available from: http://www.diseaseinfosearch.org/result/3973 PubMed PMID: 16565367. doi: 10.1167/iovs.05-1217.

13. Tuominen ISJ, Konttinen YT, Vesaluoma MH, Moilanen JAO, Helinto¨ M, Tervo TMT. Corneal Innervation and Morphology in Primary Sjögren's Syndrome. Invest. Ophthalmol. Vis. Sci 2013 Oct;54(10):7091-2549. Available from: https://www.researchgate.net/publication/e/pm/24084094?ln_t=p&ln_o=linkout PubMed PMID: 24084094. doi: 10.1167/iovs.13-12999.

14. Jm, d . C. (Benitez), Wasfy MA, Fernandez C, Garcia-Sanchez J. An in vivo confocal masked study on corneal epithelium and subbasal nerves in patients with dry eye. Invest Ophthalmol Vis Sci 2004 2004;45(1):3030-3035. Available from: https://www.nlm.nih.gov/medlineplus/cornealdisorders.html PubMed PMID: 3051467. doi: 10.1016/0039-6257(88)90070-7.

15. Niederer RL, Perumal D, Sherwin T, McGhee CN. Corneal innervation and cellular changes after corneal transplantation: an in vivo confocal microscopy study. Invest Ophthalmol Vis Sci 2007 2007;48(8):621-626. Available from: http://diabetes.diabetesjournals.org/cgi/pmidlookup?view=long&pmid=17513704 PubMed PMID: 17513704. doi: 10.2337/db07-0285.

16. Erie JC, McLarenJW, Hodge DO , et al. Recovery of corneal subbasal nerve density after PRK and LASIK. Am J Ophthalmol 2005;140(6):1059-1064. Available from: https://www.researchgate.net/publication/e/pm/16376651?ln_t=p&ln_o=linkout PubMed PMID: 16376651. doi: 10.1016/j.ajo.2005.07.027.

17. Caselli A. Validation of the nerve axon reflex for the assessment of small nerve fibre dysfunction. Journal of Neurology, Neurosurgery & Psychiatry 2006 May;77(8):927-932. Available from: http://jnnp.bmj.com/cgi/doi/10.1136/jnnp.2005.069609 PubMed PMID: 24843565. doi: 10.1136/jnnp.2005.069609.

18. Parissi M, Karanis G, Randjelovic S, Germundsson J, Poletti E, Ruggeri A, et al. Standardized baseline human corneal subbasal nerve density for clinical investigations with laser-scanning in vivo confocal microscopy.. Invest Ophthalmol Vis Sci 2013 Oct;54(10):7091-7102. Available from: https://www.researchgate.net/publication/e/pm/24084094?ln_t=p&ln_o=linkout PubMed PMID: 24084094. doi: 10.1167/iovs.13-12999.

19. Martin XY, Safran AB. Corneal hypoesthesia. Surv Ophthalmol 1988;33(1):28-40. Available from: https://www.nlm.nih.gov/medlineplus/cornealdisorders.html PubMed PMID: 3051467. doi: 10.1016/0039-6257(88)90070-7.

20. Malik RA, Kallinikos P, Abbott CA, Schie, C.H.M. van , Morgan P, Efron N, et al. Corneal confocal microscopy: a non-invasive surrogate of nerve fibre damage and repair in diabetic patients. Diabetologia 2003;46(5):683-688.

21. Quattrini C, Tavakoli M, Jeziorska M, Kallinikos P, Tesfaye S, Finnigan J, et al. Surrogate markers of small fiber damage in human diabetic neuropathy. Diabetes 2007;56(8):2148-2154. Available from: http://diabetes.diabetesjournals.org/cgi/doi/10.2337/db07-0285 doi: 10.2337/db07-0285.

22. Ishibashi F, Okino M, Ishibashi M, Kawasaki A, Endo N, Kosaka A, et al. Corneal nerve fiber pathology in Japanese type 1 diabetic patients and its correlation with antecedent glycemic control and blood pressure. J Diabetes Investig 2012 Mar;3(2):191-198. Available from: http://dx.doi.org/10.1111/j.2040-1124.2011.00157.x PubMed PMID: 24843565. doi: 10.1111/j.2040-1124.2011.00157.x.

23. Pritchard N, Edwards K, Vagenas D, Russell AW, Malik RA, Efron N. Corneal sensitivity is related to established measures of diabetic peripheral neuropathy. Clin Exp Optom 2012 Apr;95(3):355-361. Available from: https://www.nlm.nih.gov/medlineplus/diabeticnerveproblems.html PubMed PMID: 22489841. doi: 10.1111/j.1444-0938.2012.00729.x.

24. Tavakoli M, Kallinikos P, Iqbal A, Herbert A, Fadavi H, Efron N, et al. Corneal confocal microscopy detects improvement in corneal nerve morphology with an improvement in risk factors for diabetic neuropathy. Diabetic Medicine Volume 28, Issue 2011;28(10):1261-1267. Available from: http://europepmc.org/abstract/MED/21699561 PubMed PMID: 21699561. doi: 10.1111/j.1464-5491.2011.03372.x.

25. Tavakoli M, Petropoulos IN, Malik RA. Assessing corneal nerve structure and function in diabetic neuropathy. Clin Exp Optom 2012;95(3):338-347. Available from: http://ClinicalTrials.gov/search/term=22594548%20%5BPUBMED-IDS%5D PubMed PMID: 22594548. doi: 10.1111/j.1444-0938.2012.00743.x.

26. Dabbah MA, Graham J, Petropoulos I, Tavakoli M, Malik RA. Dual-model automatic detection of nerve-fibres in corneal confocal microscopy images.. Med Image Comput Comput Assist Interv 2010;13(Pt 1):300-307. Available from: http://europepmc.org/abstract/MED/20879244 PubMed PMID: 20879244.

27. Dabbah MA, Graham J, Petropoulos IN, Tavakoli M, Malik RA. Automatic analysis of diabetic peripheral neuropathy using multi-scale quantitative morphology of nerve fibres in corneal confocal microscopy imaging. Med Image Anal 2011;15(5):738-747. Available from: http://www.scholaruniverse.com/ncbi-linkout?id=21719344 PubMed PMID: 21719344. doi: 10.1016/j.media.2011.05.016.

28. Shtein RM, Callaghan BC. Corneal confocal microscopy as a measure of diabetic neuropathy.. Diabetes 2013;62(1):25-26. Available from: http://diabetes.diabetesjournals.org/cgi/pmidlookup?view=long&pmid=23258907 PubMed PMID: 23258907. doi: 10.2337/db12-1114.

A theoretical investigation of the increase in venous oxygen saturation levels in advanced glaucoma patients

Lucia Carichino[1], Alon Harris[2], Giovanna Guidoboni[1,2,3], Brent A. Siesky[2], Luis Abegão Pinto[7], Evelien Vandewalle[5], Olof B. Olafsdottir[4], Sveinn H. Hardarson[4], Karel Van Keer[5], Ingeborg Stalmans[5,6], Einar Stefánsson[4], Julia C. Arciero[1]

[1]*Department of Mathematical Sciences, Indiana University - Purdue University Indianapolis, Indianapolis, IN, USA;* [2]*Department of Ophthalmology, Indiana University School of Medicine, Indianapolis, IN, USA;* [3]*LABEX Institut de Recherche en Mathématiques, Interactions et Applications, Strasbourg, France;* [4]*Department of Ophthalmology, University of Iceland, Reykjavik, Iceland;* [5]*Department of Ophthalmology, University Hospitals Leuven, Leuven, Belgium;* [6]*Department of Ophthalmology Neurosciences, Laboratory of Ophthalmology, Katholieke Universiteit Leuven, Leuven, Belgium;* [7]*Department of Ophthalmology, Centro Hospitalar Lisboa Norte, Lisbon, Portugal*

Abstract

Purpose: Vascular changes have been observed among glaucoma patients, but it is not yet known whether these vascular changes occur primary or secondary to glaucomatous damage. In this study, a theoretical mathematical model of the retinal vasculature is applied to a set of oximetry data obtained from healthy individuals and glaucoma patients and is used to propose possible explanations for the clinically observed increases in venous blood oxygen saturation in advanced glaucoma patients.
Methods: Given clinical measurements of intraocular pressure (IOP), mean arterial pressure and arterial blood oxygen saturation from healthy persons and advanced (visual field mean defect (MD) ≥ 10 dB) primary open angle glaucoma (POAG, IOP > 21 mmHg) patients and advanced normal tension glaucoma (NTG, IOP ≤ 21 mmHg)

Correspondence: Julia C. Arciero, Department of Mathematical Sciences, 402 N. Blackford St., LD 270 D Indianapolis, IN 46202-3267, USA.
E-mail:jarciero@math.iupui.edu.

patients, the model is used to predict the oxygen demand or Krogh cylinder tissue width that would yield the clinically-measured venous oxygen saturation in each population.

Results: A decrease in retinal tissue oxygen demand (M_0), an impairment in blood flow autoregulation, or a decrease in Krogh cylinder tissue width (d) can independently lead to increased venous saturation. The model predicts that a decrease in M_0 or a decrease in d is more likely to yield the increased venous saturation levels observed in POAG patients, while impairing blood flow autoregulation with no change in M_0 or d is more likely to yield the increased venous saturation levels observed in NTG patients.

Conclusions: The combined theoretical and clinical model predictions suggest that the mechanisms leading to increased venous saturation might differ between POAG and NTG patients. The model predictions are used to hypothesize that a decrease in oxygen demand might be more relevant to the increase in venous saturation observed in advanced POAG, while impairment in autoregulation mechanisms might be more relevant to the increase in venous saturation observed in advanced NTG.

Keywords: blood flow autoregulation, glaucoma, mathematical model, oximetry, oxygen saturation, oxygen consumption, retina, spectrophotometry

1. Introduction

Glaucoma is a progressive optic neuropathy associated with visual field loss and retinal ganglion cell death. Although glaucoma progression has been primarily associated with elevated levels of intraocular pressure (IOP), recent studies have suggested that metabolic alterations, dysfunctions of vascular autoregulation and changes in oxygen supply to tissue are also relevant factors to be considered in the progression of the disease.[1,2] The correlations between retinal metabolic alterations and vision loss are not yet fully understood; however, alterations in the retinal blood oxygen saturation levels of glaucomatous patients have been observed.[3-6] Also, blood flow deficiencies reported in retinal and retrobulbar vessels[7-11] of glaucoma patients support the hypothesis that hemodynamic alterations are correlated to glaucoma damage, independent of or related to IOP.[12,13] Alterations in the micro-vascular network density (and thus oxygen supply to tissue) in the optic disc and temporal areas have also been reported in glaucoma patients when compared with healthy individuals.[14-16]

Despite this evidence linking blood flow alterations with glaucoma, it is still unknown whether vascular changes occur primary or secondary to retinal ganglion cell loss. If primary, impaired autoregulation or insufficient blood supply to the retina and optic nerve would lead to tissue damage with subsequent vision loss. If secondary, vascular changes would be the result of optic nerve damage and the

loss of retinal ganglion cells, since those cells would no longer require oxygen or nutrient.

Several techniques can be used to measure vascular alterations in the eye, including fluorescein angiography, color Doppler imaging, laser Doppler flowmetry, Doppler optical coherence tomography and retinal oximetry.[2,17,18] In particular, retinal oximetry can be used to measure hemoglobin oxygen saturation and vessel diameters in the retina.[4,6,19-22] While many oximetry studies[4,6,19-22] have been conducted among healthy individuals and patients with various types and severity of glaucoma, trends in the oximetry measurements were not consistent across studies. For example, some studies[6,19] found no differences in venous oxygen saturation levels of normal-tension glaucoma (NTG) and high-tension primary open-angle glaucoma (POAG) patients when compared with the levels in healthy individuals, while other studies[4,20-22] found significant differences in venous oxygen saturation among these populations.

In three studies,[3,4,20] patients with advanced glaucoma (visual field mean defect (MD) ≥ 10 dB) exhibited higher venous oxygen saturation levels (and thus a lower arteriovenous difference in oxygen saturation) compared with healthy individuals and mild glaucoma patients (MD ≤ 5 dB). These observations led to the hypothesis that the decreased arteriovenous difference in the advanced glaucoma group could be due to a decrease in retinal oxygen consumption, but additional and preferably longitudinal studies in glaucoma patients are necessary to help to distinguish if the observed vascular changes occur primary or secondary to glaucoma damage.

As evident from the inconsistent trends in reported clinical data, additional methods are needed before definitive conclusions can be made relating blood oxygen saturation changes and the severity or type of glaucoma. This study applies a previously developed theoretical model of retinal vascular wall mechanics[23] to a set of clinical oximetry data obtained from healthy individuals and glaucoma patients[4] to propose possible explanations for the increases in venous oxygen saturation observed in advanced glaucoma patients. The combined mathematical and clinical approach is used to calculate theoretical changes in blood oxygen saturation in retinal arterioles, capillaries and venules and to compute patient-specific levels of tissue oxygen demand or Krogh tissue width (herein referred to as "tissue width") that would yield the measured values of venous oxygen saturation given values of mean arterial pressure (MAP = (2*DBP+SBP)/3, where DBP is diastolic blood pressure and SBP is systolic blood pressure), IOP and arterial oxygen saturation from patients. The resulting theoretical predictions provide a wider range of possible factors that could explain clinical observations than would be intuitive, and these results offer an important step in distinguishing between the primary causes and secondary effects of glaucoma.

2. Methods

2.1 Experimental data

Retinal oximetry is a clinical technique used to assess oxygen saturation levels and vessel caliber in individuals with various ocular diseases. This study focuses on oximetry data in patients with different types and degrees of severity of glaucoma. The methods of performing retinal oximetry and obtaining baseline measurements of factors such as IOP and blood pressure in glaucoma patients and healthy individuals has previously been described in detail.[4] In short, measurements from 89 healthy individuals and 74 glaucoma patients of age 40 years or older were collected. Individuals with systemic diseases or ocular diseases other than open angle glaucoma were excluded from the study. However, patients receiving antihypertensive medication for elevated systemic blood pressure and patients with mild cataracts were not excluded.

Glaucoma was defined based on the characteristic optic disc damage and the corresponding visual field defects. Of all of the glaucoma patients considered in this study, 45 were diagnosed with POAG and 29 were diagnosed with NTG. A diagnosis of POAG was defined by an untreated IOP > 21 mmHg. Patients with IOP measurements consistently ≤ 21 mmHg were classified as having NTG. All glaucoma patients underwent automated perimetry. A patient was defined as having "mild glaucoma" if the visual field mean defect (MD) was ≤ 5 dB and was defined as having "advanced glaucoma" if the visual field MD ≥ 10 dB. Of the 45 POAG patients, 20 were diagnosed with mild glaucoma and 12 were diagnosed with advanced glaucoma. Of the 29 NTG patients, 13 were diagnosed with mild glaucoma and 9 were diagnosed with advanced glaucoma. Some patients were under active treatment at the time of measurement.

All oximetry measurements were performed in darkness with the Oxymap T1 oximeter (Oxymapehf, Reykjavik, Iceland), where relative oxygen saturation was measured semi-automatically with the Oxymap Analyzer Software 2.2.1 (v.3847). The IOP measurements were performed on dilated pupils using a Goldmann applanation tonometry mounted on a Haag-Streit slit lamp (Haag-Streit BQ 900, Haag-Streit International, Köniz, Switzerland) in Belgium, and using the iCare TAO1 tonometer (Tiolat Oy, Helsinki, Finland) in Iceland. An automatic sphygmomanometer was used to obtain all measurements of systolic and diastolic blood pressures after a 5 min resting period (in Belgium: Omron HEM-7001-E, Omron, Kyoto, Japan; in Iceland: Omron HEM-7221-E, Omron, Kyoto, Japan).

2.2 Mathematical model

To determine possible explanations for measured changes in venous oxygen saturation in POAG and NTG patients,[4] a simplified mathematical model of the retinal vasculature, previously developed by Arciero et al.,[23] is used. The retinal vasculature downstream of the central retinal artery (CRA) and upstream of the central retinal
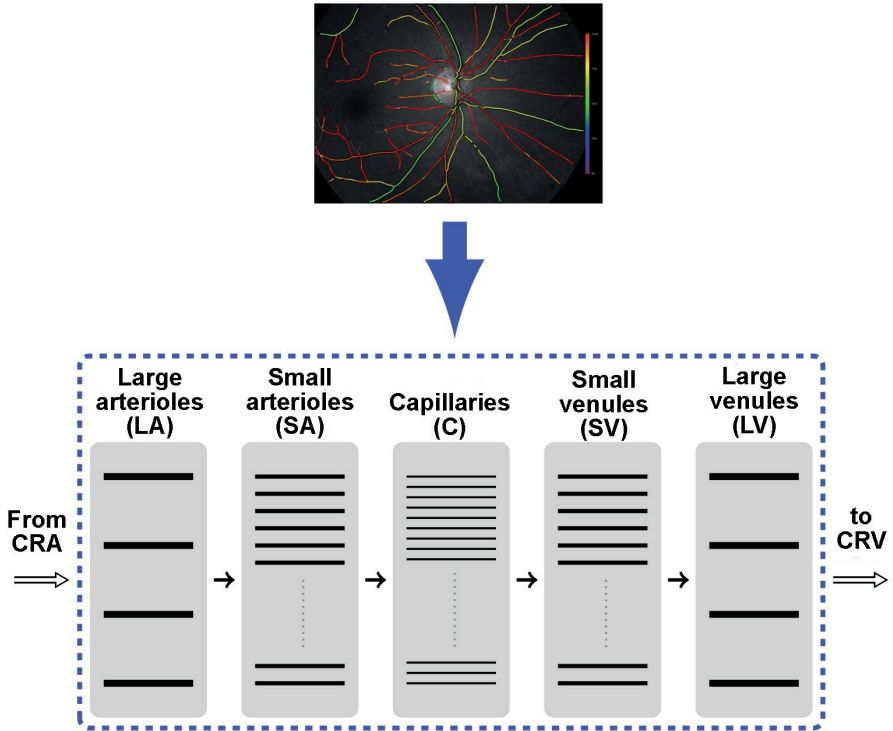
Fig. 1. The retinal vasculature, as depicted in the oximetry image (top), is modeled as a representative segment network (bottom) consisting of five compartments of parallel-arranged vessels connected in series downstream of the central retinal artery (CRA) and upstream of the central retinal vein (CRV): Large arterioles/arteries (LA), small arterioles (SA), capillaries (C), small venules (SV) and large venules/veins (LV).

vein (CRV) is modeled as a representative segment network, where five vessel compartments for the large arterioles (LA), small arterioles (SA), capillaries (C), small venules (SV) and large venules (LV) supplying and draining the retina are connected in series; each compartment consists of identical segments arranged in parallel (Fig. 1). All compartments are assumed to experience the same hemodynamic and metabolic conditions. A summary of the model equations, along with its input values and output values, is provided in Table 1. The subscripts used in Table 1 indicate if the quantity is evaluated either at the inlet (*in,i*), midpoint (*mp,i*) or outlet (*out,i*) of the *i*th compartment, where *i*=LA,SA,C,SV,LV. The values of the model parameters are listed in Tables 2, 3 and 4. In the following, the main features of the model are discussed, which are leveraged to perform the simulations reported in the Results section. For a complete description of the model we refer to a previous study by Arciero *et al.*[23]

Table 1. Summary of model[23] variables and equations (sections b – f), including input (section a) and output (section g) data.

Input
(a) $P_{in,LA} = \frac{2}{3}MAP - 20\text{mmHg}, \quad P_{out,LV} = IOP, \quad S(x = 0) = \text{arterial oxygen saturation},$
$M_0, \quad d, \quad bCO_2(x = 0) = 50\%, \quad C(x = 0) = 0.5\mu M$

Equations

(b)
$$\begin{cases} \dfrac{dD_i}{dt} = \dfrac{2\lambda_i}{\tau_d}\left(T_i - T_{total,i}\right) \\ \dfrac{dA_i}{dt} = \dfrac{1}{\tau_a}\left(A_{total,i} - A_i\right) \end{cases} \quad i = \text{LA,SA}$$

$T_{total,i} = T_{passive,i} + A_i T_{max.active,i}$ $T_{passive,i} = C_{pass,i}\exp\left[C'_{pass,i}\left(D_i/D_{0,i} - 1\right)\right]$

$T_{max.active,i} = C_{act,i}\exp\left\{-\left[\left(D_i/D_{0,i} - C'_{act,i}\right)/C''_{act,i}\right]^2\right\}$ $A_{total,i} = 1/\left(1 + \exp(-S_{tone,i})\right)$

$S_{tone,i} = C_{myo,i}T_i - C_{shear,i}\tau_i - C_{meta,i}S_{CR,i} - C_{CO_2,i}S_{CO_2,LV} + C''_{tone,i}$

(c)	Myogenic	$T_i = (P_{mp,i} - IOP)D_i/2 \quad i = \text{LA,SA,C,SV,LV}$
		$\Delta P_{tot} = Q_{tot}R_{tot} = P_{in,LA} - P_{out,LV} \quad R_{tot} = \sum_i R_i \quad Q_{tot} = n_i Q_i$
		$\Delta P_i = Q_i R_i = P_{in,i} - P_{out,i} \quad R_i = (128\mu_i L_i)/(\pi D_i^4 n_i) \quad P_{mp,i} = P_{in,i} + \frac{1}{2}\Delta P_i$

(d)	Shear stress	$\tau_i = (32\mu_i Q_i)/(\pi D_i^3) \quad i = \text{LA,SA,C,SV,LV}$

(e)	Metabolic	$S_{CR,i} = \displaystyle\int_{x_{mp,i}}^{x_{end,i}} \exp\left[-\left(y - x_{mp,i}\right)/L_0\right]C(y)dy \quad i = \text{LA,SA}$
		$C(x) = \alpha + \beta(x - x_{in,i}) + \exp\left[\gamma(x_{in,i} - x)\right]\left(C(x_{in,i}) - \alpha\right)$
		$\alpha(x) = H_T R_0\left[D_i(1 - R_1 S(x_{in,i})) - (1 - H_D)R_0 q(x)/(\pi c_0 H_D k_d)\right]/4k_d$
		$\beta(x) = (D_i H_T R_0 R_1 q(x))/(4Q_i c_0 H_D k_d) \qquad \gamma = k_d \pi D_i/[(1 - H_D)Q_i]$
		$q(x) = M_0 \pi (r_{t,i}^2 - r_{v,i}^2) \qquad r_{v,i} = \frac{1}{2}D_i \qquad r_{t,i} = r_{v,i} + d_i$
		$S(x) = S(x_{in,i}) + q(x)(x_{in,i} - x)/(Q_i c_0 H_D)$
		$PO_2(x,r) = PO_2(x,r_{v,i}) + M_0\left[(r^2 - r_{v,i}^2)/4 + r_{t,i}^2 \ln(r_{v,i}/r)/2\right]/k$

(f)	Carbon dioxide	$S_{CO_2,LV} = f(PCO_{2LV}, Q_{tot})$
		$PCO_{2LV} = g(tCO_2(x_{mp,LV})) \qquad tCO_2(x) = bCO_2(x)(1 - (-0.115Q_{tot} + 0.23))$
		$bCO_2(x) = bCO_2(x_{in,i}) - 0.81q(x)(x_{in,i} - x)/(Q_i c_0 H_D)$

Output
(g) $P_i, \Delta P_i, R_i$ and Q_i $i = \text{LA,SA,C,SV,LV}, \; C(x), S(x), PO_2(r,x), tCO_2(x), bCO_2(x)$

Table 2. Parameter values for passive tension, active tension, and vascular smooth muscle activation equations in the large arterioles (LA) and small arterioles (SA).

Constant	Value		Unit	Constant	Value		Unit
	LA	SA			LA	SA	
C_{pass}	361.48	197.01	$[dyn/cm]$	C_{myo}	0.0092	0.025	$[cm/dyn]$
C'_{pass}	53.69	17.60	$[1]$	C_{shear}	0.0258	0.0258	$[cm^2/dyn]$
C_{act}	2114.2	3089.6	$[dyn/cm]$	C_{meta}	200	200	$[\mu M/cm]$
C'_{act}	0.93	1.02	$[1]$	C_{co_2}	8e^{-4}	1.31e^{-4}	$[1/mmHg]$
C''_{act}	0.11	0.20	$[1]$	C''_{tone}	159.26	62.27	$[1]$
λ	0.0457	0.0604	$[1/mmHg]$	D_0	135.59	73.9	$[\mu M]$

Table 3. Time constants for the model equations (Table 1(b)) and parameter values for the metabolic response (Table 1(e)).

Parameter	Value	Unit
time constant for diameter, τ_d	1	$[s]$
time constant for activation, τ_a	60	$[s]$
tube hematocrit, H_T	0.3	$[1]$
discharge hematocrit, H_D	0.4	$[1]$
rate of ATP degradation, k_d	2e^{-4}	$[cm/s]$
maximum rate of ATP release, R_o	1.4e^{-9}	$[mol\ s^{-1}\ cm^{-3}]$
effect of oxygen saturation on ATP release, R_1	0.891	$[1]$
oxygen capacity of red blood cells, c_0	0.5	$[cm^3\ O_2/cm^3]$
oxygen tissue diffusion coefficient, k	9.4	$[cm^3\ O_2\ cm^{-1}\ mmHg^{-1}\ s^{-1}]$
length constant for S_{cr}, L_0	1	$[cm]$

Table 4. Parameter values describing vessel network geometry and viscosity.

Parameter	Value					Unit
	LA	SA	C	SV	LV	
number of segments, n	4	39	111,360	39	4	$[1]$
segment length, L	0.807	0.583	0.088	0.583	0.807	$[cm]$
viscosity, μ	2.28	2.06	10.01	2.09	2.44	$[cP]$

Blood flow and oxygen saturation throughout the network are predicted according to hemodynamic and mechanical principles. Retinal flow is assumed to follow Poiseuille's Law, in which flow through each vessel is proportional to the fourth power of the vessel diameter. The complex blood rheology is accounted for by assigning different values of the apparent viscosity μ to vessels in each compartment according to an experimental *in vivo* relationship[24] (Table 4). The total tension $T_{total,i}$ generated in the vessel walls of the vasoactive compartments $i=$ LA, SA follows the Law of Laplace and is modeled as the sum of passive and active tension, denoted by $T_{passive,i}$ and $T_{max.active,i}$, respectively, as detailed in Table 1(b). $T_{passive,i}$ results from the structural components of the vessel wall, and $T_{max.active,i}$ is generated by the contraction and dilation of smooth muscles in the LA and SA. Smooth muscle tone in LA and SA is described by the activation function $A_{total,i}$, which ranges from 0 to 1. The product of $T_{max.active,i}$ and the activation A_i yields the active tension generated in the vessel wall. Changes in $A_{total,i}$ are dictated by the stimulus function $S_{tone,i}$ which results from a linear combination of four autoregulatory mechanisms:

1. *myogenic mechanism*, related to the wall tension T_i computed via the Law of Laplace. Details are provided in Table 1(c), where ΔP_{tot} represents the total pressure drop along the retinal network from the outlet of the CRA to the inlet of the CRV, and ΔP_i represents the pressure drop along each segment of the ith compartment. Similarly, Q_{tot} represents the total blood flow along the network and Q_i represents the blood flow in each segment of the ith compartment, and R_{tot} represents the resistance to flow offered by the whole retinal network and R_i represents the resistance to flow offered by a single segment of the ith compartment. The resistances R_i are computed according to Poiseuille's Law;

2. *shear stress mechanism*, related to the wall shear stress τ_i computed according to Poiseuille's Law. Details are provided in Table 1(d);

3. *metabolic mechanisms*, related to the signal $S_{CR,i}$. Details are provided in Table 1(e), where the signal $S_{CR,i}$ depends on the ATP concentration at each position x along the network $C(x)$, which itself depends on the blood oxygen saturation at each point in the network $S(x)$;

4. *carbon dioxide mechanism*, related to the signal $S_{CO_2,LV}$. Details are provided in Table 1(f), where the signal $S_{CO_2,LV}$ is given by the nonlinear function f of the partial pressure of carbon dioxide in the tissue (PCO_2) and of the total retinal blood flow (Q_{tot}). The tissue carbon dioxide content (tCO_2) is converted into PCO_2 via carbon dioxide dissociation curves, represented by the function g. The tissue carbon dioxide content and the blood carbon dioxide content (bCO_2) are assumed to be linearly related.[25]

The vasodilatory effect of nitric oxygen and the vasoconstrictor effect of endothelin-1 released by endothelial cells[1] is not modeled explicitly. The roles of

these endothelial drivers for autoregulation has been established in the anterior optic nerve region,[26,27] but less is known about their roles in the retinal microcirculation and thus these factors are neglected here.

Arciero *et al.*[23] showed that the metabolic and carbon dioxide responses contribute most significantly to blood flow autoregulation, leading to a nearly constant blood flow over a wide range of intraluminal pressures. In the model, autoregulation is achieved through changes in the diameters D_i of the LA and SA segments, which should be interpreted as the new equilibrium state attained by the system as the input data are altered. In this study, simulations are also performed in the case of impaired autoregulation corresponding to the case in which metabolic and carbon dioxide mechanisms are switched off.

Since the present study aims to compare model-predicted and clinically measured venous saturation levels, details for the oxygen saturation model calculations are provided. Other details of flow, diameter and smooth muscle activation calculations are given previously[23] and are outlined here in Table 1.

By the conservation of mass, the change in oxygen flux must equal the rate of oxygen consumed by the retinal tissue:

$$\frac{d}{dx}[Q_i c_0 H_D S(x)] = -q(x) \tag{1}$$

where x is the distance along the network, Q_i is the blood flow in each compartment
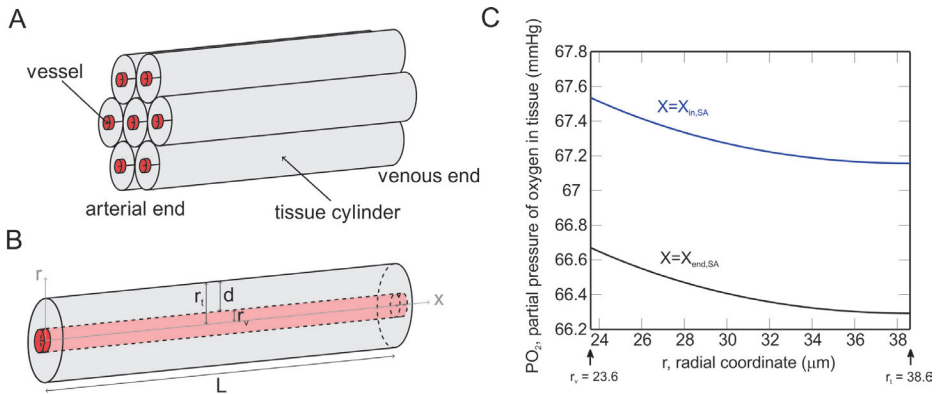

Fig. 2. A Krogh cylinder model is used to predict oxygen diffusion in retinal tissue. A) Representation of a Krogh cylinder model in which vessels (red) run along the center axis of a tissue cylinder (gray). B) Depiction of a single vessel (red) supplying a cylindrical region of tissue (gray) with oxygen, where r is the radial coordinate, x is the distance along the network, r_t is the radius of the tissue region, r_v is the radius of the vessel, d is the tissue width and L is the vessel length. C) Distribution of the partial pressure of oxygen $PO_2(x,r)$ in the tissue surrounding the small arterioles in the radial direction at two fixed positions $x_{in,SA} = 0.81$ cm and $x_{end,SA} = 1.39$ cm, $PO_2(x_{in,SA}, r_v) = 67.53$ mmHg, $PO_2(x_{end,SA}, r_v) = 67.67$ mmHg, $M_0 = 1.65$ cm³ $O_2 \cdot 100$ cm⁻³ min⁻¹, $r_v = 23.6$ μm , $r_t = 38.6$ μm, $k = 9.4$ cm³ O_2 cm⁻¹ mmHg⁻¹ s⁻¹.

i, c_0 is the oxygen carrying capacity of red blood cells at 100% saturation, H_D is the discharge hematocrit, $S(x)$ is the blood oxygen saturation and q is the tissue oxygen consumption per vessel length. Since the clinical data set in this study does not include patient-specific hematocrit values, H_D is assumed to be constant, as specified in Table 3.

Oxygen consumption in the tissue is calculated using a Krogh cylinder model, in which each oxygen-delivering vessel is assumed to provide oxygen via diffusion to a cylindrical region of tissue surrounding it (see Fig. 2A). In the present model, oxygen is assumed to be delivered by the large and small arterioles and capillaries; no oxygen exchange is assumed in the venules. At each position x in the retinal vascular network, the oxygen is delivered to the nearest tissue via diffusion according to:

$$k\left[\frac{1}{r}\frac{d}{dr}\left(r\frac{dPO_2\,(x,r)}{dr}\right)\right]=M_0 \tag{2}$$

where k is the diffusion coefficient, PO_2 is the partial pressure of oxygen at a radial distance r within the tissue cylinder and M_0 is the tissue oxygen demand per tissue volume (assumed here to be constant). The degeneration of the retinal ganglion cells is modeled indirectly by varying the tissue oxygen demand M_0; retinal ganglion cells degeneration would correspond to a decrease in M_0. Given the architecture of this model, it is important to note that the M_0 defined here is primarily representative of the oxygen demand of the retinal ganglion cells in the inner retina.[28]

The partial pressure of oxygen in the tissue along the radial direction r for a fixed position in the network x is given by:

$$PO_2(x,r)=PO_2\,(x,r_{v,i})+\frac{M_0}{k}\left[\frac{r^2-r_{v,i}^2}{4}+\frac{r_{t,i}^2}{2}\,\ln\!\left(\frac{r_{v,i}}{r}\right)\right] \tag{3}$$

where the subscript i indicates the vessel compartment, $r_{t,i}$ denotes the radius of the tissue region and $r_{v,i}$ denotes the vessel radius, as depicted in Fig. 2B. Fig. 2C depicts a sample solution for two positions $x_{in,SA}=0.81$ cm (blue curve) and $x_{end,SA}=1.39$ cm (black curve) in the small arterioles for $PO_2(x_{in,SA},r_v)=67.53$ mmHg, $PO_2(x_{end,SA},r_v)=66.67$ mmHg, $M_0=1.65$ cm³ $O_2\cdot100$ cm⁻³ min⁻¹, $k=9.4$ cm³ O_2 cm⁻¹ mmHg⁻¹ s⁻¹, $r_v=23.6$ μm, and $r_t=38.6$ μm.

For a constant value of M_0, the tissue oxygen consumption per vessel length (q) is computed as:

$$q(x)=\int_{r_{v,i}}^{r_{t,i}}M_0\,2\pi r\,dr=\pi\,M_0\left(r_{t,i}^2-r_{v,i}^2\right) \tag{4}$$

The width of tissue surrounding each vessel is defined as $d_i=r_{t,i}-r_{v,i}$. Here, it is assumed that d_i is equal to the same value d for each oxygen-delivering vessel $i=$ LA, SA, C and that $d_i=0$ for the SV and LV compartments. Thus, the oxygen consumption rate q depends on both the tissue volume surrounding the vessel and on the level of functional activity of the retinal ganglion cells represented by the tissue oxygen

demand (M_0). In turn, changes in the oxygen consumption rate q will induce changes in the oxygen saturation within the vessel as dictated by the balance of mass in Equation (1).

Given the model inputs listed in Table 1 section (a), the steady-state values of the diameters D_i and of the vascular smooth muscle activations A_i in the LA and SA compartments are determined by integrating the system of ordinary differential equation in Table 1(b) until equilibrium is reached. It is important to note that the system also involves the quantities T_i, $T_{total,i}$ and $A_{total,i}$ which, as detailed in Table 1, are functions of the unknowns D_i and A_i. The use of a steady state model is justified since the variation in the clinical measurements of oxygen saturation due to the cardiac cycle is not large.[29]

2.3 Model reference state

A reference state is defined to represent conditions typical of a healthy retina. For example, the reference state values of IOP, MAP and arterial and venous oxygen saturation are set equal to the average values of these factors measured in all of the healthy individuals in this study (see Table 5). The reference state value of tissue width is chosen to be $d^{ref} = 15$ μm, which corresponds to an experimental measurement of retinal intercapillary space of 30 μm.[30] In the reference state, the proportion of the tissue occupied by capillary lumens is about 2.7%, which is in good agreement with the proportion of 2.5% measured in histological specimens.[31] Given the reference

Table 5. Clinical average values of intraocular pressure (IOP, in mmHg), mean arterial pressure (MAP, in mmHg), ocular perfusion pressure (OPP = $\frac{2}{3}$ MAP – IOP, in mmHg), retinal arterial oxygen saturation and retinal venous oxygen saturation measured in healthy individuals, advanced (visual field MD ≥ 10 dB) primary open-angle glaucoma (POAG, IOP > 21 mmHg) patients and advanced normal tension glaucoma (NTG, IOP ≤ 21 mmHg) patients [4]. Reference state parameter values are highlighted in bold.

		Healthy (n=85)	Advanced POAG (n=12)	Advanced NTG (n=8)
Clinical data	IOP [mmHg]	**15 ± 3**	15 ± 3	10 ± 3
	MAP [mmHg]	**102 ± 12**	99 ± 10	109 ± 11
	OPP [mmHg]	**53 ± 8**	51 ± 8	62 ± 6
	Arterial oxygen saturation [%]	**93 ± 4**	95 ± 2	94 ± 3
	Venous oxygen saturation [%]	**54 ± 6**	58 ± 5	58 ± 6
Reference values	M_0^{ref} [$cm^3O_2 \cdot 100\ cm^{-3}min^{-1}$]	**1.65**		
	d^{ref} [μm]	**15**		

values of IOP, MAP, tissue width, and arterial oxygen saturation, the model is used to calculate the value of tissue oxygen demand (M_0^{ref} = 1.65 cm^3 O$_2$·100 cm^{-3} min^{-1}) that will yield the reference venous oxygen saturation level of 54%, as measured in healthy patients. This calculated rate of oxygen demand in the reference state is close in magnitude to oxygen demand levels observed experimentally.[32-34]

2.4 Model simulations

The mathematical model presented in this study is used to conduct the following simulations:

1. *Theoretical investigation*
   The model is used to predict the theoretical effect of the artificial variation of the model inputs (Table 1(a)) on the computed outputs (Table 1(g)).
2. *Theoretical interpretation of clinical data*
   The model is used to estimate patient-specific values of oxygen demand (simulation 2A) or tissue depth (simulation 2B) that would yield the clinically-measured value of venous oxygen saturation when patient-specific inputs are considered.

The details of the algorithms implemented to perform these novel, patient-specific simulations are provided below.

Algorithm for simulation 2A:
For any individual included in the experimental study proceed as follows:
   i.   Set the patient-specific input values for $P_{in,LA}$, $P_{out,LV}$ and $S(x=0)$ (Table 1(a)) given the clinical measurements of MAP, IOP and arterial oxygen saturation;
   ii. set the input tissue depth equal to the reference state value d^{ref} (Table 1(a));
   iii. set the initial guess for the input oxygen demand to M_0^0 (Table 1(a)), then for $k{\geq}0$
      a. solve the model described in Table 1(b)-(f);
      b. compute the output of the model (Table 1(g)), which includes oxygen saturation $S^k(x)$;
      c. test for convergence:

      if $\dfrac{|\text{measured} - \text{predicted venous oxygen saturation}|}{|\text{measured venous oxygen saturation}|} \leq 5 \cdot 10^{-2}$, set $M_0 = M_k^0$,

      otherwise set $M_0^{(k+1)} = M_0^k + \delta_M$ and return to point a).

Algorithm for simulation 2B:
For any individual included in the experimental study proceed as follow:

i.   set the patient-specific input values for $P_{in,LA}$, $P_{out,LV}$ and $S(x=0)$ (Table 1(a)) given the clinical measurements of MAP, IOP and arterial oxygen saturation;

ii. set the input oxygen demand equal to the reference state value M_0^{ref} (Table 1(a));

iii. set the initial guess for the input tissue depth to d^0 (Table 1(a)), then for $k \geq 0$

    a.   solve the model described in sections Table 1(b)-(f);

    b.   compute the output of the model (Table 1(g)), which includes oxygen saturation $S^k(x)$;

    c.   test for convergence:

$$\text{if } \frac{|\text{measured} - \text{predicted venous oxygen saturation}|}{|\text{measured venous oxygen saturation}|} \leq 5 \cdot 10^{-2}, \text{set } d = d^k,$$

otherwise set $d^{k+1} = d^k + \delta_d$ and return to point a).

In step iii(c) of simulations (2A) and (2B), the values of δ_M and δ_d are determined via the MATLAB algorithm fsolve, which is a nonlinear least-squares algorithm. For each of the algorithms (2A) and (2B), two sets of simulations are performed corresponding to the cases of functional or impaired autoregulation.

3. Results

3.1 Experimental data

Fig. 3 shows the scatter plot of the venous saturation data collected from healthy individuals, advanced POAG patients and advanced NTG patients.[4] Four healthy individuals and one advanced NTG patient were excluded since no record of MAP measurement was reported. Data for mild glaucoma patients are not included in the figure since Olafsdottir and Vandewalle *et al.*[4] found no statistical difference in retinal oxygen arterial and venous saturation between healthy individuals and mild glaucoma patients. The black bars represent the average value of each group and the corresponding standard deviation. In both the advanced POAG and advanced NTG patient groups, the average value of venous oxygen saturation is higher than in healthy individuals, and the average value of arteriovenous difference is lower than in healthy individuals. No statistical difference was reported in retinal oxygen saturation when mild POAG and mild NTG patients were compared, nor when advanced POAG and advanced NTG patients were compared. The average values of IOP, MAP and oxygen saturation measured in healthy individuals, advanced POAG patients and advanced NTG patients are also reported in Table 5.

3.2 Theoretical investigation

Fig. 4 shows the scatter plot of the venous oxygen saturation data collected from healthy individuals as a function of ocular perfusion pressure ($OPP = \frac{2}{3} MAP\text{-}IOP$). The
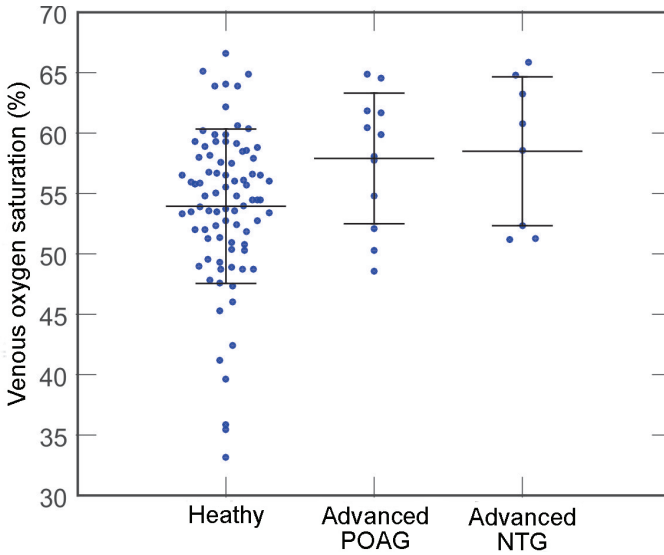
Fig. 3. Venous oxygen saturation clinical data collected from healthy individuals (n=85), advanced POAG patients (n=12) and advanced NTG patients (n=8)[4] (blue dots). Black bars represent the mean and standard deviation of each group.
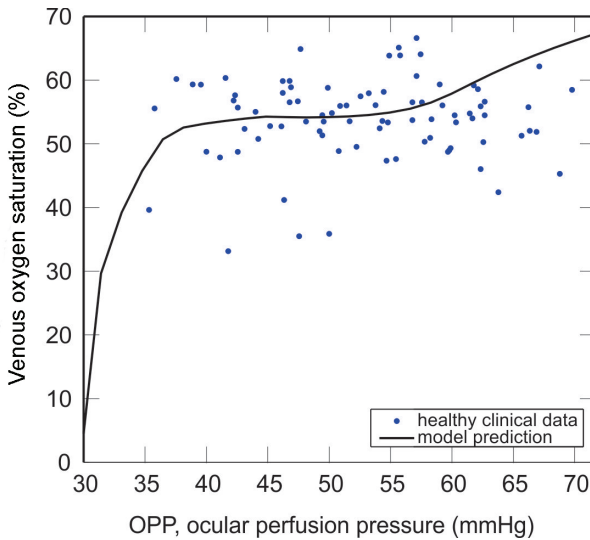

Fig. 4. A scatter plot of the venous saturation clinical data (blue dots) collected from healthy individuals is compared with theoretical predictions (solid black curve) as OPP is varied. Here, a range of OPP values is generated by holding IOP constant at its reference state value (15 mmHg) while varying MAP between 67 and 130 mmHg.

clinical data (blue dots) are compared to the mathematical model prediction (solid curve) of venous saturation as OPP is varied. Reference state values of IOP, MAP, arterial oxygen saturation, M_0^{ref} and d^{ref} are used to produce the model simulated curve. Since the model predictions generated by varying MAP and holding IOP constant or by varying IOP and holding MAP constant are nearly identical, only one curve is shown as OPP is varied.

Since the clinical data[4] show an increase in venous saturation in advanced glaucoma patients, the mathematical model is used to theorize three possible explanations for increased venous saturation:

1. **A decrease in tissue oxygen demand (M_0):** If less oxygen is consumed by the tissue, higher levels of venous oxygen saturation are predicted;
2. **An impairment of blood flow autoregulation:** If the most influential autoregulation mechanisms (conducted metabolic and/or local carbon dioxide response mechanisms) are impaired, higher levels of venous oxygen saturation are predicted for certain ranges of OPP;
3. **A decrease in tissue width (d):** If the volume of tissue supplied by each capillary or arteriole is decreased, higher levels of venous oxygen saturation are predicted.

As shown in Fig. 5A, the model predicts a decrease in venous oxygen saturation as oxygen demand is increased provided that all other factors (MAP, IOP, d, arterial blood saturation and functionality of autoregulation) are not altered. Fig. 5B depicts case (1) in which venous oxygen saturation is shown as a function of OPP for two different values of M_0: $M_0^{ref} = 1.65$ cm^3 O$_2$·100 cm^{-3} min^{-1}(blue curve) and $M_0 = 1.32$ cm^3 O$_2$·100 cm^{-3} min^{-1} (red curve). These curves show the effect of a 20% decrease in oxygen demand on the model predictions of venous saturation. It is interesting to observe that this decrease in oxygen demand causes variable increases in venous oxygen saturation depending on the value of OPP.

Fig. 5C provides evidence for case (2), namely that an increase in venous oxygen saturation can also occur over a certain range of OPP values when autoregulation is impaired. In this case, $M_0^{ref} = 1.65$ cm^3 O$_2$·100 cm^{-3} min^{-1} for both curves, but the metabolic and carbon dioxide autoregulation mechanisms are impaired (*i.e.,* absent) in the black dashed curve.

Fig. 5D shows that a decrease in tissue width supplied by each arteriole or capillary in the Krogh cylinder model can also lead to an increase in venous oxygen saturation, as outlined in case (3). Decreasing the tissue width leads to a decrease in the total tissue volume supplied by the retinal vasculature. Fig. 5D depicts the effect of decreasing tissue width from $d^{ref} = 15$ *μm* (blue curve) to $d = 13$ *μm* (green curve).

3.3 Theoretical interpretation of clinical data

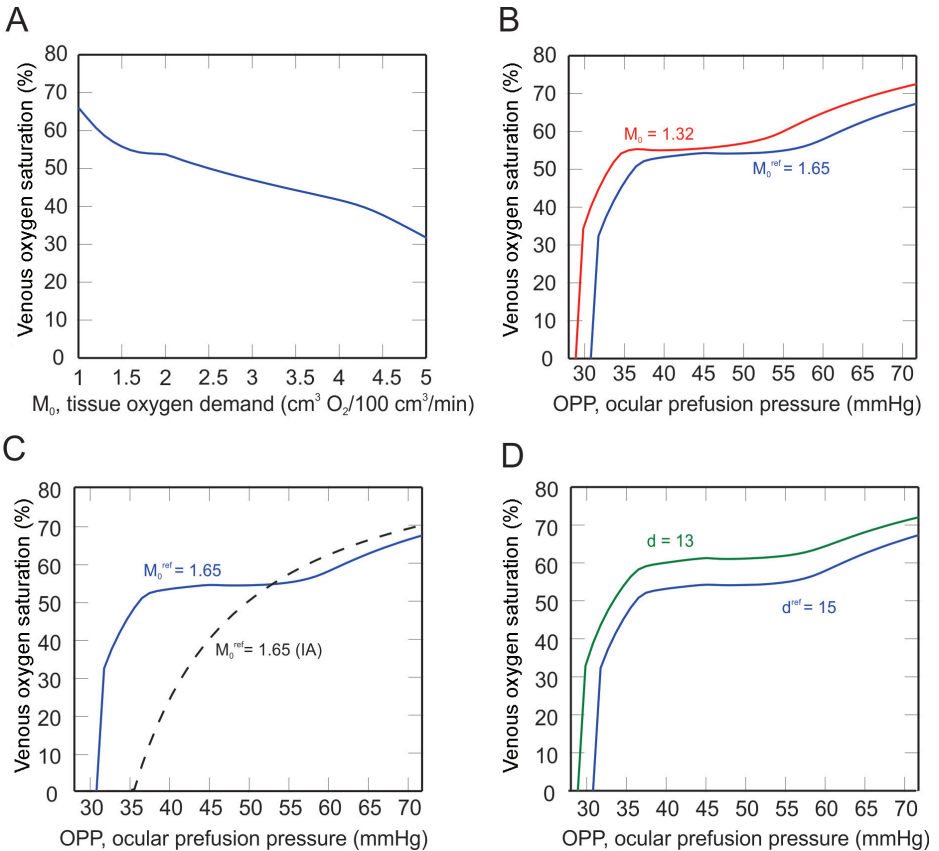Fig. 6 summarizes the model predicted values of oxygen demand (gray) or tissue

Fig. 5. A) Decrease in venous oxygen saturation as tissue oxygen demand (M_0) is increased, given constant reference state values of MAP, IOP and arterial oxygen saturation. The remaining panels highlight the three-part theoretical investigation of the effects of B) oxygen demand (M_0), C) impaired autoregulation (IA) and D) tissue width (d) on model predictions of venous oxygen saturation as OPP is varied. Each scenario is compared with the model prediction of the reference state (blue curve) in which $M_0^{ref} = 1.65$ cm³ O_2/100 cm³/min, $d^{ref} = 15$ μm, and autoregulation is functional.

width (blue) that will yield the clinically observed venous saturation levels (Fig. 3) for each individual in the healthy, advanced POAG and advanced NTG populations. Model predictions for mild POAG and NTG patient groups are not included since the venous saturation levels did not differ from healthy individuals. The model predicts that the observed increase in venous saturation in advanced POAG patients is accompanied by a decrease in oxygen demand, whereas no change in oxygen demand is predicted in advanced NTG patients. A slightly lower tissue width is predicted in POAG patients to yield increased venous saturation but not
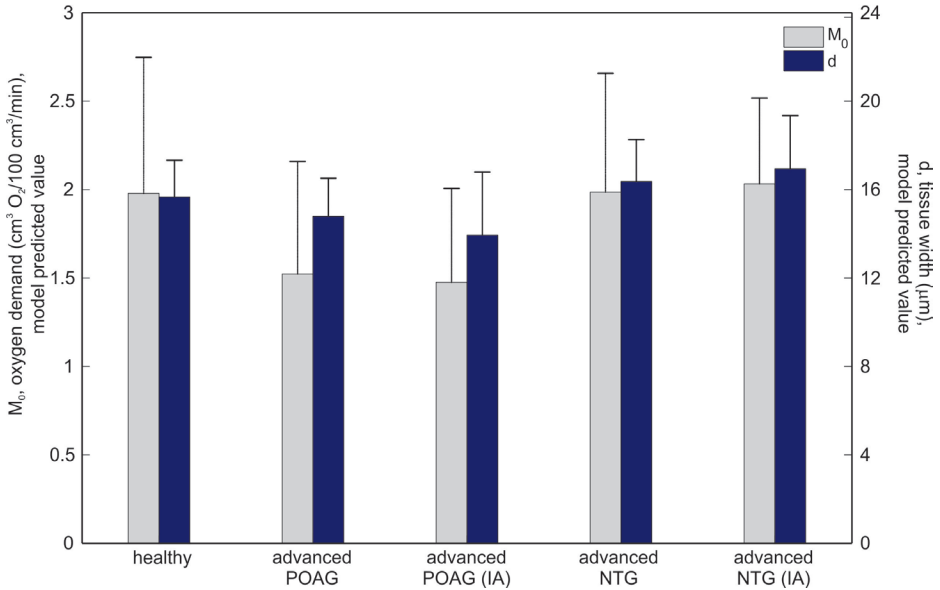
Fig. 6. Model predicted levels of tissue oxygen demand (M_0) and tissue width (d) that yield the venous saturation clinical data collected from each individual in the healthy, advanced POAG and advanced NTG populations.[4] Model predictions are also provided when autoregulation is impaired (IA) in advanced POAG and NTG patients. Black bars represent mean and standard deviation of each group.

in NTG patients. These trends are observed regardless of whether autoregulation is functioning or impaired. Table 6 lists the mean and standard deviation of the oxygen demand and tissue width model predictions depicted in Fig. 6. All clinical measures were used except for a few cases in which the tolerance of the optimization procedure employed to find M_0 (2 healthy patients, 1 advanced POAG patient and 1 advanced NTG patient) and d (2 healthy patients and 1 advanced NTG patient) was not achieved.

Table 6. Model predicted levels of tissue oxygen demand (M_0) and tissue width (d) that yield the venous saturation clinical data collected from healthy, advanced POAG and advanced NTG patients. [4]

	Healthy	Advanced POAG	Advanced POAG (IA)	Advanced NTG	Advanced NTG (IA)
M_0 [cm^3 O$_2$·100 cm^{-3} min^{-1}]	1.98 ± 0.77	1.52 ± 0.64	1.48 ± 0.53	1.99 ± 0.67	2.03 ± 0.48
d [μm]	15.66 ± 1.66	14.79 ±1.72	13.94 ± 2.85	16.36 ±1.90	16.94 ±2.40

It is important to note that the average values of oxygen demand and tissue width calculated for the healthy population (reported in Table 6) are not equal to the reference state values of oxygen demand and tissue width (reported in Table 5). In Table 5, the values M_0^{ref} and d^{ref} are computed from average values of IOP, MAP and arterial saturation obtained from the healthy population. In Table 6, the values of M_0 and d are computed using the MAP, IOP and arterial saturation from each individual and then averaging the resulting values in each population.

Based on the model predictions summarized in Fig. 6 and Table 6, Fig. 7A shows the model predicted curves of venous oxygen saturation for $M_0 = 1.98$ cm^3 O$_2 \cdot 100$ cm^{-3} min^{-1} (blue curve) and decreased $M_0 = 1.52$ cm^3 O$_2 \cdot 100$ cm^{-3} min^{-1} (black curve) as well as the average clinical values of venous saturation and OPP in healthy individuals (asterisk) and advanced POAG patients (square). In Fig. 7B, $M_0 = 1.98$ cm^3 O$_2 \cdot 100$ cm^{-3} min^{-1} and $d^{ref} = 15$ μm are fixed for both curves, but autoregulation is assumed to be impaired for the black dashed curve. These model predictions are compared with average clinical values of venous saturation and OPP measured in healthy individuals (asterisk) and advanced NTG patients (square).
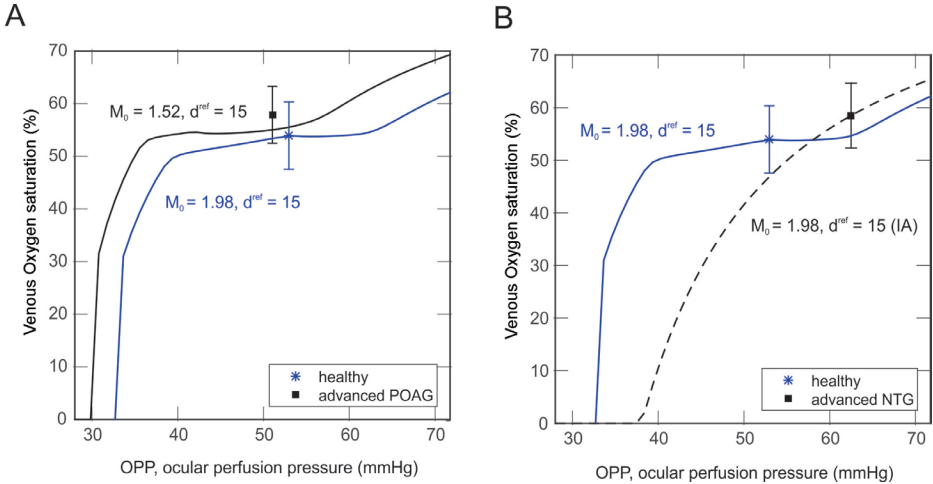

Fig. 7. Model predicted curves of venous oxygen saturation as OPP is varied are shown with average values of venous oxygen saturation and OPP measured clinically. A) The observed increase in the average venous saturation in healthy individuals (blue asterisk) and in advanced POAG patients (black square) is compared with model predicted levels of venous saturation for decreased levels of tissue demand. B) The observed increase in the average venous saturation in healthy individuals (blue asterisk) and advanced NTG patients (black square) is compared with model predicted levels of venous saturation when autoregulation is impaired (IA).

4. Discussion

4.1 Experimental data
Retinal vessel oxygen saturation was measured in healthy individuals and glaucoma patients using a non-invasive retinal oximeter. The measurements indicated that patients with advanced glaucoma (both POAG and NTG patients) exhibited higher venous oxygen saturation (and consequently a lower arteriovenous difference in oxygen saturation) compared with healthy individuals. Other studies[21,22] have confirmed these findings, and it has been previously hypothesized[4] that the observed increase in venous saturation is likely a secondary effect of glaucomatous atrophy and not a primary cause of glaucoma, citing the absence of hypoxia in advanced glaucoma patients as supporting evidence. However, the number of advanced glaucoma patients in these studies (including the current one) was rather small, and many patients were under active ophthalmological care. Thus, additional studies, ideally progressive in nature and conducted in patients with very high IOP and very low OPP, are needed in order to draw more definitive conclusions.

4.2 Theoretical investigation
This study implements a theoretical model based on fundamental hemodynamic and mechanical principles to predict venous oxygen saturation levels given patient-specific values of MAP, IOP and arterial oxygen saturation. The model predictions using the reference state values of these factors align well with the observed venous saturation levels collected from healthy individuals (Fig. 4).

A Krogh cylinder model is used to describe the diffusion of oxygen into tissue; this Krogh model is applied in the classical sense in which the oxygen-supplying vessel runs along the central axis of a tissue cylinder. However, such an assumption may not be the most appropriate for retinal tissue, since the majority of the tissue that retinal vessels feed is typically located "below" the vessels.[35] Some mathematical models have described oxygen diffusion through the retinal tissue layers[36-39] but did not consistently include a description of blood flow and autoregulation in the retinal vasculature. It would be an interesting research direction to enhance the model in the current study to include a more realistic geometric arrangement of vessels and tissue. It has also been shown that oxygen diffuses directly from the CRA to the CRV, bypassing the retinal microcirculation, due to the close anatomical relation between the central retinal vessels in the center of the optic nerve.[40,41] The current model could be extended to include the effects of this counter-current exchange phenomenon.

4.3 Theoretical interpretation of clinical data
In this study, a mathematical model is used to offer possible explanations for the observed trends in oximetry data collected in healthy individuals and glaucoma patients. Specifically, the model shows that a decrease in oxygen demand, an

impairment of autoregulation or a decrease in tissue width can all lead to increased venous saturation levels. It is important to note that although the model predictions offer each of these scenarios as a possible explanation, not all of them are physiologically relevant when describing the details of glaucoma. For example, suggesting a decrease in the Krogh cylinder tissue width as an explanation for the increased venous saturation levels observed in glaucoma is not consistent with the reduced vascularization observed in some glaucoma patients.[14-16,31] However, the interconnection of tissue width and retinal atrophy suggests that future insight could be gained by using the model to assess the effects of altering multiple factors at once.

The patient-specific model optimizations presented in this study (Fig. 7) suggest that there might be different explanations for the increased venous saturation levels observed among advanced POAG patients and advanced NTG patients. Specifically, a decrease in oxygen demand may be more relevant to the increase in venous saturation observed in advanced POAG (Fig. 7A), while impaired autoregulation mechanisms may be more relevant to the increase in venous saturation observed in advanced NTG (Fig. 7B). This finding also suggests that vascular changes might occur primary to glaucomatous damage in NTG patients. Of note, the relation found between NTG patients and the impairment of blood flow autoregulation has been proposed previously.[42,43] Importantly, impaired blood flow autoregulation could play a role in all advanced glaucoma patients, but to varying extents, as suggested by Fig. 6. Additional theoretical investigations, ideally coupled with statistical methods and conducted on a wider set of glaucoma patients, are needed to confirm the model findings.

In a study that measured venous oxygen saturation under altered light and dark conditions,[44] an increase in arterial and venous saturation was observed, although the arteriovenous difference in oxygen saturation was reported to be stable. The authors hypothesized that the observed increase in venous saturation was accompanied by an increase in oxygen consumption, which opposes the hypothesis offered in the current study. However, in the light and dark study,[44] the oxygen demand increased mostly in the outer retina due to the increased photoreceptor activity. The outer retina is not directly accounted for in the model presented here, which therefore may limit the possible model predictions under various conditions. Additionally, it is possible that a compromised ocular circulation renders an individual more susceptible to a given IOP, thereby representing a confounding factor that falls outside of strict primary or secondary classifications.

5. Conclusions

Overall, this model provides an important step in assessing and quantifying observations in clinical data. Instead of performing statistical analyses on measured observations, the model provides a mechanical framework built upon blood flow

principles that can be used to make independent predictions of the same measured quantities while varying MAP, IOP and arterial oxygen saturation. Overall, the study suggests that the primary mechanisms leading to increased venous saturation in advanced cases of glaucoma might differ between POAG and NTG patients. It is hypothesized that the increased saturation levels are more likely to be explained by decreased oxygen demand in POAG patients and impaired autoregulation in NTG patients. In future studies, the model will continue to be used to address the open question of whether vascular changes occur primary or secondary to glaucomatous damage, possibly identifying subgroups of patients where vascular pathogenic mechanisms play a more significant role. However, progressive data and larger data sets are needed to confirm the hypotheses formulated on the basis of the model predictions.

Acknowledgments

References

1. Moore D, Harris A, Wudunn D, Kheradiya N, Siesky B. Dysfunctional regulation of ocular blood flow: A risk factor for glaucoma? Clin Ophthalmol 2008;2(4):849-861. Available from: http://www.dovepress.com/articles.php?article_id=411 PubMed PMID: 19668439.
2. Harris A, Kagemann L, Ehrlich R, Rospigliosi C, Moore D, Siesky B. Measuring and interpreting ocular blood flow and metabolism in glaucoma. Can J Ophthalmol 2008;43(3):328-336. Available from: http://linkinghub.elsevier.com/retrieve/pii/S0008418208801147 PubMed PMID: 18443609. doi: 10.3129/i08-051.
3. Olafsdottir OB, Hardarson SH, Gottfredsdottir MS, Harris A, Stefansson E. Retinal oximetry in primary open-angle glaucoma. Invest Ophthalmol Vis Sci 2011;52(9):6409-13. Available from: http://iovs.ar-vojournals.org/article.aspx?doi=10.1167/iovs.10-6985 doi: 10.1167/iovs.10-6985.
4. Olafsdottir OB, Vandewalle E, Abegao Pinto L, et al. Retinal oxygen metabolism in healthy subjects and glaucoma patients. Br J Ophthalmol 2014;98(3):329-333. Available from: http://bjo.bmj.com/cgi/doi/10.1136/bjophthalmol-2013-303162 PubMed PMID: 24403567. doi: 10.1136/bjophthal-mol-2013-303162.

5.   Geirsdottir A, Hardarson SH, Olafsdottir OB, Stefansson E. Retinal oxygen metabolism in exudative age-related macular degeneration. Acta Ophthalmol 2014;92(1):27-33. Available from: http://dx.doi.org/10.1111/aos.12294 PubMed PMID: 24447786. doi: 10.1111/aos.12294.
6.   Michelson G, Scibor M. Intravascular oxygen saturation in retinal vessels in normal subjects and open-angle glaucoma subjects. Acta Ophthalmol Scand 2006 Apr;84(3):289-295. Available from: http://doi.wiley.com/10.1111/j.1600-0420.2005.00631.x PubMed PMID: 16704685. doi: 10.1111/j.1600-0420.2005.00631.x.
7.   Abegao Pinto L, Vandewalle E, De Clerck E, Marques-Neves C, Stalmans I. Ophthalmic artery Doppler waveform changes associated with increased damage in glaucoma patients. Invest Ophthalmol Vis Sci 2012 Apr;53(4):2448-53. Available from: http://www.diseaseinfosearch.org/result/3065 PubMed PMID: 22427555. doi: 10.1167/iovs.11-9388.
8.   Akarsu C, Bilgili MY. Color Doppler imaging in ocular hypertension and open-angle glaucoma. Graefes Arch Clin Exp Ophthalmol 2004;242(2):125-9. Available from: http://link.springer.com/10.1007/s00417-003-0809-3 PubMed PMID: 7940146. doi: 10.1007/s00417-003-0809-3.
9.   Butt Z, O'Brien C, McKillop G, Aspinall P, Allan P. Color Doppler imaging in untreated high- and normal-pressure open-angle glaucoma. Invest Ophthalmol Vis Sci 1997;38(3):690-6. Available from: http://www.diseaseinfosearch.org/result/3065 PubMed PMID: 9071223. doi: 10.1364/BOE.3.003127.
10. Rojanapongpun P, Drance SM, Morrison BJ. Ophthalmic artery flow velocity in glaucomatous and normal subjects. Br J Ophthalmol 1993;77(1):25-29. Available from: http://bjo.bmj.com/cgi/doi/10.1136/bjo.77.1.25 PubMed PMID: 8435394. doi: 10.1136/bjo.77.1.25.
11. Tobe LA, Harris A, Hussain RM, et al. The role of retrobulbar and retinal circulation on optic nerve head and retinal nerve fibre layer structure in patients with open-angle glaucoma over an 18-month period. Br J Ophthalmol 2015;99(5):609-612. Available from: http://bjo.bmj.com/cgi/doi/10.1136/bjophthalmol-2014-305780 PubMed PMID: 25467967. doi: 10.1136/bjophthalmol-2014-305780.
12. Grieshaber MC, Flammer J. Blood flow in glaucoma. Curr Opin Ophthalmol 2005;16(2):79-83. Available from: http://content.wkhealth.com/linkback/openurl?sid=WKPTLP:landingpage&an=00055735-200504000-00002 PubMed PMID: 15744136. doi: 10.1097/01.icu.0000156134.38495.0b.
13. Flammer J. The vascular concept of glaucoma. Surv Ophthalmol 1994;38 Suppl(38):105-10.
14. Jia Y, Morrison JC, Tokayer J, Tan O, Lombardi L, Baumann B, et al. Quantitative OCT angiography of optic nerve head blood flow. Biomed Opt Express 2012;3(12):3127-37. Available from: http://europepmc.org/abstract/MED/23243564 PubMed PMID: 23243564. doi: 10.1364/BOE.3.003127.
15. Jia Y, Tan O, Tokayer J, et al. Split-spectrum amplitude-decorrelation angiography with optical coherence tomography. Opt Express 2012;20(4):4710-25. Available from: http://europepmc.org/abstract/MED/22418228 PubMed PMID: 22418228. doi: 10.1364/OE.20.004710.
16. Jia Y, Wei E, Wang X, et al. Optical coherence tomography angiography of optic disc perfusion in glaucoma. Ophthalmol 2014;121(7):1322-1332. Available from: http://europepmc.org/abstract/MED/24629312 PubMed PMID: 24629312. doi: 10.1016/j.ophtha.2014.01.021.
17. Harris A, Jonescu-Cuypers C, Kagemann L, Ciulla T, Krieglstein G. International ophthalmology. Atlas of ocular blood flow: Butterworth-Heinemann; 2003. Available from: http://antibodies.cancer.gov/apps/site/detail/CPTC-GSTMu1-6 PubMed PMID: 11944858. doi: 10.1023/A:1014402730503 .
18. Weinreb R, Harris A. Ocular blood flow in glaucoma: The 6th consensus report of the world glaucoma association. Amsterdam, The Netherlands: Kugler Publications; 2009.
19. Ito M, Murayama K, Deguchi T, et al. Oxygen saturation levels in the juxta-papillary retina in eyes with glaucoma. Exp Eye Res 2008;86(3):512-518. Available from: http://linkinghub.elsevier.com/retrieve/pii/S0014483507003715 PubMed PMID: 18262523. doi: 10.1016/j.exer.2007.12.010.
20. Vandewalle E, Abegao Pinto L, et al. Oximetry in glaucoma: correlation of metabolic change with structural and functional damage. Acta Ophthalmol 2014;92(2):105-110. Available from: http://dx.doi.org/10.1111/aos.12011 PubMed PMID: 23323611. doi: 10.1111/aos.12011.
21. Mordant DJ, Al-Abboud I, Muyo G, Gorman A, Harvey AR, McNaught AI. Oxygen saturation measure-

ments of the retinal vasculature in treated asymmetrical primary open-angle glaucoma using hyperspectral imaging. Eye 2014 Jul;28(10):1190-1200. Available from: http://europepmc.org/abstract/MED/25060843 PubMed PMID: 25060843. doi: 10.1038/eye.2014.169.

22. Ramm L, Jentsch S, Peters S, Augsten R, Hammer M. Investigation of blood flow regulation and oxygen saturation of the retinal vessels in primary open-angle glaucoma. Graefes Arch Clin Exp Ophthalmol 2014;252(11):1803-1810. Available from: http://www.diseaseinfosearch.org/result/3065 PubMed PMID: 25112846. doi: 10.1007/s00417-014-2766-4.

23. Arciero J, Harris A, Siesky B, Amireskandari A, Gershuny V, Pickrell A, et al. Theoretical analysis of vascular regulatory mechanisms contributing to retinal blood flow autoregulation. Invest Ophthalmol Vis Sci 2013 Aug;54(8):5584-93. Available from: http://europepmc.org/abstract/MED/23847315 PubMed PMID: 23847315. doi: 10.1167/iovs.12-11543.

24. Pries AR, Secomb TW, Gessner T, Sperandio MB, Gross JF, Gaehtgens P. Resistance to Blood-Flow in Microvessels in-Vivo. Circ Res 1994;75(5):904-915. Available from: http://circres.ahajournals.org/cgi/pmidlookup?view=long&pmid=7923637 PubMed PMID: 7923637. doi: 10.1161/01.RES.75.5.904.

25. Ye GF, Moore TW, Buerk DG, Jaron D. A compartmental model for oxygen-carbon dioxide coupled transport in the microcirculation. Ann Biomed Eng 1994;22(5):464-479. Available from: http://link.springer.com/10.1007/BF02367083 PubMed PMID: 7825749. doi: 10.1007/BF02367083.

26. Orgul S, Cioffi GA, Wilson DJ, Bacon DR, Van Buskirk EM. An endothelin-1 induced model of optic nerve ischemia in the rabbit. Invest Ophthalmol Vis Sci 1996;37(9):1860-9.

27. Orgul S, Gugleta K, Flammer J. Physiology of perfusion as it relates to the optic nerve head. Surv Ophthalmol 1999;43 Suppl 1(43):592-8. Available from: http://toxnet.nlm.nih.gov/cgi-bin/sis/search2/r?dbs+hsdb:@term+@rn+7782-44-7 PubMed PMID: 10416744.

28. Causin P, Guidoboni G, Malgaroli F, Sacco R, Harris A. Blood flow mechanics and oxygen transport and delivery in the retinal microcirculation: multiscale mathematical modeling and numerical simulation. Biomech Model Mechanobiol 2015 Aug;36:247-259. Available from: http://linkinghub.elsevier.com/retrieve/pii/S135094621300044X PubMed PMID: 26232093. doi: 10.1007/s10237-015-0708-7.

29. Palsson O, Geirsdottir A, Hardarson SH, Olafsdottir OB, Kristjansdottir JV, Stefansson E. Retinal oximetry images must be standardized: a methodological analysis. Invest Ophthalmol Vis Sci 2012 Apr;53(4):1729-33. Available from: http://toxnet.nlm.nih.gov/cgi-bin/sis/search2/r?dbs+hsdb:@term+@rn+7782-44-7 PubMed PMID: 22395877. doi: 10.1167/iovs.11-8621.

30. Michelson G, Welzenbach J, Pal I, Harazny J. Functional imaging of the retinal microvasculature by scanning laser Doppler flowmetry. Int J Ophthalmol 2001;23(4-6):327-335. Available from: http://antibodies.cancer.gov/apps/site/detail/CPTC-GSTMu1-6 PubMed PMID: 11944858. doi: 10.1023/A:1014402730503.

31. Quigley HA. Neuronal death in glaucoma. Prog Retin Eye Res 1999;18(3):39-57. Available from: http://linkinghub.elsevier.com/retrieve/pii/S0014483505801228 PubMed PMID: 9920498. doi: 10.1016/S0014-4835(05)80122-8.

32. Medrano CJ, Fox DA. Oxygen consumption in the rat outer and inner retina: light- and pharmacologically-induced inhibition. Exp Eye Res 1995;61(3):273-284. Available from: http://linkinghub.elsevier.com/retrieve/pii/S0014483505801228 PubMed PMID: 7556491. doi: 10.1016/S0014-4835(05)80122-8.

33. Braun RD, Linsenmeier RA, Goldstick TK. Oxygen consumption in the inner and outer retina of the cat. Invest Ophthalmol Vis Sci 1995;36(3):542-54. Available from: http://www.scholaruniverse.com/ncbi-linkout?id=12695252 PubMed PMID: 12695252. doi: 10.1001/archopht.121.4.547.

34. Wangsa-Wirawan ND, Linsenmeier RA. Retinal oxygen: fundamental and clinical aspects. Arch Ophthalmol 2003;121(4):547-57. Available from: http://www.scholaruniverse.com/ncbi-linkout?id=12695252 PubMed PMID: 12695252. doi: 10.1001/archopht.121.4.547.

35. Kur J, Newman EA, Chan-Ling T. Cellular and physiological mechanisms underlying blood flow regulation in the retina and choroid in health and disease. Prog Retin Eye Res 2012;31(5):377-406. Available from: http://linkinghub.elsevier.com/retrieve/pii/S1350946212000298 PubMed PMID: 22580107. doi: 10.1016/j.preteyeres.2012.04.004.

36. Cringle SJ, Yu DY. A multi-layer model of retinal oxygen supply and consumption helps explain the muted rise in inner retinal PO(2) during systemic hyperoxia. Comp Biochem Physiol A Mol Integr Physiol 2002;132(1):61-66. Available from: http://linkinghub.elsevier.com/retrieve/pii/S109564330100530X PubMed PMID: 12062192. doi: 10.1016/S1095-6433(01)00530-X.

37. Haugh LM, Linsenmeier RA, Goldstick TK. Mathematical models of the spatial distribution of retinal oxygen tension and consumption, including changes upon illumination. Ann Biomed Eng 1990;18(1):19-36. Available from: http://www.scholaruniverse.com/ncbi-linkout?id=2306030 PubMed PMID: 2306030. doi: 10.1007/BF02368415.

38. Lau JC, Linsenmeier RA. Oxygen consumption and distribution in the Long-Evans rat retina. Exp Eye Res 2012;102(5):50-58. Available from: http://linkinghub.elsevier.com/retrieve/pii/S001448351200190X PubMed PMID: 22828049. doi: 10.1016/j.exer.2012.07.004.

39. Roos MW. Theoretical estimation of retinal oxygenation during retinal artery occlusion. Physiol Measol 2004;25(6):1523-1532. Available from: http://toxnet.nlm.nih.gov/cgi-bin/sis/search2/r?dbs+hsdb:@term+@rn+7782-44-7 PubMed PMID: 15712729. doi: 10.1088/0967-3334/25/6/016.

40. Riva CE, Pournaras CJ, Tsacopoulos M. Regulation of local oxygen tension and blood flow in the inner retina during hyperoxia. J Appl Physiol 1986;61(2):592-8. Available from: http://toxnet.nlm.nih.gov/cgi-bin/sis/search2/r?dbs+hsdb:@term+@rn+7782-44-7 PubMed PMID: 3745049.

41. Bek T. Regional morphology and pathophysiology of retinal vascular disease. Prog Retin Eye Res 2013;36:247-259. Available from: http://linkinghub.elsevier.com/retrieve/pii/S135094621300044X PubMed PMID: 23892140. doi: 10.1016/j.preteyeres.2013.07.002.

42. Abegao Pinto L, Vandewalle E, De Clerck E, Marques-Neves C, Stalmans I. Lack of spontaneous venous pulsation: possible risk indicator in normal tension glaucoma. Acta Ophthalmol 2013;91(6):514-520. Available from: http://dx.doi.org/10.1111/j.1755-3768.2012.02472.x PubMed PMID: 22776135. doi: 10.1111/j.1755-3768.2012.02472.x.

43. Oettli A, Gugleta K, Kochkorov A, Katamay R, Flammer J, Orgul S. Rigidity of retinal vessel in untreated eyes of normal tension primary open-angle glaucoma patients. J glaucoma 2011;20(5):303-306. Available from: http://content.wkhealth.com/linkback/openurl?sid=WKPTLP:landing-page&an=00061198-201106000-00007 PubMed PMID: 20577102. doi: 10.1097/IJG.0b013e3181e666a1.

44. Hardarson SH, Basit S, Jonsdottir TE, et al. Oxygen saturation in human retinal vessels is higher in dark than in light. Invest Ophthalmol Vis Sci 2009;50(5):2308-11. Available from: http://iovs.arvojournals.org/article.aspx?doi=10.1167/iovs.08-2576 doi: 10.1167/iovs.08-2576.

Modeling autoregulation in three-dimensional simulations of retinal hemodynamics

Matteo Aletti, Jean-Frédéric Gerbeau, Damiano Lombardi

Inria Paris & Sorbonne Universités, UPMC Univ, Paris 6, France

Abstract

Purpose: Autoregulation is a mechanism necessary to maintain an approximately constant blood flow rate in the microcirculation when acute changes in systemic pressure occur. Failure of autoregulation in the retina has been associated with various diseases, including glaucoma. In this work, we propose an initial attempt to model autoregulation in a 3D network of retinal arteries.
Methods: The blood flow is modeled with the time-dependent Stokes equations. The arterial wall model includes the endothelium and the smooth muscle fibers. Various simplifying assumptions lead to a fluid-structure model where the structural part appears as a boundary condition for the fluid. The numerical simulations are performed on a patient-specific network of 25 segments of retinal arteries located in the inferior temporal quadrant.
Results: The simulations performed on the patient-specific arterial network have provided velocities which are in good agreement with published experimental data. In addition, the model allowed to reproduce flow rate-pressure curves which are comparable with experimental data or results obtained with 0D models. In particular, a characteristic plateau of the flow rate has been found for pressures ranging from 40 to 60 mmHg.
Conclusion: This work proposes the first 3D simulation of blood flow in a real network of retinal arteries and it also incorporates an autoregulation mechanism. This can be viewed as a first step towards a more complete 3D model of the hemodynamic of the eye.

Keywords: retina; autoregulation; 3D hemodynamics

Correspondence: Matteo Aletti, Inria Paris & Sorbonne Universités UPMC Univ Paris 6, France
E-mail: matteo.aletti@inria.fr

1. Introduction

Retinal hemodynamics is strongly influenced by vascular autoregulation. This mechanism is necessary to maintain an approximately constant flow rate in the microcirculation when acute changes in the pressure occur, and it is present in various tissues and organs.[1] Failure or impairment of autoregulation in the retina has been associated with various diseases, for instance, diabetic retinopathy and glaucoma.[2,3,4]

   In the retina, this phenomenon has been studied both in animals[5] and in humans.[6,7,8,9,10,11] Retinal vessels contract or relax in response to a change in the perfusion pressure or to a specific metabolic need. However, the mechanisms underlying the metabolic pathways that trigger vessel contraction or relaxation are still under investigation.

   Autoregulation has been modeled on 0D networks of arterioles[12] and also specifically in the retina.[13] The present work is an initial attempt to address this phenomenon with 3D patient-specific networks, focusing on the mechanical aspects.

   This work is not motivated by any specific clinical application. Its goal is to propose a first step toward a 3D model of the hemodynamics of the eye. Even if existing 0D models can provide valuable information, we believe that 3D models can be useful to better understand the complex mechanical interactions which occur within the eye. With modern segmentation tools, patient-specific vasculature can be automatically reconstructed from retinal fundus images. With 3D models, it will be possible to use these rich data to address new issues where geometry plays an important role. For instance, it could be interesting to investigate the blood flow when a dysfunction occurs in a very localized part of the retina. Venular-arteriolar communication[14] gives another example where a precise representation of the geometry would also be useful. Nowadays, it is even possible to acquire video of the retinal vasculature showing the pulsatility of the arterial wall. A data assimilation procedure in a 3D fluid-structure model could allow us to estimate the local mechanical properties of the vessel, as was done for the aorta.[15,16]

   The numerical simulation of autoregulation in 3D requires a system of equations that model the mechanical interaction between the blood and the arterial wall. Various approaches have been proposed in the literature to address this problem in large arteries. The most complete models are based on the nonlinear elastodynamics equation coupled with the Navier-Stokes equations set in a moving domain. We refer, for example, to the monograph by Fernández and Gerbeau[17] or to one of the many others available [18,19,20,21], to name but a few. These models are very demanding from a computational viewpoint and are valid for large displacements, which is not always necessary, especially in small arteries. Less expensive approaches have been proposed, where the arterial wall equation is drastically simplified.[22,23,24] The model used in the present work adopts this latter approach, but it introduces new features, such as active fibers, which are useful when addressing the autoregulation problem. In the study by Colciago *et al.*[25] the authors observed that using simplified models

on image-based geometry might cause numerical instabilities, due to inaccurate approximations of the normals and the principal curvatures of the surface. A side effect of including fibers in this model is the improvement of the numerical stability, owing to a Laplace operator added to the structure equation. This model has been recently proposed in the study by Aletti *et al.,*[26] where a complete derivation and the numerical schemes can be found. The novelty of the present work lies in its modeling the autoregulation mechanism and the numerical simulation of this phenomenon in patient-specific retinal arteries. The numerical tests are carried out on a portion of the retinal vasculature consisting of 25 arterial segments located in the inferior-temporal quadrant and reconstructed from a retinal fundus image.

The structure of the work is as follows: in Section 2, the fluid-structure framework is introduced; Section 3 addresses the structural model, with special emphasis on the fibers. Section 4 deals with the autoregulation mechanism and Section 5 presents the numerical results. Section 6 presents some limitations of the study and the conclusion.

2. Fluid-structure coupling: main modeling assumptions

The first modeling assumption is to neglect the convective terms in the fluid momentum equation. This approximation is justified since, by considering a maximum vessel diameter $D = 200 \ \mu m$, a velocity $v = 5 \ cm/s$ and a kinematic viscosity $\nu = 0.04 \ cm^2/s$, we obtain a Reynolds number of 2.5. The second main assumption is to suppose that the blood behaves as an homogeneous Newtonian fluid, which is questionable since microvessels are considered.[27,28] We make this hypothesis for the sake of simplicity because it is assumed not to affect too much the autoregulation, which is the mechanism this work focuses on.

The domain Ω_t in which the fluid flows, is in general, time-dependent, since the wall is an elastic structure in interaction with the fluid. The boundary $\partial\Omega_t$ is subdivided into two subsets: Γ_t, which is the interface between the fluid and the structure, and Σ_t, representing the artificial boundaries of the domain where inlet and outlet boundary conditions are enforced. Considering the small displacements of the retinal arteries wall, the domain Ω_t is considered to have a fixed reference configuration denoted by Ω. A schematic representation of this setting is given in Fig. 1. This approximation considerably reduces the computational cost. The fluid equations are therefore:

$$\begin{cases} \rho^f \partial_t \boldsymbol{u} = \nabla \cdot \boldsymbol{\sigma}^f & \text{in } \Omega, \\ \nabla \cdot \boldsymbol{u} = 0 \text{ in } \Omega, \end{cases} \tag{1}$$

where $\boldsymbol{u}$ is the velocity, ρ^f is the fluid density and $\boldsymbol{\sigma}^f = \mu^f(\nabla\boldsymbol{u} + (\nabla\boldsymbol{u})^T) - p\boldsymbol{I}$ is the fluid stress tensor, where μ^f is the dynamic viscosity and p is the pressure.

The velocity on the fixed fluid-structure interface Γ is obtained by a Taylor expansion. This approach is known as a 'transpiration condition'. In the literature, this is
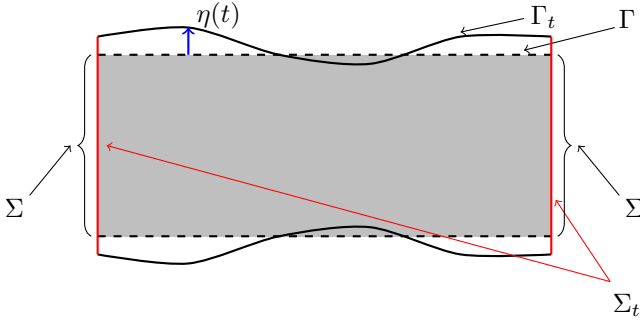
Figure 1: The fluid domain Ω_t is within the two curved lines, however the equations are solved on the fixed computational domain Ω depicted in gray. The displacement field η, which depends on time, maps Γ into Γ_t.

usually a zero-th order expansion. Here, a first order transpiration condition is adopted in order to compute the variation of the flow induced by the wall dynamics, which is important in order to model autoregulation. The main geometrical assumption is that the normal to the structure $\boldsymbol{n}$ is constant in time. Moreover, the kinematics of the vessel wall is assumed to be, at each time, parallel to the normal. With $\boldsymbol{\eta}$ denoting the displacement of the wall, the following holds:

$$\boldsymbol{\eta} = \eta\boldsymbol{n}, \ \forall t. \tag{2}$$

Two conditions have to be satisfied on the fluid-structure interface Γ_t: the continuity of the velocity and the continuity of the stress. Since the structure displacement is assumed to be parallel to the normal direction, the equations for the continuity of the velocity are, for all $x \in \Gamma$, $\boldsymbol{u}(\boldsymbol{I} - \boldsymbol{n} \otimes \boldsymbol{n})|_{\boldsymbol{x}+\eta(\boldsymbol{x})\boldsymbol{n}(\boldsymbol{x})} = \boldsymbol{0}$ and $\boldsymbol{u} \cdot \boldsymbol{n}|_{\boldsymbol{x}+\eta(\boldsymbol{x})\boldsymbol{n}(\boldsymbol{x})} = \partial_t\eta$. The balance of the normal component of the normal stress gives $\boldsymbol{\sigma}^f_{\boldsymbol{nn}}|_{\boldsymbol{x}+\eta(\boldsymbol{x})\boldsymbol{n}(\boldsymbol{x})} = -f^s - p_{iop}$, where p_{iop} denotes the external pressure acting on the structure, in this case the intra ocular pressure, and f^s represents the stress coming from the structure.

The simplifying assumptions on the structure dynamics, which will be detailed in the following section, allow us to treat the structure equations as a boundary condition for the fluid problem.

The equations for the coupled system are written in weak form, on a fixed domain. Let $\boldsymbol{v}, q, \chi, \boldsymbol{w}$ be test functions defined in suitable functional spaces according to the boundary conditions of the problem. In particular let $\boldsymbol{u}(t)$ and $\boldsymbol{v} \in \mathbf{V}$, let $p(t)$ and $q \in M$, where $V = \mathbf{H}^2(\Omega)$ and $M = H^1(\Omega)$. Then:

$$\begin{cases} \langle \partial_t \boldsymbol{u}, \boldsymbol{v} \rangle_\Omega + a(\boldsymbol{u}, \boldsymbol{v}) + b(p, \boldsymbol{v}) = 0 & \text{in } \Omega, t > 0 \\ \langle \nabla \cdot \boldsymbol{u}, q \rangle_\Omega = 0 & \text{in } \Omega, t > 0 \\ \rho_s h_s \langle \partial_{tt}^2 \eta, \chi \rangle_\Gamma + \Psi^s(\eta, \chi) + \langle p_{iop}, \chi \rangle_\Gamma = \langle p + \eta \nabla p \cdot \boldsymbol{n}, \chi \rangle_\Gamma & \text{on } \Gamma \\ \langle \partial_t \eta, \chi \rangle_\Gamma = \langle \boldsymbol{u} \cdot \boldsymbol{n} + \eta \nabla \boldsymbol{u} \boldsymbol{n} \cdot \boldsymbol{n}, \chi \rangle_\Gamma & \text{on } \Gamma \\ \langle (\boldsymbol{I} - \boldsymbol{n} \otimes \boldsymbol{n})(\boldsymbol{u} + \eta \nabla \boldsymbol{u} \boldsymbol{n}), \boldsymbol{w} \rangle_\Gamma = 0 & \text{on } \Gamma. \end{cases} \quad (3)$$

The forms a, b read:

$$\begin{aligned} a : \boldsymbol{V} \times \boldsymbol{V} \to \mathbb{R}, \quad & a(\boldsymbol{u}, \boldsymbol{v}) = \nu^f \langle \nabla \boldsymbol{u} + \nabla \boldsymbol{u}^T, \nabla \boldsymbol{v} \rangle_\Omega && \forall (\boldsymbol{u}, \boldsymbol{v}) \in \boldsymbol{V} \times \boldsymbol{V} \\ b : M \times \boldsymbol{V} \to \mathbb{R}, \quad & b(p, \boldsymbol{v}) = -\langle p, \nabla \cdot \boldsymbol{v} \rangle_\Omega && \forall (p, \boldsymbol{v}) \in M \times \boldsymbol{V}. \end{aligned} \quad (4)$$

where $\langle \cdot, \cdot \rangle_\Omega$ and $\langle \cdot, \cdot \rangle_\Gamma$ denote the standard scalar product in $L^2(\Omega)$ and in $L^2(\Gamma)$, respectively and ν^f is the kinematic viscosity. It should be noted that in this framework the structure dynamics is embedded as a boundary condition of the fluid problem. The system in Eq.(3) is discretised by means of finite elements (P1-P1, with a SUPG stabilisation) and by a mixed semi-implicit scheme in time. All the details of the implementation of this approach are provided in the study by Aletti *et al.*[26]

Remark 1. *Numerically, the tangential velocity sometimes exhibits oscillations on the fluid-structure interface, especially on complex geometries. The reason for these oscillations is not completely understood. They might be due to the approximation of the normals and the curvatures, as already noted by Colciago et al.[25], or to the first order transpiration terms adopted in our approach. We observed that this problem can be alleviated by the following consistent stabilization term:*

$$\langle (\boldsymbol{I} - \boldsymbol{n} \otimes \boldsymbol{n})(\boldsymbol{u} + \eta \nabla \boldsymbol{u} \boldsymbol{n}), \boldsymbol{w} \rangle_\Gamma = -\beta \langle h \nabla (\boldsymbol{I} - \boldsymbol{n} \otimes \boldsymbol{n}) \boldsymbol{u}, \nabla \boldsymbol{w} \rangle_\Gamma \text{ on } \Gamma, \quad (5)$$

where $\beta \geq 0$ is the stabilization coefficient and h is the surface element size.

3. Modeling the vessel wall dynamics

Retinal arteriolar structure consists of a thin layer of endothelium layer and a layer of smooth muscle cells which is more developed with respect to vessels of the same size in other organs.[28] From a modeling perspective, the wall is considered as an elastic shell, so as to render the behavior of the endothelium, and several fiber layers to model the smooth muscles.

This section is organised as follows. After introducing the notation, the model of the structure is presented in its general form, as it appears in system (3). The model for the endothelium is described, followed by a presentation of the fiber layer. First a derivation of a constitutive law for the smooth muscle fibers is presented. This constitutive law is then used to close the kinematical and mechanical description of the fiber layer surrounding the endothelium.

3.1 Notation

Let Γ be the reference position of the vessel wall, *i.e.*, the position at which it is in a normal state of equilibrium, without external influences. The geometrical configuration of Γ is described by a regular map Φ such that $\boldsymbol{\xi} \in \omega \subseteq \mathbb{R}^2 \mapsto \boldsymbol{x} = \Phi(\boldsymbol{\xi}) \in \Gamma$. Let $\boldsymbol{A}$ be the first fundamental form and $\boldsymbol{B}$ the second fundamental form associated with the reference configuration Γ. Let $\boldsymbol{S} = \boldsymbol{A}^{-1}\boldsymbol{B}$ be the representation of the shape operator. The eigenvalues of the shape operator are the principal curvatures of the surface Γ, the mean curvature being the average of the principal curvatures and the Gaussian curvature being their product. The surface parametrization is denoted by Greek letters and the curvilinear coordinates domain is denoted by $\omega \subseteq \mathbb{R}^2$.

3.2 Equations for the structure dynamics

The equations for the structure dynamics, appearing as a boundary condition of the system (3), are obtained by adding the inertia terms to the elastic energy of the structure. In particular, the dynamics equations in weak form can be written as:

$$\int_{\omega} \rho^s h^s (\partial_{tt}^2 \eta) \chi \sqrt{a} \, d\boldsymbol{\xi} + \Psi^s(\eta, \chi) = 0, \tag{6}$$

where the thickness of the structure is denoted by h^s and its density by ρ^s. The form Ψ^s describes the behavior of the structure. It is considered as the sum of several contributions:

$$\Psi^s = \Psi^\kappa + \Psi^{\mathbf{w}} + \Psi^{\mathbf{v}}, \tag{7}$$

where Ψ^κ, defined in Eq.(14), represents the contribution of the endothelium and $\Psi^{\mathbf{w}}, \Psi^{\mathbf{v}}$, defined in Eq.(35), represent the contribution of the fibers aligned in the directions $\mathbf{w}$ and $\mathbf{v}$ respectively.

Each of these terms is analyzed in detail in the following part of this section. In general, all the weak forms are derived as follows: given an elastic model and the corresponding energy, the equilibrium configuration for the structure can be seen as the stationary point of the energy functional:

$$\Psi(\eta, \chi) := \langle \delta_\eta \psi(\eta), \chi \rangle_\Gamma = 0, \tag{8}$$

where δ_η denotes the Frechet derivative with respect to η and ψ is the elastic energy.

3.3 The endothelium layer

A nonlinear Koiter shell model is adopted to describe the endothelium dynamics. The equations and a detailed mathematical derivation are presented in the work by Ciarlet.[29] The choice of this nonlinear model, rather than the simpler linear version, is motivated by the consistency with the fiber layer description. In particular, when the fiber kinematics (see Eq.(31)) is described, some nonlinear contributions arise. The

terms appearing in the Koiter model that have the same order with respect to the displacement field η have thus to be kept. The displacement field, as pointed out in Eq.(2), is parallel to the normal to the reference configuration.

The simplifying hypotheses from a mechanical point of view are the following:

- the bending terms are negligible;

- the material is linear, isotropic and homogeneous.

The equilibrium configuration is the stationary point of the energy functional:[29]

$$\psi^\kappa(\eta) = \frac{1}{2} \int_\omega \mathcal{E}^{\alpha\beta\sigma\tau} g_{\sigma\tau}(\eta) g_{\alpha\beta}(\eta) \; h_\kappa \sqrt{a} \, d\boldsymbol{\xi} - \int_\omega \boldsymbol{f} \cdot \eta \, h^\kappa \sqrt{a} \, d\boldsymbol{\xi}, \qquad (9)$$

where $\sqrt{a} = \sqrt{det(A)}$, h^κ is the shell thickness and $\boldsymbol{f}$ are the external forces, $g(\eta)$ is the change of metric tensor. The properties of the material are contained in the elastic tensor $\mathcal{E}$, whose contravariant components read:

$$\mathcal{E}^{\alpha\beta\sigma\tau} = \frac{4\lambda^s \mu^s}{\lambda^s + 2\mu^s} A^{\alpha\beta} A^{\sigma\tau} + 2\mu^s A^{\alpha\sigma} A^{\beta\tau} + 2\mu^s A^{\alpha\tau} A^{\beta\sigma}, \qquad (10)$$

where λ^s, μ^s are the Lamé coefficients of the structure.

By exploiting the hypothesis of normal displacement (see Eq.(2)), the expression for the change of metric tensor becomes:

$$g_{\alpha\beta} = -B_{\alpha\beta}\eta + \frac{1}{2} A^{\sigma\tau} B_{\sigma\alpha} B_{\tau\beta} \eta^2 + \frac{1}{2} \partial_\alpha \eta \partial_\beta \eta, \qquad (11)$$

where the derivative with respect to the Greek letters denotes the derivation with respect to the surface parametrization.

The form Ψ^κ describing the equilibrium of the nonlinear Koiter shell model under the assumptions made reads:

$$\Psi^\kappa(\eta, \chi) := \frac{2E}{1 - \nu^2} \int_\omega \left(c_1 \eta - 3c_2 \eta^2 + 2c_3 \eta^3 \right) \chi - 2\nabla\chi^T (C_1 \eta + C_2 \eta^2)\nabla\eta + \quad (12)$$

$$-\nabla^T \eta \left[(C_1 + 2C_2 \eta) \chi \right] \nabla\eta + \frac{1}{2} \left(\nabla\eta^T A^{-1} \nabla\eta \right) \nabla^T \chi A^{-1} \nabla\eta \, h^\kappa \sqrt{a} \, d\boldsymbol{\xi} - \quad (13)$$

$$\int_\omega \boldsymbol{f}_n \cdot \chi \, h^\kappa \sqrt{a} \, d\boldsymbol{\xi}, \qquad (14)$$

where E is the Young modulus of the material, ν the Poisson coefficient, the constant tensors (C_j) and the coefficients (c_k) are expressed as functions of the mean

and Gaussian curvatures (respectively ρ_1 and ρ_2) and the Poisson ratio as follows:

$$c_1 = 4\rho_1^2 - 2(1-\nu)\rho_2, \tag{15}$$

$$c_2 = 4\rho_1^3 + (\nu - 3)\rho_1\rho_2, \tag{16}$$

$$c_3 = 4\rho_1^4 - 4\rho_1^2\rho_2 + \frac{1}{2}(1+\nu)\rho_2^2, \tag{17}$$

$$C_1 = \left[\nu\rho_1 I + \frac{1}{2}(1-\nu)S\right] A^{-1}, \tag{18}$$

$$C_2 = \left[\nu\rho_1^2 I + \frac{1}{2}(1-\nu)S^2\right] A^{-1}. \tag{19}$$

Notice that, at the first order, the endothelium behaves pointwise as a spring with constant c_1. However the overall behavior can be roughly considered as the sum of two contributions: a nonlinear spring and a nonlinear membrane. More details about this derivation can be found in the study by Aletti *et al.* [26]

3.4 The smooth muscle cells model

In this section, a model describing the behavior of the smooth muscle cells (SMC) is investigated. The resulting model is a 1D idealisation of the SMC muscle fibers. The equations derived in the present section are used as a constitutive law to close the model for the fiber layers.

The layer of SMCs, which in large vessels is also responsible for adaptive changes in the stiffness, has the ability to contract or relax following electrochemical stimuli in order to regulate the blood flow (see, e.g., studies by Murtada *et al.* and Milnor *et al.* [30,31])

There is no autonomic innervation in the retinal vasculature. [32] This implies that the regulation is carried out by mechanisms that take place locally in the eye. [33] The contraction of the smooth muscle cells is controlled by the concentration of calcium ions, which trigger the phosphorylation of myosin light chains. [1] The different chemical pathways are not investigated in the present work and we make the simplifying assumption that the concentration of calcium ions depends only on changes of the pressure. However, if more sophisticated models are available they can be included to relate the concentration of calcium ions to the other mechanisms.

A chemical state model of the smooth muscle cells has been proposed by Hai and Murphy [34]. This model takes four chemical species into account: myosin (M), phosphorilated myosin (M_p), phosphorilated actin myosin cross-bridge (AM_p) and unphosphorilated actin myosin cross-bridge (AM). It describes the evolution of the concentrations ($\alpha_M, \alpha_{M_p}, \alpha_{AM}, \alpha_{AM_p}$) of those species with a linear system of differential equations $\dot{\boldsymbol{\alpha}} = \boldsymbol{K}\boldsymbol{\alpha}$ under the constraint $\alpha_M + \alpha_{M_p} + \alpha_{AM} + \alpha_{AM_p} = 1$, where $\boldsymbol{K}$ depends on the concentration of calcium ions.

The chemical model by Hai and Murphy [34] was used by Yang *et al.* [35,36] to describe the myogenic response. More recently, the approach by Yang *et al.* has been extended

to a continuum mechanics framework.[37,30] Such models have also been coupled with a membrane model to compute the concentration of calcium ions as a response to external stimuli.[38] The overall mechanism is reproduced in the following way: an external stimulus causes a change in calcium concentration which alters the chemical state of the SMC. Once the chemical state is known, it is possible to compute the active component of the forces in the cell and thus its mechanical behavior.

In what follows, we refer to the model of Yang *et al.*[35,36] and propose a further simplification in order to derive a constitutive equation for a 1D fiber. In the model presented in the first study by Yang *et al.*,[35] the mechanics of a single SMC is described by two elements in parallel: a spring characterized by an exponential force-length relationship (to describe the passive structural behavior of the overall cell) and an active element for the cross-bridges. The total force is given by

$$F = F_{cell} + F_{cb}, \tag{20}$$

where cb stands for cross-bridges. The active element is itself made of three elements in series which model the active force of the actin-myosin cross-bridges, their passive elasticity properties and the viscous effects, respectively. The total length of the active element L_{cb} can be expressed as the sum of the length of these three components:

$$L_{cb} = L_{cb,a} + L_{cb,el} + L_{cb,visc}, \tag{21}$$

where $a, el, visc$ stand for active, elastic and viscous, respectively. The length of the cell and of the active element representing the cross-bridges are the same and they are equal to the total length L.

$$L = L_{cell} = L_{cb}. \tag{22}$$

The system of equations is closed by observing that the elements in series have the the same force:

$$F_{cb,a} = F_{cb,el} = F_{cb,visc}. \tag{23}$$

Finally, considering the constitutive laws of the three components of the active element, it is possible to solve the system and obtain the total force. Such force depends on the total length of the cell, on its time derivative and also on the cell chemical state described by the proportion of phosphorilated and dephosphorilated actin-myosin:

$$F = F(L, \frac{dL}{dt}, \alpha_{AM}, \alpha_{AM_p}). \tag{24}$$

This expression can be simplified if the visco-elastic effects are neglible compared to the elastic effects. In such a case the total force is a function of only the total length and the concentration of phosphorilated actin-myosin:
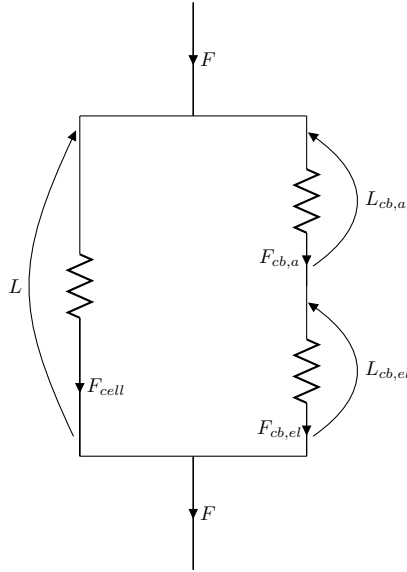
$$F = F(L, \alpha_{AM_p}). \tag{25}$$

Figure 2: Scheme of the equivalent circuit describing the model by Yang et al. [35,36] when viscous effects are neglected.

Its expression can be obtained by solving the following system whose equivalent circuit is depicted in Fig.2:

$$\begin{cases} F_{cell} & = k_{cell}(e^{\alpha_{cell}\left(\frac{L}{L_0}-1\right)} - 1) \\ F_{cb,a} & = f_{AM_p}\alpha_{AM_p}e^{-b\left(\frac{L_{cb,a}}{L_{opt}}-1\right)^2} \\ F_{cb,el} & = k_{el}\left(e^{\alpha_{el}\left(\frac{L_{cb,el}}{L_{cb,el,0}}-1\right)} - 1\right) \\ F_{cb,a} & = F_{cb,el} \\ F & = F_{cell} + F_{cb,a} \\ L & = L_{cb,a} + L_{cb,el}, \end{cases} \tag{26}$$

where the first three equations represent the constitutive law of the cell, the active part of the cross-bridges and their elastic part. Therefore, the parameters k_{cell}, α_{cell}, L_0, f_{AM_p}, b, L_{opt}, k_{el}, α_{el} and $L_{cb,el,0}$ describe the structural properties of the SMC. The last three equations are obtained by combining equations (20),(21),(22) and (23).

Since it is not possible to obtain a closed-form solution for system (26), we make an approximation to obtain an affine stress-strain relationship. Eq.(25) is linearized with respect to the reference configuration L_{ref}:

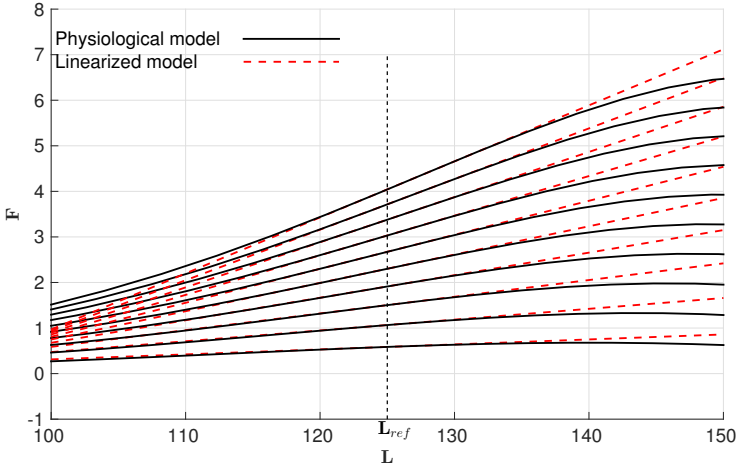$$F \sim F_0(\alpha_{AM_p}) + F_1(\alpha_{AM_p})(L - L_{ref}), \tag{27}$$

Figure 3: Force-length relationship from system (26), coefficients taken from Yang et al. (2003). Numerical approximation (black) compared with its approximation (dashed red) linearized with respect to the L_{ref}.

where the analytical expressions for F_0 and F_1 are known and are derived through a Taylor expansion. In order to corroborate the final result, the physiological model in system (26) is compared with its linearized version for different values of α_{AM_p}. The result is presented in Fig.3, which shows that a simple affine constitutive law is indeed valid for an approximated description of the SMC fibers for the retina in physiological regimes.

The constitutive law adopted, which is the simplest law that approximately describes the behaviour of the SMCs is:

$$\sigma_{1D} = k_0 + k_1 \varepsilon_{1D}, \tag{28}$$

where σ_{1D} is the elastic stress, k_0 is the pre-stress of the fiber, k_1 is the elastic modulus, ε_{1D} is the fiber deformation.

Equation (27) can finally be used to identify the parameters k_0, k_1, after a rescaling. The SMCs are assumed to have a cylindrical shape with a radius r_{smc}. The force is divided by πr_{smc}^2 in order to obtain the stress. The result reads:

$$k_0(\alpha_{AM_p}) = \frac{1}{\pi r_{smc}^2} F_0(\alpha_{AM_p}),$$
$$k_1(\alpha_{AM_p}) = \frac{1}{\pi r_{smc}^2} F_1(\alpha_{AM_p}), \tag{29}$$

In practice, it is difficult to have access to the value of α_{AM_p}, which depends on many

factors. This is why in the following section, the functions k_0 and k_1 will be simply assumed to depend on an 'activation parameter' ζ:

$$\sigma_{1D} = k_0(\zeta) + k_1(\zeta)\varepsilon_{1D}, \tag{30}$$

3.5 The fiber layer

In this section, the equations describing the dynamics of an SMC fiber layer are detailed. The main hypotheses are the following:

- the fibers are perfectly attached to the shell;

- the fibers are characterized by an affine stress-strain constitutive law.

The kinematic hypothesis implies that the deformation of the fibers equals the deformation of the underlying shell structure in the direction of the fibers.

Let $\mathbf{w} \in \mathbb{T}_{\boldsymbol{x}}(\Gamma)$ be a unitary vector belonging to the tangent space of Γ defined at the point $\boldsymbol{x} \in \Gamma$. The deformation of the fiber in the $\mathbf{w}$ direction can thus be written as:

$$\varepsilon_{1D} = \mathbf{w}^T \boldsymbol{G} \mathbf{w} = -d_1 \eta + \frac{d_2}{2}\eta^2 + \frac{1}{2}\nabla\eta^T P_{\mathbf{w}} \nabla\eta, \tag{31}$$

where the scalar coefficients d_j and the projector $P_{\mathbf{w}}$ are defined as $d_1 = \mathbf{w}^T \boldsymbol{B} \mathbf{w}$, $d_2 = \mathbf{w}^T \boldsymbol{B}\boldsymbol{S}\mathbf{w}$, $P_{\mathbf{w}} = \mathbf{w} \otimes \mathbf{w}$. The constitutive stress-strain relationship is given by Eq.(30).

Let $\varrho_{\mathbf{w}}$ be the fraction of the total number of fibers aligned in the direction $\mathbf{w}$. The elastic energy of the fibers aligned in the direction $\mathbf{w}$ is of the form:

$$\psi^{\mathbf{w}}(\eta) = \frac{1}{2}\int_{\omega} \varrho_{\mathbf{w}} \left[k_0 + k_1\varepsilon_{1D}(\eta)\right]\varepsilon_{1D}(\eta)\, h^f \sqrt{a}\, d\boldsymbol{\xi} + \int_{\omega} r_{\mathbf{w}}\, h^f \sqrt{a}\, d\boldsymbol{\xi}, \tag{32}$$

where h^f is the thickness of the smooth muscle cell layer, $r_{\mathbf{w}}$ represents the potential energy of a force acting on the fibers aligned with the direction $\mathbf{w}$.

The equilibrium equations are introduced in weak form as the scalar product with a test function of the Frechet derivative of the energy with respect to the displacement:

$$\Psi^{\mathbf{w}}(\eta, \chi) = \int_{\omega} \varrho_{\mathbf{w}} \nabla\chi^T \left[k_0 + k_1\left(-d_1 + \frac{d_2}{2}\eta^2\right) + \frac{k_1}{4}W\right] P_{\mathbf{w}}\nabla\eta + \tag{33}$$

$$\varrho_{\mathbf{w}}\left[k_0\left(-d_1 + d_2\eta\right) + k_1\left(-d_1^2\eta - \frac{3d_1 d_2}{2}\eta^2 + \frac{d_2^2}{2}\eta^3\right) + \frac{k_1}{2}(-d_1 + d_2\eta)W\right]\chi + \tag{34}$$

$$(\delta_{\eta} r_{\mathbf{w}})\chi\, h^f \sqrt{a}\, d\boldsymbol{\xi}, \tag{35}$$

where $W = \left(\nabla\eta^T P_{\mathbf{w}}\nabla\eta\right)$. We remark that the contribution of the first line is of membrane type, whereas the second line contains algebraic terms in the test function and hence it renders a nonlinear spring-like behavior.

When $\eta = 0$ and the SMCs are not activated, i.e. $\zeta = \bar{\zeta}$, the reference configuration is the equilibrium configuration only if the stress exerted by the fibers due to their pre-stress is balanced by the underlying shell. By injecting $\eta = 0, \zeta = \bar{\zeta}$ into Eq.(35), we obtain:

$$\int_\omega (-\varrho_{\mathbf{w}} \bar{k}_0 d_1 + \delta_\eta r_{\mathbf{w}}) \chi h^f \sqrt{a} \, d\boldsymbol{\xi} = 0, \qquad (36)$$

hence, for any arbitrary test function χ, the following holds

$$r_{\mathbf{w}} = \varrho_{\mathbf{w}} \bar{k}_0 d_1 \eta, \qquad (37)$$

where $\bar{k}_0 = k_0(\bar{\zeta})$.

Remark 2. *The consequence of Eq.(37) is the appearance, in the balance of the normal forces on Γ, of a force term. This is the main result of the SMCs contraction. Indeed, by combining Eq.(35) and Eq.(37) and, by setting $k_1 = 0$ for the sake of simplicity, we get:*

$$\Psi^{\mathbf{w}}(\eta, \chi) = \int_\omega \varrho_{\mathbf{w}} k_0(\zeta) d_2 \eta \chi + \varrho_{\mathbf{w}} k_0(\zeta) \nabla \chi^T P_{\mathbf{w}} \nabla \eta \, h^f \sqrt{a} \, d\boldsymbol{\xi} + \qquad (38)$$

$$\int_\omega \varrho_{\mathbf{w}} (\bar{k}_0 - k_0(\zeta)) d_1 \chi \, h^f \sqrt{a} \, d\boldsymbol{\xi}. \qquad (39)$$

This weak formulation represents the contribution to the structure equation due to the fibers in direction $\mathbf{w}$. The effect of the activation on the wall mechanics is twofold: firstly, there is a change in the constants that characterize the passive behavior of the structure (namely in the spring- and membrane-like contributions), and secondly, a force term of the following form appears:

$$\int_\omega \varrho_{\mathbf{w}} (\bar{k}_0 - k_0(\zeta)) d_1 \chi \, h^f \sqrt{a} \, d\boldsymbol{\xi}. \qquad (40)$$

When ζ reaches its maximum value, this term is negative, representing a force in the normal direction that induces a negative displacement. Note that the sign of d_1 depends on the curvature along the fiber direction and it is, in general, negative when the normal is pointing outward.

Remark 3. *In order to get an intuitive insight in the normal equilibrium for the structure, an example in an idealized setting is proposed. The structure is a cylinder of radius R, a linear Koiter shell is considered, that is in equilibrium under a pressure load. The displacement with respect to the reference configuration is constant and, hence, space and time derivatives of the displacement field vanish. Under these conditions the equilibrium displacement is the solution of an algebraic equation:*

$$\left(\frac{E h^\kappa}{1 - \nu^2} c_1 + \varrho_{\mathbf{w}} h^f (k_0(\zeta) d_2 - k_1 d_1^2) \right) \bar{\eta} = p - p_{iop} - \varrho_{\mathbf{w}} h^f d_1 (\bar{k}_0 - k_0(\zeta)), \quad (41)$$

the coefficient of $\bar{\eta}$ depends on both the mechanical properties of the structure ($E, \nu, \varrho_{\mathbf{w}}$, $k_0(\zeta)$, k_1) and on its geometrical properties (c_1, d_1, d_2 which depend on the curvature). The force term depends on both the mechanical properties ($\varrho_{\mathbf{w}}, k_0(\zeta)$) and the geometry d_1. Let us separate the shell contribution, the fiber contribution and the transmural presssure:

$$\left(\frac{Eh^{\kappa}}{1-\nu^2} c_1 \right) \bar{\eta} = \Delta p - \sigma_{fiber}, \tag{42}$$

where σ_{fiber} denotes the active and passive contributions of the fibers. When the tangential stress in a cylinder is computed by using the Koiter shell model, the following is obtained:

$$\sigma_{\theta} = \frac{E}{1-\nu^2} \frac{\bar{\eta}}{R}. \tag{43}$$

Injecting this relationship into the equilibrium equation yields:

$$\sigma_{\theta} \frac{h^{\kappa}}{R} = \Delta p - \sigma_{fiber}. \tag{44}$$

The shell (arteriolar endothelium) is in equilibrium under the load exerted by the fibers and the transmural pressure. The tangential wall tension is simply the integral of the stress across the thickness (by making the assumption of constant stress in the section, the tension is given by $\sigma_{\theta} h^{\kappa}$), so that the equilibrium equation reduces to the Laplace law.

Remark 4. In general, the fibers are not parallel to only one direction. In what follows, two linearly independent unitary vectors $\mathbf{v}, \mathbf{w} \in \mathbb{T}_{\boldsymbol{x}}(\Gamma)$ and the associated fiber fractions $\varrho_{\mathbf{v}}$ and $\varrho_{\mathbf{w}}$ defined in each point of Γ are considered. In such a case the two associated energy fields $\psi^{\mathbf{w}}$ and $\psi^{\mathbf{v}}$ sum up. If medical imaging or histological examination provide the fiber orientations, this information can be used to set $\mathbf{v}, \varrho_{\mathbf{v}}, \mathbf{w}$ and $\varrho_{\mathbf{w}}$. When this information is missing, these values can be based on a qualitative knowledge of the fibers orientation. For example, it is indicated in the study by Pournaras et al. [28] p. 287 that the smooth muscle cells are oriented both circularly and longitudinally. One possible choice paralle is therefore to take the principal direction of curvature, and $\varrho_{\mathbf{v}} = \varrho_{\mathbf{w}} = \frac{1}{2}$.

With this choice, the fiber layer behaves as an isotropic homogeneous membrane.

3.6 Summary of Section 3

For the sake of clarity, we now summarize the model derived in the previous sections. The whole system is made of the Stokes equations

$$\begin{cases} \langle \partial_t \boldsymbol{u}, \boldsymbol{v} \rangle_{\Omega} + a(\boldsymbol{u}, \boldsymbol{v}) + b(p, \boldsymbol{v}) = 0 & \text{in } \Omega, t > 0, \\ \langle \nabla \cdot \boldsymbol{u}, q \rangle_{\Omega} = 0 & \text{in } \Omega, t > 0, \\ \langle (\boldsymbol{I} - \boldsymbol{n} \otimes \boldsymbol{n})(\boldsymbol{u} + \eta \nabla \boldsymbol{u} \boldsymbol{n}), \boldsymbol{w} \rangle_{\Gamma} = 0 & \text{on } \Gamma, t > 0, \\ \sigma(\boldsymbol{u}, p)\boldsymbol{n} = -p_{in}(t)\boldsymbol{n} & \text{on } \Gamma_{in}, t > 0, \end{cases} \tag{45}$$

and by the continuity of the normal velocity and of the normal stresses at the vessel wall:

$$\begin{cases} \rho_s h_s \langle \partial_{tt}^2 \eta, \chi \rangle_\Gamma + \Psi^s(\eta, \chi) + \langle p_{iop}, \chi \rangle_\Gamma = \langle p + \eta \nabla p \cdot \boldsymbol{n}, \chi \rangle_\Gamma & \text{on } \Gamma, t > 0, \\ \langle \partial_t \eta, \chi \rangle_\Gamma = \langle \boldsymbol{u} \cdot \boldsymbol{n} + \eta \nabla \boldsymbol{u} \boldsymbol{n} \cdot \boldsymbol{n}, \chi \rangle_\Gamma & \text{on } \Gamma, t > 0. \end{cases} \quad (46)$$

The behavior of the two-layer structure is modeled by $\Psi^s(\eta, \chi)$, defined in Equation (7).

4. Autoregulation and pressure feedback

As indicated in Eq.(30), the pre-stress and the elastic modulus of the SMCs are assumed to be a function of a parameter ζ describing the activation of the SMCs. Inspired by Arciero *et al.*[13], we use the following expression for k_0:

$$k_0(\zeta) = k_{0,ref} + k_{0,a}^{max} S(\zeta), \quad S(\zeta) = \frac{1 - e^{-s(\zeta - p_{ref})}}{1 + \frac{1}{\omega} e^{-s(\zeta - p_{ref})}}, \quad (47)$$

where p_{ref} is a given reference pressure, $k_{0,ref}$ is the pre-stress in the absence of activation, $\omega = -k_{0,a}^{min}/k_{0,a}^{max}$, where $k_{0,a}^{max}$ and $k_{0,a}^{min}$ are given parameters. The parameter s affects the slope of the curve and can be estimated by using

$$s = \frac{1}{p_{max} - p_{ref}} \ln \left(\frac{1 + q/\omega}{1 - q} \right),$$

where $\ln$ is the natural logarithm, and p_{max} is the value for which the active component of the pre-stress is equal to $q k_{0,a}^{max}$. A similar behavior could be assumed for the elastic modulus of the fibers k_1, but in what follows, we simply suppose that $k_1 = 0$. A plot of the sigmoid function is presented in Figure 4 for typical values of the parameters.

We now present our strategy to compute the activation parameter ζ. As mentioned in Section 3.4, SMCs react to changes in the concentration of calcium ions. The calcium ion concentration is in turn varied by several regulatory mechanisms.[5,28,33] Since the focus of this work is the mechanical aspect of autoregulation, we make the simplifying assumption that the activation variable ζ directly depends on the feeding pressure. The rationale behind this choice is that an increase in the feeding pressure triggers the mechanims that will eventually affect the activation state of the smooth muscle cells. If models describing regulatory mechanisms and the concentration of calcium ions along the network were available, they could be used to provide a more physiological expression of ζ.

We estimate ζ by using the mean values of the incoming pressure over the different cardiac cycles. These values are used to reconstruct ζ as a piecewise linear
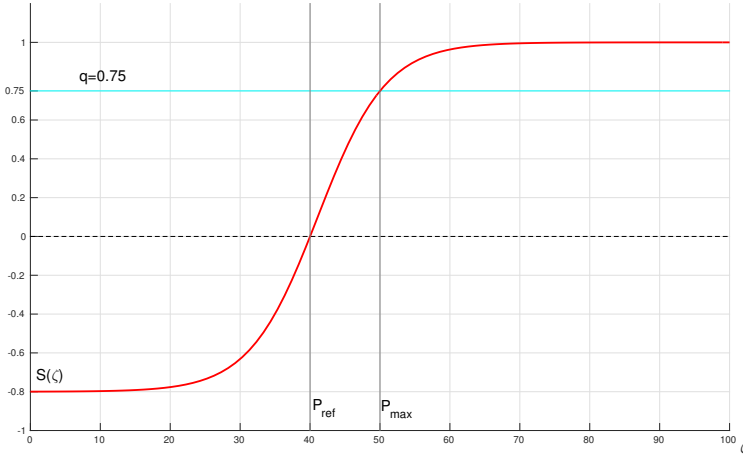
Figure 4: Sigmoid function for the parameters $\omega = 0.8$, $P_{max} = 50$, $q = 0.75$. $S(\zeta)$ on the y-axis and ζ on the x-axis.

function in time, in the following way:

$$
\begin{cases}
\zeta(t) = \frac{1}{T_{i+1}-T_i}\left((T_{i+1}-t)\zeta_i + (t-T_i)\zeta_{i+1}\right) \quad \forall t \in (T_i, T_{i+1}) \text{ for } i = 1, 2, \ldots \\
\zeta_{i+1} = \frac{1}{(T_{i+1}-T_i)|\Sigma_{in}|} \int_{T_i}^{T^{i+1}} \int_{\Sigma_{in}} p \, d\Gamma \, dt, \quad \text{for } i = 1, 2, \ldots \\
\zeta_0 = p_{ref}
\end{cases}
$$

(48)

where Σ_{in} denotes the inlet of the computational domain and T_i the starting time of the i-th heart cycle.

As usual in computational hemodynamics, the 3D domain is truncated and the downstream vessels is taken into account by using 0D Windkessel models. More precisely, each terminal vessel in our 3D network is connected to the venous pressure via an RCR compartment. For simplicity, all these compartments are assumed to share the same values for the resistances (R_{prox} and R_{distal}) and the capacitance (C). The autoregulation in the Windkessel element is governed by the following hypotheses: the proximal resistance R_{prox} remains constant over time; the distal resistance is given by:

$$R_{distal}(\zeta) = R_{distal,ref} + \alpha S(\zeta) R_{distal,ref},$$

(49)

with $\alpha = 1 - R_{distal,max}/R_{distal,ref}$; the capacitance varies so that the characteristic time $\tau = R_{distal}(\zeta)C(\zeta)$ remains constant.

5. Numerical simulations

This section is structured as follows. First, we present a validation of the model on a test case where the mean incoming pressure coincides with the reference pressure. The values obtained for the velocity are compared with the experimental data presented in the work by Riva et al. [39] Second, we present a numerical experiment where the mean incoming pressure is varied. Different flow rate-incoming pressure curves are obtained for different values of the maximum pre-stress of the fibers.

5.1 Reference case and validation

5.1.1 Data

The geometry was obtained using a retinal fundus image in the Drive dataset. [40] The image was segmented and the vessels tree reconstructed by using the algorithms presented in the studies by Al-Diri et al. [41] and Calivà et al. [42] We considered only the inferior temporal arteriole and its branches. Twenty-five segments were obtained via the segmentation algorithm. The 3D tree was reconstructed from the 2D image by first assuming a circular section for the vessels and then by projecting the results over a sphere. The detailed bifurcations were not available from the segmentation and they were reconstructed using B-splines. The mesh generation was carried out using gmsh [43] and then refined using Feflo.a, an anisotropic local remeshing sotware developed at Inria. Figure5 shows two snapshots of the geometry used for the computations. The computational mesh has 822,071 tetrahedra and 105,604 triangles on the surface, for a total number of vertices of 165,238.

In the study by Guidoboni et al. [44], the authors suggest taking a pressure at the inlet of the central retinal artery that is equal to two thirds of the mean brachial arterial pressure. With typical values of systolic and diastolic brachial pressure ($120/80 \, \mathrm{mmHg}$), this gives 62 mmHg. In addition, a pressure drop of about 20 mmHg is assumed to take place from the upstream of the central retinal artery to the downstream of the lamina cribrosa. Thus, we choose $p_{ref} = 40 \mathrm{mmHg}$, which is a reference value for the pressure at the beginning of our 3D network. Regarding the outlet boundary condition we set the venous pressure at 20 mmHg, which is compatible with the value used as a reference in the work by Guidoboni et al. [44] after the venules compartment. The reference values for the Windkessel parameters are $R_{distal} = 6 \cdot 10^8 \, \mathrm{P \, cm^{-3}}$, $R_{prox} = 6 \cdot 10^7 \, \mathrm{P \, cm^{-3}}$, $C = 1.67 \cdot 10^{-10} \, \mathrm{s \, cm^3 \, P^{-1}}$. The blood viscosity is given by $\nu^f = 0.03 \, \mathrm{cm^2 \, s^{-1}}$, and its density by $\rho^f = 1 \, \mathrm{g/cm^3}$. The structure parameters are the Young modulus of the endothelium $E = 0.05 \, \mathrm{MPa}$ and its Poisson ratio $\nu = 0.5$, the thickness of the endothelium $h^\kappa = 5 \mu m$ and the total thickness of the vessel $h^s = 25 \mu m$. The density of the structure is set equal to $1 \mathrm{g/cm^3}$. The fiber layer thickness is $h^f = 20 \mu m$ The mechanical properties of the fibers are the pre-stress $k_0 = 0.4 \mathrm{MPa}$ and the elastic modulus $k_1 = 0$. The intra-ocular pressure p_{iop} is kept constant at 15mmHg.
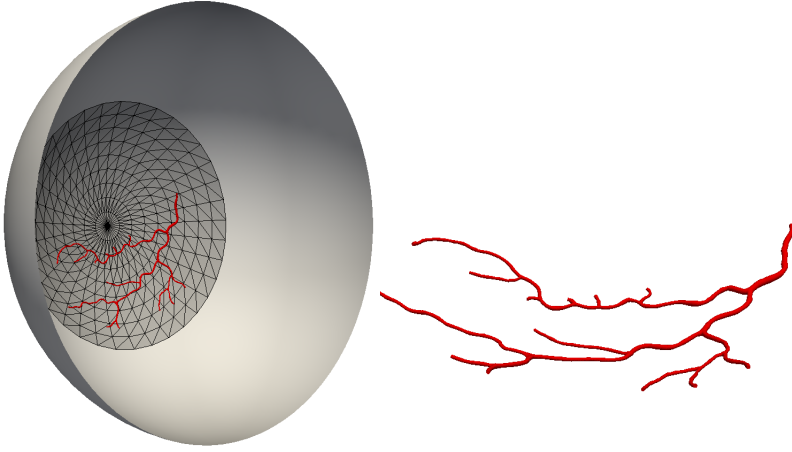
Figure 5: Computational mesh (left) and a broader view with the sphere used for the reconstruction (right).

The duration of the cardiac cycle is $0.8s$, and the duration of diastole is $0.25s$. The time-profile of the incoming pressure is the following:

$$P_{in}(t) = \begin{cases} (p_{sys} - p_{dia})\sin(\pi t/0.25) + p_{dia} & t \in [0, 0.25] \\ p_{dia} & t \in [0.25, 0.8], \end{cases} \qquad (50)$$

where $p_{dia} = 0.9\bar{P}$ and $p_{sys} = p_{dia} + 0.16\pi\bar{P}$ are the diastolic and systolic pressure for a given value of mean pressure $\bar{P}$. A summary of these choices is presented in Table 1.

5.1.2 Results

In order to have a reference solution where autoregulation does not play a role and that can be used to assess the model, we set $\bar{P} = 40$ mmHg. We use $\boldsymbol{u} = 0, \eta = 0$ as initial conditions, and observe a quasi periodic behavior after two cardiac cycles. In Figure 6 we report a snapshot from the simulation taken at the time instant $t = 3s$, *i.e.*, during the diastole. The figure also displays the surface of the computational mesh. To compare the results of our simulation with the experimental data presented in the study by Riva *et al.* [39], we compute the mean value (in time, over a cardiac cycle) of the blood velocity at the center of different sections of the artery along the network. The value of the diameter is taken as the mean value of the diameters over the segment (between two bifurcations) which contains the section. The chosen points of the network are depicted in Figure 7, and a comparison of the data is given in Figure 8. In

Table 1: Summary of the model parameters. In the table P stands for Poise.

Fluid parameters			
ν^f	0.03 cm^2 s^{-1}	ρ^f	1 g cm^{-3}
Boundary conditions and Windkessel parameters			
P_{venous}	20 mmHg	P_{iop}	15 mmHg
R_{distal}	$6 \cdot 10^8$ P cm^{-3}	$R_{proximal}$	$6 \cdot 10^7$ P cm^{-3}
C	$1.67 \cdot 10^{-10}$ s cm^3 P^{-1}		
Structure parameters			
ρ^s	1 g cm^{-3}	E	0.05 MPa
ν	0.5	k_0	0.4 MPa
k_1	0	h^k	5 μm
h^f	20 μm	h^s	25 μm

Figure 6: Velocity profiles on some slices of the domain. Values are taken during the diastolic phase of the fourth cardiac cycle ($t = 3s$).
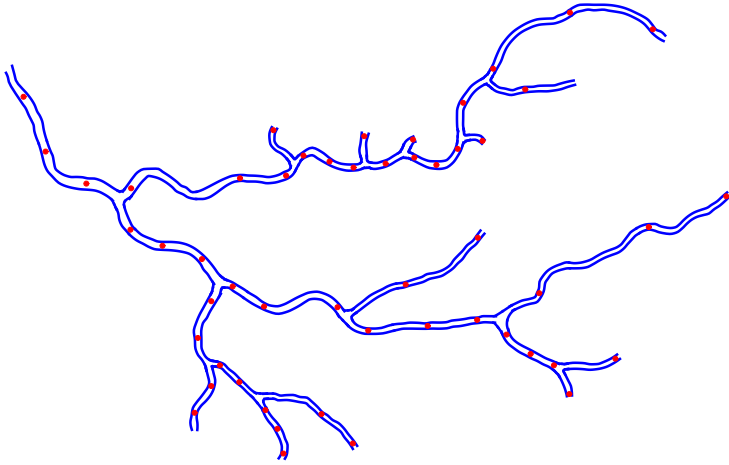
Figure 7: Points where the mean velocity has been measured for comparison with experimental data presented in Riva *et al.* [39]

order to have a fair comparison, the mean velocity over time has been computed using the same formula as was used in the study by Riva *et al.* [39] (one third of the systolic velocity plus two thirds of the diastolic velocity).

The results of the model are within the same range of values as the experimental data. The two sets of points also show a similar variability. However, there is a region for which either the velocity has been underestimated or the diameter has been overestimated (around 100 μm, 1 cm/s). We can provide two explanations for this discrepancy. Firstly, the errors might come from the segmentation: the points with the lowest velocity are in the terminal vessels, which are the smallest and therefore the most difficult to capture with the segmentation algorithms. Secondly, it is possible that the assumption that all terminal vessels experience the same downstream equivalent resistance is too rough an approximation of reality.

5.2 Autoregulation

5.2.1 Data

For this test case we used the geometry and the data reported in Section 5.1.1. The control mechanism has been detailed in Section 4. For the present simulation, the parameters defining the sigmoid activation function (see Eq.(47)) arFe the following: $\omega = 0.8$ and $P_{max} = 50$mmHg, $q = 75\%$.
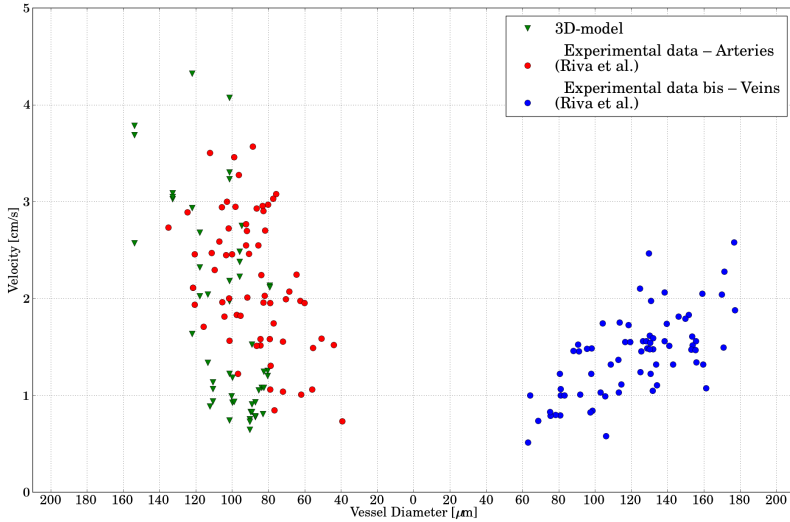
Figure 8: Comparison between the experimental data taken from Riva *et al.* [39] Mean velocity in time (y-axis) and diameter (x-axis, arteries on the left side and veins on the right side). Experimental data are depicted by circles: red refers to arteries and blue refers to veins. Data computed by the proposed model are depicted by green triangles.

5.2.2 Results

In Figure 9 the relationship between the flow rate and the pressure at the inlet is depicted for a representative cardiac cyle in two distinct scenarios: without autoregulation (in blue) and with autoregulation (in red). Each loop is a cardiac cycle for a simulation performed by imposing a different mean incoming pressure. The chosen values are $\bar{P} = [30, 40, 50, 60, 70]$mmHg. In the autoregulated case, the parameters determining the control intensity are: $k_{0,a}^{max} = 0.1$MPa and $\alpha = 0.15$. It should be noted that for a mean pressure of $\bar{P} = 40$mmHg there is only one loop since it is the reference pressure, *i.e.*, the pressure for which the smooth muscle cells maintain their reference length. By observing these curves it can be inferred that the control mechanism acts directly on the vessels resistance. In particular, when the mean pressure is higher than the reference pressure, the flow rate is diminished, whereas when the mean pressure is lower, the SMCs action tends to increase the flow rate.

Each point of the curves represented in Figure 10 is the value of the flow entering the network for a given value of inlet pressure. The mean inlet pressure $\bar{P}$ is varied from 30 mmHg to 70 mmHg. The parameters governing autoregulation are chosen as follows: $k_{0,a}^{max}$ takes three values: 0 (no autoregulation), 0.05 MPa and 0.1 Mpa. The autoregulation parameter α, defined in equation (49), indicates how much the
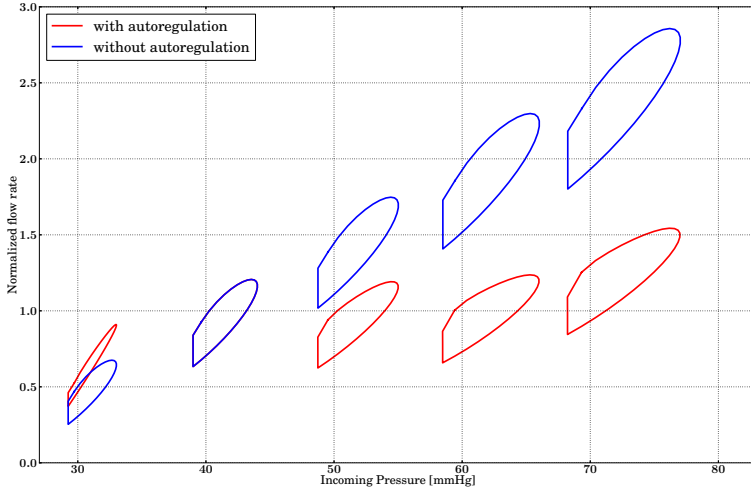
Figure 9: Normalized flow rate (y-axis) with respect to incoming pressure (x-axis). Each circle represents one cardiac cycle from a different simulation. The blue circles correspond to the simulations without autoregulation: $K_{0,a}^{max} = 0$ and $\alpha = 0$, for different values of $\bar{P}$. The red circles refer to the autoregulation parameters $K_{0,a}^{max} = 0.1$MPa and $\alpha = 0.15$.

downstream circulation is able to vary its overall resistance. Two different cases were considered: $\alpha = 0$ (no autoregulation) and $\alpha = 0.15$ (for which the maximum value of distal resistance is equal $1.15 R_{distal,ref}$). For each numerical experiment four cardiac cycles are simulated. The values of the flow are taken in the last cycle and the flow is normalized with respect to the value obtained for $\bar{P} = p_{ref} = 40$mmHg. Figure 10 shows that using $k_{a,0}^{max} = 0.1$MPa and using autoregulation in the Windkessel model (circles, green), it is possible to replicate a plateau in the flow rate-pressure relationship. This result is similar to that obtained in the study by Arciero *et al.*[13] with a 0D approach. The impact of autoregulation in the Windkessel for this choice of parameters can be observed by comparing the green curve (circles) with the red one (down triangles), which was obtained with the same $k_{a,0}^{max}$ and by turning the Windkessel autoregulation off ($\alpha = 0$).

6. Limitations and conclusion

In this work, we have proposed a first attempt at modeling autoregulation in a 3D network of retinal arteries. Our approach is based on a simplified fluid-structure model whose computational cost is of the same order as the cost of a pure fluid problem. The
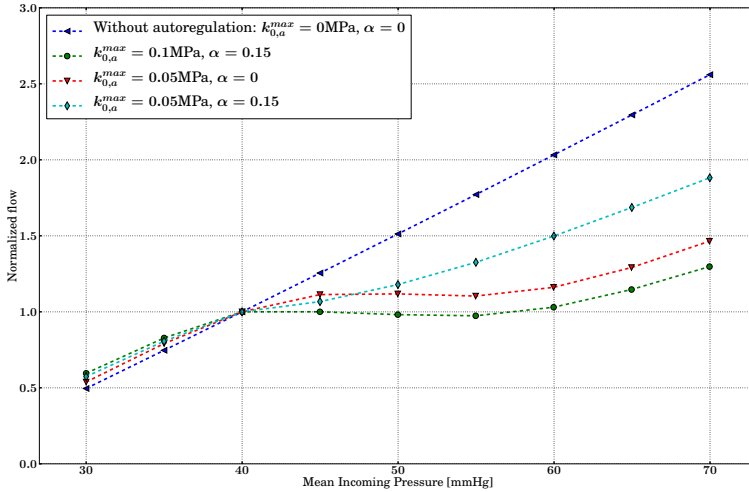
Figure 10: Autoregulation curves. Mean incoming pressure on the fourth cardiac cycles (x-axis) and normalized flow rate over the fourth cardiac cycle (y-axis). Different lines correspond to different values for the autoregulation parameters. Each point on a curve refers to a different simulation with a given mean incoming pressure.

model used for the wall includes smooth muscle fibers, whose active constitutive law has been derived by approximating physiological models proposed in the literature. The simulations performed in a real network of 25 segments of retinal arteries have provided velocities which are in good agreement with published experimental data. By varying the parameters of the active component of the constitutive law, we have been able to reproduce flow rate-pressure curves which are comparable with experimental data or results obtained with 0D models. In particular, a characteristic plateau of the flow rate has been found for pressures ranging from 40 to 60 mmHg.

    To the best of our knowledge, this study is the first to propose 3D simulations of blood flow in a real network of retinal arteries, including an autoregulation mechanism. It can be viewed as a first step toward a more complete 3D model of the hemodynamic of the eye. In spite of encouraging results, many limitations remain and the model could be improved in various ways.

    Firstly, the diameter of the vessels considered in this work is below $200\,\mu m$, which means that the hemodynamics is in a microcirculation regime.[27,28] In such vessels, the Fahraeus effect, the Fahraeus-Lindqvist effect and plasma skimming may be relevant in determining the distribution of hematocrit and the velocity profile.[45,46]

    Secondly, our autoregulation model describes how smooth muscle fibers control

the blood flow, but not the physiological mechanisms that trigger the contraction or the relaxation. The feedback mechanism could be improved to include other aspects than only the inlet pressure.

Besides these limitations, future works could also improve the models used for the downstream vasculature, and should address other important phenomena like the interaction with other compartments, such as the lamina cribrosa or the intraocular pressure.

Acknowledgements

References

1.   Schubert R, Mulvany MJ. The myogenic response: established facts and attractive hypotheses.. Clin Sci (Lond) 1999;96(4):313-326. Available from: http://toxnet.nlm.nih.gov/cgi-bin/sis/search2/r?dbs+hsdb:@term+@rn+7440-70-2 PubMed PMID: 10087237.

2.   Kohner EM, Patel V, Rassam SM. Role of blood flow and impaired autoregulation in the pathogenesis of diabetic retinopathy.. Diabetes 1995;44(6):603-607. Available from: http://toxnet.nlm.nih.gov/cgi-bin/sis/search2/r?dbs+hsdb:@term+@rn+7782-44-7 PubMed PMID: 7789621. doi: 10.2337/diab.44.6.603.

3.   Rassam SM, Patel V, Kohner EM. The effect of experimental hypertension on retinal vascular autoregulation in humans: a mechanism for the progression of diabetic retinopathy.. Exp Physiol 1995;80(1):53-68. Available from: http://onlinelibrary.wiley.com/resolve/openurl?genre=article&sid=nlm:pubmed&issn=0958-0670&date=1995&volume=80&issue=1&spage=53 PubMed PMID: 7734138.

4.   Grunwald JE, Riva CE, Stone RA, Keates EU, Petrig BL. Retinal autoregulation in open-angle glaucoma.. Ophthalmology 1984;91(12):1690-1694. Available from: http://www.diseaseinfosearch.org/result/3065 PubMed PMID: 6521997.

5.   Jeppesen P, Aalkjær C, Bek T. Myogenic response in isolated porcine retinal arterioles, Current eye research 27. Ophthalmology 2003;91(12):217-222. Available from: http://www.diseaseinfosearch.org/result/3065 PubMed PMID: 6521997.

6.   Jeppesen P, Sanye-Hajari J, Bek T. Increased blood pressure induces a diameter response of retinal arterioles that increases with decreasing arteriolar diameter.. Invest Ophthalmol Vis Sci 2007;48(1):328-331. Available from: https://www.researchgate.net/publication/e/pm/17197550?ln_t=p&ln_o=linkout PubMed PMID: 17197550. doi: 10.1167/iovs.06-0360.

7.   Blum M, Bachmann K, Wintzer D, Riemer T, Vilser W, Strobel J. Noninvasive measurement of the Bayliss effect in retinal autoregulation.. Graefes Arch Clin Exp Ophthalmol 1999;237(4):296-300.

Available from: http://ClinicalTrials.gov/search/term=10208262%20%5BPUBMED-IDS%5D PubMed PMID: 10208262.

8. Harris A, Arend O, Bohnke K, Kroepfl E, Danis R, Martin B. Retinal blood flow during dynamic exercise.. Graefes Arch Clin Exp Ophthalmol 1996;234(7):440-444. Available from: https://www.nlm.nih.gov/medlineplus/exerciseandphysicalfitness.html PubMed PMID: 8817287.

9. Dumskyj MJ, Eriksen JE, Dor´e CJ, Kohner EM. Autoregulation in the human retinal circulation: assessment using isometric exercise, laser doppler velocimetry, and computer-assisted image analysis. Microvascular research 1996;51(3):378-392. Available from: https://www.researchgate.net/publication/e/pm/8992235?ln_t=p&ln_o=linkout PubMed PMID: 8992235. doi: 10.1006/mvre.1996.0034.

10. Robinson F, Riva CE, Grunwald JE, Petrig BL, Sinclair SH. Retinal blood flow autoregulation in response to an acute increase in blood pressure.. Invest Ophthalmol Vis Sci 1986;27(5):722-726. Available from: https://www.researchgate.net/publication/e/pm/3700021?ln_t=p&ln_o=linkout PubMed PMID: 3700021.

11. Nagaoka T, Mori F, Yoshida A. Retinal artery response to acute systemic blood pressure increase during cold pressor test in humans.. Invest Ophthalmol Vis Sci 2002;43(6):1941-1945. Available from: https://www.nlm.nih.gov/medlineplus/highbloodpressure.html PubMed PMID: 12037003.

12. Arciero JC, Carlson BE, Secomb TW. Theoretical model of metabolic blood flow regulation: roles of ATP release by red blood cells and conducted responses. American Journal of Physiology - Heart and Circulatory Physiology 2008;295(4). Available from: http://ajpheart.physiology.org/cgi/pmidlookup?view=long&pmid=18689501 PubMed PMID: 18689501. doi: 10.1152/ajpheart.00261.2008.

13. Arciero J, Harris A, Siesky B, Amireskandari A, Gershuny V, Pickrell A, et al. Theoretical analysis of vascular regulatory mechanisms contributing to retinal blood flow autoregulation.. Invest Ophthalmol Vis Sci 2013 Aug;54(8):5584-5593. Available from: http://europepmc.org/abstract/MED/23847315 PubMed PMID: 23847315. doi: 10.1167/iovs.12-11543.

14. Hester RL, Hammer LW. Venular-arteriolar communication in the regulation of blood flow.. Am J Physiol Regul Integr Comp Physiol 2002;282(5). Available from: http://ajpregu.physiology.org/cgi/pmidlookup?view=long&pmid=11959667 PubMed PMID: 11959667. doi: 10.1152/ajpregu.00744.2001.

15. Moireau P, Bertoglio C, Xiao N, Figueroa CA, Taylor C, Chapelle D, et al. Sequential identification of boundary support parameters in a fluid-structure vascular model using patient image data. Biomechanics and Modeling in Mechanobiology 2012;12(3):475-496. Available from: http://link.springer.com/10.1007/s10237-012-0418-3 doi: 10.1007/s10237-012-0418-3.

16. Bertoglio C, Barber D, Gaddum N, Valverde I, Rutten M, Beerbaum P, et al. Identification of artery wall stiffness: In vitro validation and in vivo results of a data assimilation procedure applied to a 3D fluid–structure interaction model. Journal of Biomechanics 2014;47(5):1027-1034. Available from: http://linkinghub.elsevier.com/retrieve/pii/S0021929014000098 PubMed PMID: 24529756. doi: 10.1016/j.jbiomech.2013.12.029.

17. Fernández M, Gerbeau JF. Algorithms for fluid-structure interaction problems, Cardiovascular Mathematics. Modeling and simulation of the circulatory system. Springer Verlag, 2009, Ch. 9; .

18. Bazilevs Y, Calo V, Zhang Y, Hughes TJ. Isogeometric fluid– structure interaction analysis with applications to arterial blood flow. Computational Mechanics 2006;38(4-5):4-5. Available from: http://link.springer.com/10.1007/s00466-006-0084-3 doi: 10.1007/s00466-006-0084-3.

19. Crosetto P, Reymond P, Deparis S, Kontaxakis D, Stergiopulos N, Quarteroni A. Fluid–structure interaction simulation of aortic blood flow. Computers & Fluids 2011;43(1):46-57. Available from: http://linkinghub.elsevier.com/retrieve/pii/S0045793010003452 doi: 10.1016/j.compfluid.2010.11.032.

20. Moireau P, Xiao N, Astorino M, Figueroa CA, Chapelle D, Taylor CA, et al. External tissue support and fluid-structure simulation in blood flows.. Biomech Model Mechanobiol 2011 Feb;11(1-2):1-18. Available from: https://www.researchgate.net/publication/e/pm/21308393?ln_t=p&ln_o=linkout PubMed PMID: 21308393. doi: 10.1007/s10237-011-0289-z.

21. Fernández MA, Landajuela M, Vidrascu M. Fully decoupled time-marching schemes for incompressible fluid/thin-walled structure interaction. Journal of Computational Physics 2015;297:156-181.

Available from: http://linkinghub.elsevier.com/retrieve/pii/S0021999115003289 doi: 10.1016/j.jcp.2015.05.009.

22. Figueroa CA, Vignon-Clementel IE, Jansen KE, Hughes TJR, Taylor CA. A coupled momentum method for modeling blood flow in three-dimensional deformable arteries. COMPUTER METHODS IN APPLIED MECHANICS AND ENGINEERING 2006 Aug;195(41-43):5685-5706. Available from: http://linkinghub.elsevier.com/retrieve/pii/S004578250500513X doi: 10.1016/j.cma.2005.11.011.

23. Nobile F, Vergara C. An effective fluid-structure interaction formulation for vascular dynamics by generalized robin conditions. SIAM Journal on Scientific Computing 2008;30(2):731-763. Available from: http://epubs.siam.org/doi/abs/10.1137/060678439 doi: 10.1137/060678439.

24. Pironneau O. Numerical Simulations of Coupled Problems in Engineering, Vol. 33 of Computational Methods in Applied Sciences. Springer International Publishing; 2014.

25. Colciago CM, Deparis S, Quarteroni A. Comparisons between reduced order models and full 3D models for fluid–structure interaction problems in haemodynamics. Journal of Computational and Applied Mathematics 2014;265:120-138. Available from: http://linkinghub.elsevier.com/retrieve/pii/S0377042713005049 doi: 10.1016/j.cam.2013.09.049.

26. M. Aletti, J.-F. Gerbeau, D. Lombardi, A simplified fluid-structure model for arterial flow. Application to retinal hemodynamics., submitted (2015).

27. Wong TY, Klein R, Klein BEK, Meuer SM, Hubbard LD. Retinal vessel diameters and their associations with age and blood pressure.. Invest Ophthalmol Vis Sci 2003;44(11):4644-4650. Available from: http://www.scholaruniverse.com/ncbi-linkout?id=14578380 PubMed PMID: 14578380.

28. Pournaras CJ, Rungger-Brändle E, Riva CE, Hardarson SH, Stefansson E. Progress in retinal and eye research. 2008.

29. Ciarlet PG, Vol, e.V. (Mathematical) . of Studies in Mathematics and its Applications. Amsterdam: North-Holland Publishing Co; 2000.

30. Murtada S, Kroon M, Holzapfel GA. A calcium-driven mechanochemical model for prediction of force generation in smooth muscle.. Biomech Model Mechanobiol 2010 Mar;9(6):749-762. Available from: http://toxnet.nlm.nih.gov/cgi-bin/sis/search2/r?dbs+hsdb:@term+@rn+7440-70-2 PubMed PMID: 20354752. doi: 10.1007/s10237-010-0211-0.

31. Milnor WR. Cardiovascular physiology. Oxford University Press; 1990.

32. Laties AM. Central retinal artery innervation. Absence of adrenergic innervation to the intraocular branches.. Arch Ophthalmol 1967;77(3):405-409. Available from: http://archopht.jamanetwork.com/article.aspx?doi=10.1001/archopht.1967.00980020407021 PubMed PMID: 4960032. doi: 10.1001/archopht.1967.00980020407021.

33. Bek T. Regional morphology and pathophysiology of retinal vascular disease.. Prog Retin Eye Res 2013 Jul;36:247-259. Available from: https://www.nlm.nih.gov/medlineplus/retinaldisorders.html PubMed PMID: 23892140. doi: 10.1016/j.preteyeres.2013.07.002.

34. Hai CM, Murphy RA. Cross-bridge phosphorylation and regulation of latch state in smooth muscle. Am J Physiol 254 (1 Pt 1988;1:99-106.

35. Yang J, Clark JW, Bryan RM, Robertson C. The myogenic response in isolated rat cerebrovascular arteries: smooth muscle cell model. Medical Engineering & Physics 2003;25(8):691-709. Available from: http://linkinghub.elsevier.com/retrieve/pii/S1350453303001000 doi: 10.1016/S1350-4533(03)00100-0.

36. Yang J, Clark JW, Bryan RM, Robertson CS. The myogenic response in isolated rat cerebrovascular arteries: vessel model. Medical Engineering & Physics 2003;25(8):711-717. Available from: http://linkinghub.elsevier.com/retrieve/pii/S1350453303001012 PubMed PMID: 12900185. doi: 10.1016/S1350-4533(03)00101-2.

37. Stålhand J, Klarbring A, Holzapfel GA. Smooth muscle contraction: mechanochemical formulation for homogeneous finite strains.. Prog Biophys Mol Biol 2007 Aug;96(1-3):465-481. Available from: http://www.scholaruniverse.com/ncbi-linkout?id=17884150 PubMed PMID: 17884150. doi: 10.1016/j.pbiomolbio.2007.07.025.

38. Sharifimajd B, Stålhand J. A continuum model for excitation–contraction of smooth muscle under finite deformations. Journal of Theoretical Biology 2014;355:1-9. Available from: http://linkinghub.elsevier.com/retrieve/pii/S0022519314001519 PubMed PMID: 24657629. doi: 10.1016/j.jtbi.2014.03.016.

39. Riva CE, Grunwald JE, Sinclair SH, Petrig BL. Blood velocity and volumetric flow rate in human retinal vessels.. Invest Ophthalmol Vis Sci 1985;26(8):1124-1132. Available from: https://www.researchgate.net/publication/e/pm/4019103?ln_t=p&ln_o=linkout PubMed PMID: 4019103.

40. Staal J, Abràmoff MD, Niemeijer M, Viergever MA, van Ginneken B. Ridge-Based Vessel Segmentation in Color Images of the Retina. IEEE Trans. Med. Imaging 2004;23(4):501-509. Available from: http://ieeexplore.ieee.org/lpdocs/epic03/wrapper.htm?arnumber=1282003 PubMed PMID: 15084075. doi: 10.1109/TMI.2004.825627.

41. Al-Diri B, Hunter A, Steel D. An active contour model for segmenting and measuring retinal vessels. IEEE Transactions on Medical Imaging 2009;28(9):1488-1497. Available from: http://www.scholaruniverse.com/ncbi-linkout?id=19336294 PubMed PMID: 19336294. doi: 10.1109/TMI.2009.2017941.

42. F. Calivà, M. Aletti, B. Al-Diri, A. Hunter, A new tool to connect blood vessels in fundus retinal images, in: Proceedings of 37th Annual international conference of the IEEE engineering in medicine and biology society, 2015.

43. Geuzaine C, Remacle JF. Gmsh: A 3-D finite element mesh generator with built-in pre-and post-processing facilities. International Journal for Numerical Methods in Engineering 2009;79(11):1309-1331. Available from: http://doi.wiley.com/10.1002/nme.2579 doi: 10.1002/nme.2579.

44. Guidoboni G, Harris A, Cassani S, Arciero J, Siesky B, Amireskandari A, et al. Intraocular pressure, blood pressure, and retinal blood flow autoregulation: a mathematical model to clarify their relationship and clinical relevance.. Invest Ophthalmol Vis Sci 2014 May;55(7):4105-4118. Available from: http://europepmc.org/abstract/MED/24876284 PubMed PMID: 24876284. doi: 10.1167/iovs.13-13611.

45. Pries A, Neuhaus D, Gaehtgens P, Blood . viscosity in tube flow: dependence on diameter and hematocrit. American Journal of Physiology 1992;263:1770-1770.

46. Pries AR, Ley K, Claassen M, Gaehtgens P. Red cell distribution at microvascular bifurcations.. Microvasc Res 1989;38(1):81-101. Available from: https://www.researchgate.net/publication/e/pm/2761434?ln_t=p&ln_o=linkout PubMed PMID: 2761434.

Integrated Multidisciplinary Approaches in the Study and Care of the Human Eye

Integrated Multidisciplinary
Approaches in the Study
and Care of the Human Eye

EDITED BY
PAOLA CAUSIN
GIOVANNA GUIDOBONI
RICCARDO SACCO
ALON HARRIS

EDITED BY
PAOLA CAUSIN
GIOVANNA GUIDOBONI
RICCARDO SACCO
ALON HARRIS

ISBN 978-90-6299-241-6
Dec. 2015. x and 185 pages. Hardbound.
Many figures and photos. 16x24 cm
List price € 80.00 / US $ 100.00*
Discount price: € 72.00 / US $ 90.00*
* excl. 6% VAT (only applicable for EU customers) and shipping costs

The human eye offers the possibility to non-invasively observe and quantify many morphological and hemodynamical data in real time. The interpretation of these dynamic data, however, remains a challenging task.

Mathematical models provide quantitative representations of the biomechanics and fluid-dynamics of the eye and their relationship with systemic conditions providing a valuable investigative tool. While inevitably presenting complex mathematics, this volume is not intended solely for mathematicians, rather it facilitates a new and exciting interdisciplinary field and approach to eye disease.

Order online at www.kuglerpublications.com

Journal for Modeling in Ophthalmology

Focus and Scope

While the rapid advance of imaging technologies in ophthalmology is making available a continually increasing number of data, the interpretation of such data is still very challenging and this hinders the advance in the understanding of ocular diseases and their treatment. Interdisciplinary approaches encompassing ophthalmology, physiology, mathematics and engineering have shown great capabilities in data analysis and interpretation for advancing basic and applied clinical sciences.

The Journal for Modeling in Ophthalmology (JMO) was created in 2014 with the aim of providing a forum for interdisciplinary approaches integrating mathematical and computational modeling techniques to address open problems in ophthalmology. JMO welcomes articles that use modeling techniques to investigate questions related to the anatomy, physiology and function of the eye in health and disease.